UNCLASSIFIED
SECURITY CLASSIFICATION OF THIS PAGE

REPORT DOCUMENTATION PAGE

1a. REPORT SECURITY CLASSIFICATION UNCLASSIFIED	1b. RESTRICTIVE MARKINGS None
2a. SECURITY CLASSIFICATION AUTHORITY	3. DISTRIBUTION/AVAILABILITY OF REPORT Approved for public release; Distribution unlimited.
2b. DECLASSIFICATION/DOWNGRADING SCHEDULE	
4. PERFORMING ORGANIZATION REPORT NUMBER(S) SIO Ref. 85-7	5. MONITORING ORGANIZATION REPORT NUMBER(S) AFGL-TR-84-0168

6a. NAME OF PERFORMING ORGANIZATION University of California, San Diego Visibility Laboratory	6b. OFFICE SYMBOL *(If applicable)*	7a. NAME OF MONITORING ORGANIZATION Air Force Geophysics Laboratory
6c. ADDRESS *(City, State and ZIP Code)* La Jolla, California 92093		7b. ADDRESS *(City, State and ZIP Code)* Hanscom AFB, Massachusetts 01731 Contract Monitor: Lt.Col. John D. Mill/OPA
8a. NAME OF FUNDING/SPONSORING ORGANIZATION	8b. OFFICE SYMBOL *(If applicable)*	9. PROCUREMENT INSTRUMENT IDENTIFICATION NUMBER F19628-82-C-0060

8c. ADDRESS *(City, State and ZIP Code)*

10. SOURCE OF FUNDING NOS.

PROGRAM ELEMENT NO.	PROJECT NO.	TASK NO.	WORK UNIT NO.
62101F	7670	7670-14	7670-14-02

11. TITLE *(Include Security Classification)* The Fascat Model Performance Under Fractional Cloud Conditions and Related Studies

12. PERSONAL AUTHOR(S)
Wayne S. Hering & Richard W. Johnson

13a. TYPE OF REPORT Final	13b. TIME COVERED FROM 1 MAR 82 TO 31 DEC 84	14. DATE OF REPORT *(Yr., Mo., Day)* 1984 December	15. PAGE COUNT 116

16. SUPPLEMENTARY NOTATION

17. COSATI CODES

FIELD	GROUP	SUB. GR.

18. SUBJECT TERMS *(Continue on reverse if necessary and identify by block number)*
Atmospheric Optical Properties, Sky, Cloud, and Terrain Radiance
Visible Image Transmission, Target Detection

19. ABSTRACT *(Continue on reverse if necessary and identify by block number)*

This Final Report under Contract No. F19628-82-C-0060 summarizes the results of several research studies directed toward the development of models of the optical properties of the atmosphere which are suitable for the operational support of tactical weapons and sensors operating in the visible and infrared portions of the electromagnetic spectrum.

The overall contractual effort has been an integral part of the overall Air Force Geophysics Laboratory (AFGL/AFSC) program to develop a thorough understanding of atmospheric effects on visible and infrared radiation through the atmosphere, and ultimately, the concomitant limitations on the performance of electro-optical systems such as target acquisition devices and precision guided munitions.

This Final Report contains a brief review of four previously issued interim reports which were submitted during this contractual interval in support of the primary model development task. It also contains the complete documentation for the FASCAT code and a discussion of the FASCAT model performance under fractional cloud meteorological conditions.

20. DISTRIBUTION/AVAILABILITY OF ABSTRACT UNCLASSIFIED/UNLIMITED ☒ SAME AS RPT. ☐ DTIC USERS ☐		21. ABSTRACT SECURITY CLASSIFICATION Unclassified
22a. NAME OF RESPONSIBLE INDIVIDUAL Lt.Col John D. Mill	22b. TELEPHONE NUMBER *(Include Area Code)* (617) 861-3665	22c. OFFICE SYMBOL AFGL/OPA

DD FORM 1473, 83 APR EDITION OF 1 JAN 73 IS OBSOLETE.

UNCLASSIFIED
SECURITY CLASSIFICATION OF THIS PAGE

AFGL-TR-84-0168 SIO Ref. 85-7

THE FASCAT MODEL PERFORMANCE UNDER FRACTIONAL CLOUD CONDITIONS AND RELATED STUDIES

Richard W. Johnson
Wayne S. Hering

Visibility Laboratory
University of California, San Diego
Scripps Institution of Oceanography
La Jolla, California 92093

Approved:

Roswell W. Austin, Director
Visibility Laboratory

Approved:

William A. Nierenberg, Director
Scripps Institution of Oceanography

CONTRACT NO. F19628-82-C-0060
Project No. 7670
Task No. 7670-14
Work Unit No. 7670-14-02

FINAL REPORT
1 MAR 82 - 31 DEC 84

DECEMBER 1984

Contract Monitor
Major John D. Mill, Atmospheric Optics Branch, Optical Physics Division

Approved for public release; distribution unlimited.

Prepared for

AIR FORCE GEOPHYSICS LABORATORY
AIR FORCE SYSTEMS COMMAND
UNITED STATES AIR FORCE
HANSCOM AFB, MASSACHUSETTS 01731

AIR FORCE,86145/21-4-86 - 377

SUMMARY

This Final Report under Contract No. F19628-82-C-0060 summarizes the results of several research studies directed toward the development of models of the optical properties of the atmosphere which are suitable for the operational support of tactical weapons and sensors operating in the visible and infrared portions of the electromagnetic spectrum.

The overall contractual effort has been an integral part of the overall Air Force Geophysics Laboratory (AFGL/AFSC) program to develop a thorough understanding of atmospheric effects on visible and infrared radiation through the atmosphere, and ultimately, the concomitant limitations on the performance of electro-optical systems such as target acquisition devices and precision guided munitions.

This Final Report contains a brief review of four previously issued interim reports which were submitted during this contractual interval in support of the primary model development task. It also contains the complete documentation for the FASCAT code and a discussion of the FASCAT model performance under fractional cloud meteorological conditions.

TABLE OF CONTENTS

LIST OF TABLES AND ILLUSTRATIONS

THE FASCAT MODEL PERFORMANCE UNDER FRACTIONAL CLOUD CONDITIONS AND RELATED STUDIES

by

Wayne S. Hering and Richard W. Johnson

1.0 INTRODUCTION

This Final Report has been prepared under Air Force Geophysics Laboratory Contract No. F19628-82-C-0060 and addresses several studies related to the development of models for atmospheric optical properties within the visible and infrared portions of the electromagnetic spectrum.

Initial research studies and their subsequent reported findings are reviewed in section two of this Final Report. Section 3, the major element within this report, is reserved for a discussion of the FASCAT (Fast Atmospheric SCATtering) model in its current and most sophisticated configuration. This model, first presented in Hering (1981) has been extended to address singly and multiply scattered radiances not only under clear and fully overcast meteorological conditions, but under the more difficult and substantially more general conditions typified by fractional cloud cover.

2.0 A REVIEW OF RELATED STUDIES

There were several research studies related to visible and infrared optical properties within the lower troposphere that were conducted as part of this overall contractual effort. The subject areas ranged from the generalized development for equation of transfer formalisms, Gordon (1982), to the specific analyses of experimentally measured aerosol size distributions, Fitch (1983).

In order to briefly summarize these analysis and modelling efforts, four of the resultant scientific reports which were issued during this contract interval are reviewed in the following paragraphs. In general, the format will contain a very brief intoductory comment, followed by an abstract of the original report's primary result and/or recommendation.

2.1 AFGL-TR-82-0223: Implications of the Equation of Transfer Within the Visible and Infrared Spectrum

by Jacqueline I. Gordon

Note: Subsequent pre-publication review has modified the derivation, but not the results discussed in Section 2.1 as related to Eq. 4.17 through 4.22. See App. Opt. Vol. 24, No. 16.

Introductory Comment: As documented in a series of preceding AFGL reports which are tabulated in Appendix C, the Visibility Laboratory has conducted a substantial program of visible spectrum measurement, analysis, and modeling. The radiative transfer formalisms used in these programs have been visible spectrum oriented, and in general did not contain emission and absorption terms. This report, -0223, extends the work by including these terms in the analytic formalisms and then uses these expressions to re-evaluate previously obtained experimental measurements and assesses their use in specific modelling applications.

EQUATION OF TRANSFER
(Section 2, AFGL-TR-82-0223)

Radiance

The basic equations developed herein are monochromatic. Applicability to broadband sensors will be discussed where appropriate.

The most basic equation in radiation theory is the equation of transfer (Eq. 10 Duntley *et al.* (1957), Eq. (3) Sec. 3.15 Preisendorfer (1976), and Eq. (46) Chandrasekhar (1960))

$$dL(z,\theta,\phi)/dr = -\alpha(z)\,L(z,\theta,\phi) + L_*(z,\theta,\phi). \qquad (2.1)$$

This equation relates the incremental change in radiance $dL(z,\theta,\phi)$ at altitude z in direction zenith angle θ and azimuth ϕ over the incremental path length dr to the attenuation coefficient $\alpha(z)$, the radiance $L(z,\theta,\phi)$ and the path function $L_*(z,\theta,\phi)$. The first term is the loss term and the second is the gain term.

The attenuation or extinction coefficient $\alpha(z)$ is equivalent to the Chandrasekhar (1960) mass attenuation coefficient k times the density ρ. The attenuation coefficient is the sum of the total scattering coefficient $s(z)$ plus the absorption coefficient $a(z)$

$$\alpha(z) = s(z) + a(z). \qquad (2.2)$$

The path function $L_*(z,\theta,\phi)$ is equivalent to the Chandrasekhar (1960) mass emission coefficient j times the density ρ. The path function is the sum of a scattered component and an emitted component which is related to the absorption

$$L_*(z,\theta,\phi) = L_{*_s}(z,\theta,\phi) + L_{*_a}(z). \qquad (2.3)$$

The emitted component due to absorption is isotropic and hence is shown without direction modifiers.

Scattering

The scattering coefficient has two components. Rayleigh or molecular scattering $_{R}s$ is highly wavelength dependent being proportional to the inverse fourth power of the wavelength λ^{-4}. Mie scattering $_{M}s$ (due to atmospheric particulates) is less wavelength dependent. Both tend to be smooth continuous functions with wavelength.

The path function due to scattering is the integral of the incoming radiance $L(z,\theta',\phi')$ in all 4π directions (including the sun where appropriate) times the volume scattering function $\sigma(z,\beta')$

$$L_{*_s}(z,\theta,\phi) = \int_{4\pi} L(z,\theta',\phi')\,\sigma(z,\beta')\,d\Omega . \qquad (2.4)$$

The scattering angle β' is equivalent to the Chandrasekhar (1960) angle Θ. It is a function of the incoming radiance direction angles θ', ϕ' and the sensor direction angles θ, ϕ as follows

$$\cos\beta' = \sin\theta \sin\theta' \cos(\phi'-\phi) + \cos\theta \cos\theta' \qquad (2.5)$$

The integral of the volume scattering function over 4π is the total scattering coefficient

$$s(z) = \int_{4\pi} \sigma(z,\beta)\,d\Omega . \qquad (2.6)$$

The volume scattering function is equivalent to the Chandrasekhar (1960) phase function $p(\cos\Theta)$ times the attenuation coefficient α divided by 4π.

Absorption and Emission

Atoms and molecules in the gas phase absorb and emit in line and band spectra. The atomic spectra are line spectra and tend to be at the shorter wavelengths. The band spectra are molecular and tend to be at the longer wavelengths. The continua are essentially part of the band spectra, weak but broad spectrally.

Molecules in the liquid or solid phase cannot emit line or band spectra but can only emit in a continuous spectrum, the distribution of which is determined by the ambient temperature, in other words like a black or grey body (incomplete radiator). This implies that the absorption spectrum for liquids and solids is also continuous spectrally.

An aerosol is defined as a mixture of gas and small solid or liquid particles. Although the solid particulates and water droplets with dissolved particulates absorb and emit like a grey body with a continuous absorption spectrum, the gas or air absorbs and emits in line and band spectra. Thus the aerosol absorbs and emits like a spectral or colored body.

Emission Mechanisms. The principal emission mechanisms above the mesosphere are electroluminescence and chemiluminescence resulting in line and band spectra. These emissions are called airglow. These are important in the visible part of the spectrum at twilight and night but will not be dealt with herein.

The principle emission mechanism in the troposphere and in the atmosphere at or below the mesosphere is temperature radiation which is photon emission caused by atomic or molecular collision. The atmosphere is assumed to be in local thermodynamic equilibrium, hence Kirkhoff's law applies. The path function due to emission is thus [Eq. (38) Chandrasekhar (1960)]

$$L_{*_a}(z) = a(z)\, L(\lambda,T) \qquad (2.7)$$

where $L(\lambda,T)$ is the blackbody radiance at wavelength λ and T is the temperature in degrees Kelvin. The path function due to emittance at and below the mesosphere is highly wavelength dependent and should be dealt with monochromatically.

A black body in thermodynamic equilibrium absorbs and emits as a continuous function of wavelength and temperature according to the classical equation [Wolfe (1978) Table 1.7]

$$L(\lambda,T) = c_1 / [\pi \lambda^5 (e^x - 1)] \qquad (2.8)$$

where

$$c_1 = 2\pi hc^2 = 3.741382E-16\ Wm^2 \qquad (2.9)$$

and

$$x = c_2 / (\lambda T) . \qquad (2.10)$$

The form 3.74E-16 is an alternate format for 3.74×10^{-16}. This computer form is used throughout this report. The c is the speed of light, h is the Planck constant and

$$c_2 = ch/k = 1.438786E-2\ mK \qquad (2.11)$$

where k is the Boltzmann constant. The constants are from Driscoll and Vaughn (1978) Table A.1.

Visible Spectrum. Blackbody radiance and hence exitance (emittance) is negligible in the visible spectrum. Even at $1\,\mu m$ at 300°K (27°C or 80°F), $L(1\mu m, 300K) = 1.76E-7\ W/\Omega m^2$. At shorter wavelengths (all the visible wavelengths) and/or lower temperatures (the normal range of temperature below the mesosphere) the emittance is still less. Hence for the visible spectrum Eq. (2.3) becomes

$$L_*(z,\theta,\phi) = L_{*_s}(z,\theta,\phi) . \qquad (2.12)$$

Equilibrium Radiance

The equilibrium radiance is defined as the radiance when the incremental change in radiance over the incremental path length dL/dr equals zero, therefore from Eq. (2.1) (Eq. (11) Duntley *et al.* (1957))

$$0 = L_*(z,\theta,\phi) - \alpha(z)\, L_q(z,\theta,\phi) \tag{2.13}$$

or (Eq. (40) Chandrasekhar(1960))

$$L_q(z,\theta,\phi) = L_*(z,\theta,\phi)/\alpha(z) . \tag{2.14}$$

Thus the equilibrium radiance is equal to the Chandrasekhar (1960) source function $\mathcal{J}$.

No Absorption. In a medium or at wavelengths with no absorption, the attenuation coefficient would equal the scattering coefficient and the equilibrium radiance would be equal to

$$L_q(z,\theta,\phi) = L_{*_s}(z,\theta,\phi)/s(z) . \tag{2.15}$$

Scattering Negligible. When scattering is negligible, such as at longer wavelengths in the infrared, the attenuation is equivalent to the absorption. Substituting Eq. (2.7) into Eq. (2.14) we have

$$L_q(z,\theta,\phi) = L(\lambda,T) . \tag{2.16}$$

Equation of Transfer. An alternate form of the equation of transfer is to divide both sides by the attenuation coefficient and let dr equal $\sec\theta\ dz$ [Eq. 63 Chandrasekhar (1960)],

$$\begin{aligned}\cos\theta\, dL\ (z,\theta,\phi)\,/\,[\alpha(z)\, dz]\\ = -L(z,\theta,\phi) + L_q(z,\theta,\phi) .\end{aligned} \tag{2.17}$$

The $\cos\theta$ is equal to the Chandrasekhar (1960) function μ and $\alpha(z)\ dz$ is equal to $dt(z)$ the differential of the optical thickness $t(z)$.

DETERMINATIONS FROM THE SOLAR ALMUCANTAR

(Section 3, AFGL-TR-82-0223)

Sky Radiance

The almucantar is the part of the sky at a constant zenith angle, all azimuths. The solar almucantar is the sky at the zenith angle of the sun θ_s. The sky radiance in the solar almucantar is the path radiance out-of-the-atmosphere to the sensor at altitude z. The sky radiance can be expressed as

$$L_\infty^*(z,\theta_s,\phi) = \int_\infty^z L_*(z_i,\theta_s,\phi)\ T_{r\,i}(z,\theta_s)dr . \tag{3.1}$$

The path function $L_*(z,\theta_s,\phi)$ can be expressed in terms of a sun component, a sky-terrain component and an emitted component

$$\begin{aligned}L_*(z,\theta_s,\phi) &= {}_s\epsilon(z)\sigma(z,\beta)\\ &+ \int_{4\pi} L(z,\theta',\phi')\sigma(z,\beta')d\Omega + L_{*_a}(z) ,\end{aligned} \tag{3.2}$$

or

$$\begin{aligned}L_*(z,\theta_s,\phi) &= {}_s\epsilon(z)[\sigma(z,\beta)\\ &+ \int_{4\pi} L(z,\theta',\phi')\sigma(z,\beta')d\Omega/{}_s\epsilon(z)\\ &+ L_{*_a}(z)/{}_s\epsilon(z)] ,\end{aligned} \tag{3.3}$$

where

${}_s\epsilon(z)$ is the solar scalar irradiance at altitude z.

Let the last two terms be designated by the function $C(z)$ such that

$$C(z) = \int_{4\pi} L(z,\theta',\phi')\sigma(z,\beta')d\Omega/{}_s\epsilon(z) + L_{*_a}(z)/{}_s\epsilon(z) . \tag{3.4}$$

Substituting Eqs. (3.3) and (3.4) into Eq. (3.1) we get

$$L_\infty^*(z,\theta_s,\phi) = \int_\infty^z {}_s\epsilon(z_i)T_{r\,i}(z,\theta_s)[\sigma(z_i,\beta) + C(z_i)]dr . \tag{3.5}$$

The sun scalar irradiance and the transmittance can be expressed as a function of the sun irradiance at the top of the atmosphere ${}_s\epsilon(\infty)$ as follows

$${}_s\epsilon(z_i)T_{r\,i}(z,\theta_s) = {}_s\epsilon(\infty)\exp[-\int_\infty^{z_i} \alpha(z)dr - \int_{z_i}^{z} \alpha(z)dr] . \tag{3.6}$$

The two integrals can be combined and expressed in terms of the limits ∞ to z which is equivalent to the total transmittance, thus

$${}_s\epsilon(z_i)T_{r\,i}(z,\theta_s) = {}_s\epsilon(\infty)T_\infty(z,\theta_s) = {}_s\epsilon(z) . \tag{3.7}$$

Now substituting into Eq. (3.5), the sun irradiance can be taken out of the integral and we get

$$L_\infty^*(z,\theta_s,\phi)/{}_s\epsilon(z) = \int_\infty^z [(\sigma(z,\beta) + C(z)]dr . \tag{3.8}$$

The quantity in the square brackets is a function of altitude and not of zenith angle, therefore

$$\int_{\infty}^{z} [\sigma(z,\beta) + C(z)]dr$$

$$= [m_\infty(z,\theta_s)/m_\infty(z,0)] \int_{\infty}^{z} [\sigma(z,\beta) + C(z)]dz \ . \qquad (3.9)$$

where $m_\infty(z,\theta_s)/m_\infty(z,0)$ is the relative optical airmass at θ_s. For altitudes up to 6 kilometers we can use the sea level value for sun zenith angles 0 to 86 degrees so for convenience we will shorten this to $m(\theta_s)$. Substituting back into Eq. (3.8) we get

$$L(z,\theta_s,\phi)/[{}_s\epsilon(z)m(\theta_s)] = \int_{\infty}^{z} [\sigma(z,\beta) + C(z)]dz \ . \qquad (3.10)$$

The right hand term can be separated into two parts

$$\int_{\infty}^{z} [\sigma(z,\beta) + C(z)]dz = \int_{\infty}^{z} \sigma(z,\beta)dz + \int_{\infty}^{z} C(z)dz \ . \qquad (3.11)$$

Now let us define an optical thickness function $\tau_\infty(z,\beta)$ such that

$$\tau_\infty(z,\beta) = \int_{\infty}^{z} \sigma(z,\beta)dz \ . \qquad (3.12)$$

The integral of the optical thickness function over 4π is the optical thickness due to scattering ${}_st_\infty(z)$

$${}_st_\infty(z) = \int_{4\pi} \tau_\infty(z,\beta)d\Omega \qquad (3.13)$$

since the optical thickness due to scattering is the integral of the total scattering coefficient with altitude

$${}_st_\infty(z) = \int_{\infty}^{z} s(z)dz \ . \qquad (3.14)$$

Substituting Eq. (3.12) into Eq. (3.10) we get

$$L_\infty^*(z,\theta_s,\phi)/[{}_s\epsilon(z)m(\theta_s)] = \tau_\infty(z,\beta) + \int_{\infty}^{z} C(z)dz \ . \qquad (3.15)$$

This is the basic equation for the radiance in the solar almucantar and how it relates to the sun scalar irradiance, the optical airmass, the optical thickness function and one additive component defined by Eq. (3.4).

Optical Stability

Transmittances from Solar or Solar Almucantar Radiances

The atmosphere is considered to be optically stable when the atmospheric transmittance does not change with time. When the day is optically stable, measurements of the apparent sun radiance ${}_sL_\infty(z,\theta_s,0)$ made over a large range of sun zenith angle can yield a good measure of total transmittance $T_\infty(z,0)$ and the inherent sun radiance ${}_sL_o(\infty)$

$${}_sL_\infty(z,\theta_s,0) = {}_sL_o(\infty)T_\infty^{m(\theta_s)}(z,0) \ . \qquad (3.16)$$

Taking the log of both sides of Eq. (3.16) we get

$$\log {}_sL_\infty(z,\theta_s,0) = \log {}_sL_o(\infty) + m(\theta_s) \log T_\infty(z,0) \ . \qquad (3.17)$$

Graphs of apparent sun radiance on semi-log paper of log apparent sun radiance versus airmass yield the typical Langley (or Bouguer) graph where log inherent sun radiance is the intercept and log transmittance is the slope.

Variations of Eq. (3.15) give both another method for obtaining the total transmittance and several ways of checking the optical stability. Equation (3.15) can also be written as

$$L_\infty^*(z,\theta_s,\beta)/m(\theta_s)$$

$$= T_\infty(z,0)^{m(\theta_s)} {}_s\epsilon(\infty)[\tau_\infty(z,\beta) + \int_{\infty}^{z} C(z)dz] \ . \qquad (3.18)$$

Taking the log of both sides we get

$$\log[L_\infty^*(z,\theta_s,\beta)/m(\theta_s)] = m(\theta_s) \log T_\infty(z,0) + \log A \qquad (3.19)$$

where

$$A = {}_s\epsilon(\infty)[\tau_\infty(z,\beta) + \int_{\infty}^{z} C(z)dz] \ . \qquad (3.20)$$

For an optically stable day, A should be constant for a given angle from sun. Thus the sky radiance at a constant β in the solar almucantar can be used to obtain the beam transmittance when measured over a large range of airmass values on an optically stable day. A semi-log graph of $\log[L_\infty^*(z,\theta_s,\beta)/m(\theta_s)]$ versus airmass would be linear with a slope of log transmittance and an intercept at $\log A$. The transmittance obtained from the sun radiance using Eq. (3.17) and the transmittance obtained from the sky radiance in the solar almucantar are then averaged to obtain the most accurate value.

Tashenov (1970) used this method with measurements of the solar aureole to obtain spectral transmittance in the region 410 to 735 nanometers.

Tests to Determine Optical Stability

Pyaskovskaya-Fesenkova (1970) outlines two tests for optical stability as well as a unique equation for transmittance which is valid only for optically stable days.

The first test is to graph for a constant scattering angle the ratio $L_\infty^*(z,\theta_s,\beta)/[{}_s\epsilon(z)m(\theta_s)]$ versus $m(\theta_s)$. As can be seen from Eq. (3.15), if the day is optically stable the right hand term is constant. Therefore this graph should result in a horizontal straight line. That is, for an optically stable day

$$L_\infty^*(z,\theta_s,\beta)/[{}_s\epsilon(z)m(\theta_s)] = B \qquad (3.21)$$

where

$$B = \tau_\infty(z,\beta) + \int_\infty^z C(z)dz\ . \qquad (3.22)$$

The second test for optical stability is to graph the ratio $L_\infty^*(z,\theta_s,\beta)/{}_s\epsilon(z)$ versus relative airmass for a constant β. The graph should result in a straight line going through the origin on an optically stable day. To understand this, Eq. (3.15) is rewritten in the form

$$L_\infty^*(z,\theta_s,\beta)/{}_s\epsilon(z) = m(\theta_s)\ B\ . \qquad (3.23)$$

The B is now the slope and the intercept is zero.

If the day is optically stable a graph of solar almucantar radiance at a constant scattering angle versus airmass will yield a value of transmittance as follows. If we write Eq. (3.21) in the form

$$L_\infty^*(z,\theta_s,\beta) = {}_s\epsilon(\infty)T_\infty(z,0)^{m(\theta_s)}\ m(\theta_s)\ B \qquad (3.24)$$

and differentiate (only the sky radiance and the air mass are variables, the inherent sun scalar irradiance, B and the transmittance are constant), we get

$$dL_\infty^*(z,\theta_s,\beta)$$

$$= B\ {}_s\epsilon(\infty)T_\infty(z,0)^{m(\theta_s)}\ d\ m(\theta_s)[1 + m(\theta_s)lnT_\infty(z,0)]\ . \qquad (3.25)$$

Equation (3.25) is only valid when the angle from sun is constant, the vertical transmittance from space to sensor is constant and the day is optically stable. Setting $dL_\infty^*(z,\theta_s,\beta)$ equal to zero and rearranging we get

$$\ln T_\infty(z,0) = -1/m(\theta_s') \qquad (3.26)$$

where θ_s' is the sun angle where $L_\infty^*(z,\theta_s,\beta)$ is a maximum. Therefore a graph of solar almucantar radiance at a constant angle from the sun versus airmass will increase and then decrease with the maximum at $m(\theta_s')$ when the day is optically stable. If the curve is reasonably well defined with sufficient airmass values, a reasonable transmittance value can be obtained. It can also be used as a third test for optical stability. The values of transmittance obtained by means of Eqs. (3.17), (3.19) and (3.26) should be in agreement on an optically stable day.

Pyaskovskaya-Fesenkova (1970) describes an instrument for measuring the quantities in the preceding equations. It is essentially a radiance photometer with a three degree field of view for the solar measurement. For the aureole measurement a two degree to three degree circular zone is used. Her article also includes a theoretical test of the error in obtaining transmittance from the sun radiance when the aureole in the three degree field is necessarily a part of the sun radiance measurement. She concluded the error to be negligible.

ADDITIONAL DETERMINATIONS
(Section 4, AFGL-TR-82-0223)

Method of Obtaining Single Scattering Albedo from Horizon Sky

Roessler and Faxvog (1981) developed equations for the horizon sky luminance as a function of the single scattering albedo after assuming both an isotropic scattering function and an isotropic luminance distribution. The technique can be made more generally applicable by developing the equations for the horizon at a scattering angle of 55 degrees from the sun.

Horizon Sky at 55° from Sun

The equation for the path function at 55 degrees scattering angle can be expressed as a function of the sun component separate from the sky-terrain component in a manner similar to Eq. (3.2)

$$L_*(z,\theta,\ 55\,\beta) = {}_s\epsilon(z)\sigma(z,55)$$

$$+ \int_{4\pi} L(z,\theta',\phi')\sigma(z,\beta')d\Omega + L_{*_a}(z)\ . \qquad (4.7)$$

Substituting Eq. (4.6) into Eq. (4.7) and assuming the sky-terrain or diffuse scalar irradiance ${}_d\epsilon(z)$ is isotropic we get

$$L_*(z,\theta,\ 55\,\beta) = {}_s\epsilon(z)s(z)/(4\pi)$$

$$+ {}_d\epsilon(z)s(z)/(4\pi) + L_{*_a}(z)\ . \qquad (4.8)$$

Since the total scalar irradiance is the sun plus the sky-terrain scalar irradiance, Eq. (4.8) can be written as

$$L_*(z,\theta,\ 55\,\beta) = \epsilon(z)s(z)/(4\pi) + L_{*_a}(z)\ . \qquad (4.9)$$

Dividing both sides by the attenuation coefficient and expressing the emitted path function according to Eq. (2.7) we get an equation for the equilibrium radiance

$$L_q(z,\theta,55\beta) = \epsilon(z)s(z)/[\alpha(z)4\pi] + a(z)L(\lambda,T)/\alpha(z)\,. \tag{4.10}$$

This can be expressed in terms of the single scattering albedo ω (from Eq. (2.39)) as

$$L_q(z,\theta,55\beta) = \omega(z)\epsilon(z)/(4\pi) + [1-\omega(z)]L(\lambda,T)\,. \tag{4.11}$$

The general equation for the horizon sky radiance at 55 degrees scattering angle from Eq. (2.57) is

$$L_\infty^*(z,90,55\beta) = L_q(z,90,55\beta)[1-T_\infty(z,90)]\,. \tag{4.12}$$

Therefore from Eq. (4.11) the horizon sky radiance at 55 degrees is

$$L_\infty^*(z,90,55\beta) = \{\omega(z)\epsilon(z)/(4\pi) + [1-\omega(z)]L(\lambda,T)\}[1-T_\infty(z,90)]\,. \tag{4.13}$$

The above equation assumes that the attenuation coefficient is horizontally isotropic and therefore the horizon sky must be cloud free.

Visible Spectrum

In the visible spectrum $L(\lambda,T)$ is negligible. Also for the photopic at sea level $T_\infty(0,90)$ is negligible and Eq. (4.13) becomes

$$L_\infty^*(0,90,55\beta) = \omega(0)\epsilon(0)/4\pi\,. \tag{4.14}$$

Thus the single scattering albedo ω can be determined by measuring the horizon sky at 55 degrees and the total scalar irradiance at sea level

$$\omega(0) = L_\infty^*(0,90,55\beta)4\pi/\epsilon(0)\,. \tag{4.15}$$

Since this is an approximative method, the precision level of the resultant $\omega(0)$ is not expected to be high. However, it can still be quite useful as one measure of the single scattering albedo.

When there is no absorption $\omega = 1$ and the horizon sky should equal the average scalar irradiance $\epsilon(0)/(4\pi)$

$$L_\infty^*(0,90,55\beta) = \epsilon(0)/(4\pi)\,. \tag{4.16}$$

Method of Obtaining Scattering Transmittance from Sky Radiance Ratios at 55 Degrees

When absorption is negligible, the general equation for the equilibrium radiance at 55 degrees scattering angle Eq. (4.11) reduces to

$$L_q(z,\theta,55\beta) = \epsilon(z)/4\pi\,. \tag{4.17}$$

Also when absorption is negligible the total scalar irradiance $\epsilon(z)$ is constant with altitude, therefore the equilibrium radiance at 55 degrees is also constant with altitude. Rearranging the equilibrium radiance form of the equation of transfer Eq. (2.17) we get

$$[L(z,\theta,55\beta)-L_q(z,\theta,55\beta)]^{-1}\,dL(z,\theta,55\beta) = -s(z)dr\,, \tag{4.18}$$

where the total scattering coefficient $s(z)$ has been substituted for the attenuation coefficient since absorption is negligible. Since the equilibrium radiance is a constant Eq. (4.18) can be integrated with respect to altitude

$$\int_{L_o}^{L_r} [L(z,\theta,55\beta) - L_q(z,\theta,55\beta)]^{-1}\,dL(z,\theta,55\beta) = -\int_o^r s(z)dr\,. \tag{4.19}$$

The result of the integration is

$$L_r(z,\theta,55\beta) = L_o(z_t,\theta,55\beta)\,{}_sT_r(z,\theta) + L_q(z,\theta,55\beta)[1-{}_sT_r(z,0)] \tag{4.20}$$

where ${}_sT_r(z,\theta)$ is the transmittance due to scattering.

Sky Radiance Ratio at 55°

For sky radiance at 55 degrees scattering angle, the inherent radiance L_o is equal to zero and Eq. (4.20) becomes

$$L_\infty^*(z,\theta,55\beta) = L_q(z,\theta,55\beta)[1-{}_sT_\infty(z,\theta)]\,. \tag{4.21}$$

Now when 55 degree sky radiances at two zenith angles θ and θ' are ratioed, since the equilibrium radiance is equivalent, the sky radiance ratio is solely a function of the scattering transmittance

$$L_\infty^*(z,\theta,55\beta)/L_\infty^*(z,\theta',55\beta) = [1-{}_sT_\infty(z,0)^{m(\theta)}]\,/\,[1-{}_sT_\infty(z,0)^{m(\theta')}]\,. \tag{4.22}$$

Although Eq. (4.22) cannot be solved for directly, it can be solved by iterative means. Error analysis indicates that the zenith angle difference $\theta - \theta'$ should be large to minimize the error in the resultant vertical transmittance ${}_sT_\infty(z,0)$.

Visible Spectrum

In the visible spectrum, absorption is negligible except for ozone. The total transmittance in the visible spectrum would thus be approximated by the product of the scattering transmittance times the ozone transmittance

$$T_\infty(z,0) = {}_sT_\infty(z,0)\;{}_aT_\infty(z,0)\,. \qquad (4.23)$$

To illustrate the use of Eqs. (4.22) and (4.23), we again refer to the sky radiance and solar transmissometer data taken on the Visibility Laboratory rooftop in 1964. The atmosphere on 2 September 1964 was optically stable during the afternoon as illustrated in Section 3.3. Thus evaluation of the scattering transmittances throughout the afternoon should give us an estimate of the precision of the estimation method for broad band sensors in the visible. Equation (4.22) was evaluated for all sky radiances at 55 degrees plus or minus 2.5 degrees scattering angle for θ from 81.6 to 64.7 degrees and θ' from 64.7 to 2.8 degrees. Later error analyses indicated that some of these zenith angle combinations are less error prone than others. Hence, the averages in Table 4.1 are less accurate than can be obtained with a smaller yet better selection of zenith angle combinations. However, they are presented herein as a first approximation.

The transmittance ratios in Table 2.1 are the transmittances based on Eq. (4.22) times the ozone transmittance divided by the transmittance from the solar transmissometer. The ozone transmittance is noted at the bottom of each column. The transmittance comparison is best for Filter 1 which is a relatively narrow band filter with the least absorption. The near noon data compare least well. The accuracy is probably sufficient to warrant further development of the method to improve the precision level.

Use of sky radiances at 55 degrees scattering angle should be an improvement on the sky ratio method described in Duntley *et al.* (1972) Section 2.1 and in Duntley *et al.* (1978) Section 2.2. That method, which stemmed from the nomographic method of Kushpil' and Petrova (1971), used sky radiances at all scattering angles. Kushpil' and Petrova (1971) suggested use of ratios at 57.2 degrees scattering angle for the visible spectrum and 53.9 degrees for the near infrared portion of the spectrum but did not give a theoretical basis for the nomograph or for the selection of these angles.

Table 2.1. Comparison of transmittance determination procedures. (sky radiance ratio method *vs* solar transmissometer). (Table 4.1 from AFGL-TR-82-0223).

Nominal Sun Zenith Angle θ_s (degrees)	TOTAL TRANSMITTANCE RATIO (From Eq. (4.22, and 4.23) and Solar Transmissometer Measurements)			
	Filter 1 $\bar{\lambda} = 459$ *nm*	Filter 2 $\bar{\lambda} = 505$ *nm*	Filter 3 $\bar{\lambda} = 560$ *nm*	Filter 4 $\bar{\lambda} = 661$ *nm*
24	.954	.891	.894	.900
30	.944	.893	.894	.905
40	1.045	1.011	1.030	1.038
50	1.045	1.013	1.041	1.047
60	1.034	1.006	1.031	1.044
70	1.030	1.014	1.042	1.050
80	1.002	.998	1.031	1.045
Average	1.008	.975	.995	1.004
Standard Deviation	.043	.057	.069	.070
Ozone Contribution ${}_aT_\infty$ (0,0)	.996	.984	.969	.978

SUMMARY

(Section 5, AFGL-TR-82-0223)

Some implications of the equation of transfer as it relates to a scattering and absorbing medium have been explored. The major implication is that a measurement of the 4π radiance distribution can yield a great deal of information about the atmosphere both in the visible and the near infrared. If the solar almucantar is cloud-free the aerosol optical thickness can be derived. If the 4π radiance distribution is measured at several altitudes, the radiance arrays can be tested for consistency and, if consistent, a measure of absorption obtained. The Visibility Laboratory data catalog of radiances, both airborne and ground-based are a mine of information waiting to be tapped. This catalog is useful for testing methods of retrieval of basic scattering and absorption information about the atmosphere as well as for development of atmospheric models.

2.2 AFGL-TR-83-0236: Analytic Techniques for Estimating Visible Image Transmission Properties of the Atmosphere

by Wayne S. Hering

Introductory Comments: A fast operationally oriented technique for estimating visible spectrum contrast transmittance was introduced in Hering (1981). This 1981 report, recognized that the complexity of multiple scattering and absorption processes, in conjunction with the inherent variability of the aerosol particle distribution and composition would require effective simplifications in order that estimates of contrast transmittance through the atmosphere be made rapidly and consistently.

Thus, a series of modelling approximations that relate optical scattering properties to meteorological variables were derived from experimental data, and combined with available analytic approximations for radiative transfer calculations to develop the operational technique discussed in that report.

A subsequent report, AFGL-TR-83-0236, Hering (1983), was prepared during this current contract interval which extends the methodology of Hering (1981) to include not only clear and hazy day meteorological conditions, but full overcast cloud conditions as well. Since the work reported in Hering (1983) lays the fundamental ground work for the FASCAT model discussed in Section 3 of this Final Report, the text of the 1983 document has been included herein as Appendix A, and need not be discussed further here.

2.3 AFGL-TR-83-0270: Characteristics of Aerosol Volume Distributions Measured at Meppen, W. Germany

by Bruce W. Fitch

Introductory Comment: One of the most vexing problems facing those whose goal is the full characterization of the atmosphere's influence upon optical propagation, is the reliable specification of the aerosol size distribution. This report, AFGL-TR-83-0270 addresses this problem via the analysis of a composite data base collected by two different measuring systems, both of whose pertinent characteristics are described. The analysis uses the volume distribution methodology discussed in several earlier publications, Whitby *et al.* (1972), Shettle (1975). In the discussion, three size modes are defined as the accumulation mode (sub-micron region), the course mode (greater than 3μ region) and the middle mode (occurring at particle radii of approximately one micron). In general, log normal fits to each of the size distributions are used throughout.

A CASE STUDY

(Section 5, AFGL-TR-83-0270)

From 4 March through 13 March, 1978, Royco measurements were made several times each day around local noon. Figure 2-1 shows the values M_1, M_2, and M_3 along with wind speed, wind direction and relative humidity for these ten days. Each column in the figure represents a full 24 hr day. At the start of the series on 4 March, a large middle mode is present but there is no accumulation mode. Note that for this day, the values of M_2 are plotted on a X10 scale. A large coarse mode appears in two samples measured near 1300 hours. From 0500 hours up through 1430 hours, the time of the last sample, the relative humidity is $\geqslant 85\%$ and the wind is from the north at a speed of $\leqslant 2$ m/sec. The visible (photopic) extinction coefficient is $2.9\ \mathrm{km}^{-1}$ at 1100 hours and $1.9\ \mathrm{km}^{-1}$ at 1400 hours indicating the presence of a heavy mist or light fog. A mist is considered present when visible extinction is $> 1\ \mathrm{km}^{-1}$ and relative humidity is $> 80\%$; a fog is present when visible extinction is $\sim 4\ \mathrm{km}^{-1}$. Fig.

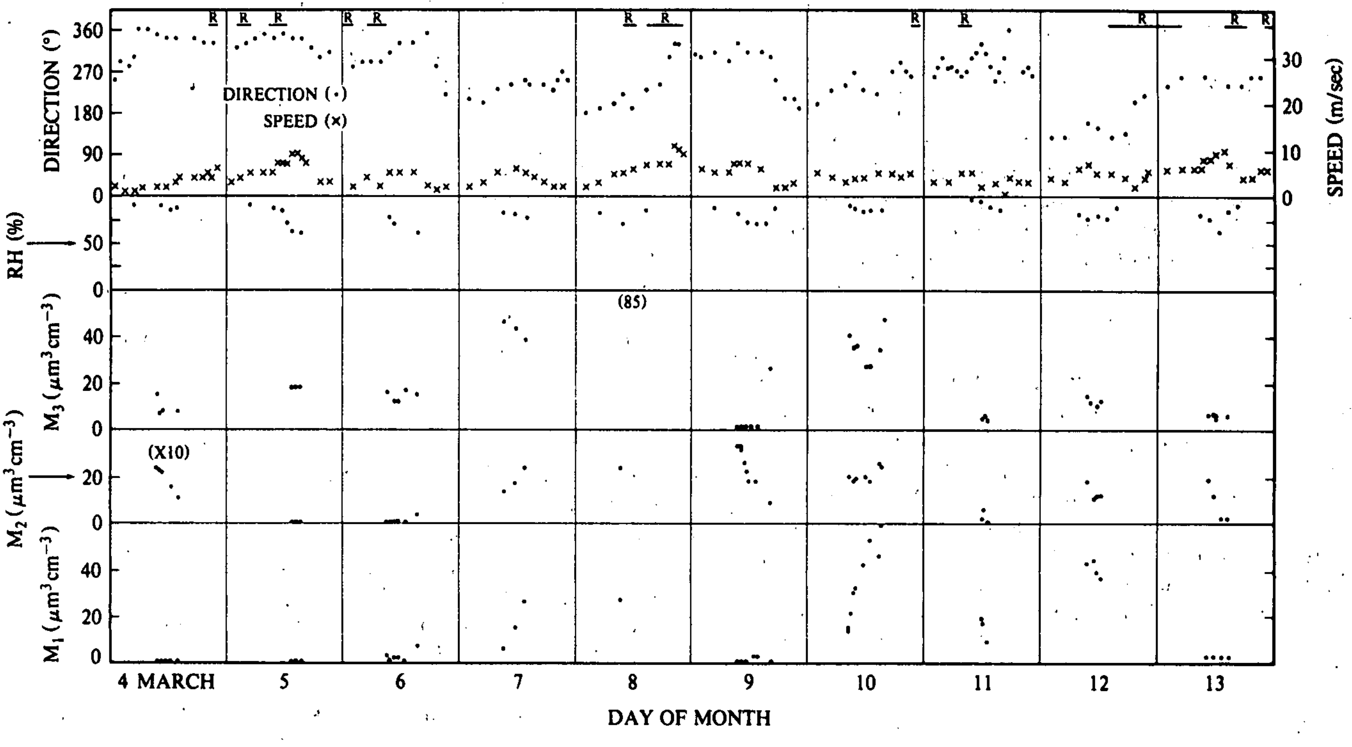

Fig. 2-1. Maximum volume concentrations *M* of the three modes with relative humidity (RH), wind direction, wind speed and periods of rain (R) for ten days in March. (Fig. 5-1 from AFGL-TR-83-0270).

2-2(a) shows the volume distribution measured four different times on 4 March. The figure shows a decrease in the volume M_2 over the time interval 1005 through 1428 hrs corresponding to a decrease in the extinction coefficient. The mist persists throughout 4 March and is gone by 0500 hours on 5 March.

The middle mode is gone by 1400 hours on 5 March. High relative humidity and visible extinction through the night of 4 March and early morning of 5 March suggest the presence of a middle mode till about 1000 hours. At this time there is a sharp increase in wind speed followed by a decrease in relative humidity. This suggests that the air parcel was dried through either vertical mixing or advection. It is likely that the drop in relative humidity to values $<65\%$ dried the middle mode. Prior to the aerosol measurements on 5 March there were three occurrences of rain. It is doubtful that the rain washed out the middle mode because measurements on several other days show a middle mode present immediately following an episode of rain. The accumulation and coarse particle modes remain fairly constant from 4 to 6 March.

There is a marked increase in the values of M_1, M_2 and M_3 on 7 March as compared to their values on 5 and 6 March. Corresponding to the change in the magnitude of the three maximum volumes, there is a shift in wind direction from 300-350° to 200-250°. The major source of aerosol in the 300-350° direction is the North Sea; whereas in the 200-250° direction there are several aerosol sources including the industrial center of Dusseldorf at about 200° and Amsterdam and the North Sea near 250°. This suggests that the accumulation and coarse particle modes are associated with an air mass from an industrial center. The middle mode, whose presence is dependent on high relative humidity, is probably a marine aerosol or, possibly, a very hydroscopic component of the accumulation mode. The three volume modes measured three times on 7 March are shown in Fig. 2-2(b). The relative humidity is $>75\%$ for the aerosol measurements on 7 March and the visible extinction is about 1 km^{-1}. During the time of aerosol measurement, the wind speed is about 5m/sec, suggesting an advection mist. Conditions on 8 March are similar to those on 7 March except $\bar{r}_3$ increases to $\sim 85 \mu m^3 cm^{-3}$. The composition of the coarse mode is not known but the modest relative humidity present at the time of measurement suggests the particles are fairly dry. Late on 8 March the wind direction shifts from around 200° to 330°.

The first measurements of 9 March show the presence of the middle mode but not the accumulation and coarse particle modes. The rapid decrease in M_2 after 1100 hours is in concert with a decrease in relative humidity. Fig. 2-2(c) shows the decrease in the size of the middle mode from 1015 to 1655 hours. The sharp decrease in relative humidity is associated with an increase in wind speed similar to what happened on 5 March at about the same time of day. In the early evening on 9 March the wind direction shifts to 200-250° and the relative humidity increses sharply. With this change, Fig. 2-2(c) shows a significant increase in the large particles at 1655 hours. The following day all three volume modes are again present.

The appearance of the three modes on 10 March with the wind from 200-250° and relative humidity $>80\%$ is similar to the situation on 7 March. Fig. 2-2(d) shows the three volume modes measured on 10 March. A measure of the visible extinction on 10 March is not available but the value of the scattering coefficient, 2.5 km^{-1}, indicates a mist. Since absorption is small at visible wavelengths, the scattering and extinction coefficient will be used interchangeably to indicate a mist or fog. An advection mist is indicated since wind speed is ≥ 3 m/sec. During 10 March, the wind direction slowly becomes more northerly indicating that the next day may show a middle mode if relative humidity is high.

On 11 March the relative humidity is $\geq 85\%$ and the wind direction is fluctuating from about 250 to 330°. The visible scattering coefficient decreases rapidly from a value of ~ 10 km^{-1} at 0500 hours to about 1 km^{-1} at 1100 hours. By 1300 hours it is about 0.6 km^{-1}. The values of M indicate that all three modes are present but in small number concentration. A small number concentration would explain why the middle mode is not large with relative humidity persisting above 85%. Thus, it appears that an advection mist was present in the morning but by midday was replaced with an air mass high in humidity and low in particle concentration.

On 12 March, the wind is from 100-160°, relative humidity is $>75\%$ and all three volume modes are present. The wind direction and large accumulation mode indicate the influence of an industrial/urban aerosol source. Late in the day the wind direction changes to 200-250° suggesting all three modes will again be present on 13 March.

Fig. 2-2(e) shows that all three modes are present on 13 March. On this day, the values of M, for the accumulation mode are smaller compared to previous cases where this mode was present for wind from 200-250°. Clean air generally associated with the passage of a cold front in conjunction with a small production of industrial particulates on Sunday, 12 March, may be responsible for $M_1 < \mu m^3 cm^{-3}$ on 13 March. A frontal passage is indicated by cooler daytime temperatures on 13 March compared to 12 March and a long period of rain during the night of 12 March. There is a sharp increase in wind speed at about 1000 hrs on 13 March followed by a decrease in relative humidity and M_2. This same meteorological phenomenon occurred on 5 and 7 March and similarly resulted in a decrease in M_2.

The ten day case study presented in Fig. 2-1 shows that a knowledge of local wind direction, wind speed and relative humidity is not always sufficient to predict the characteristics of the local aerosol size distribution. High relative humidity is important to aerosol growth but the measured volume modes are not equally affected. Particles of the middle mode are much more sensitive to changes in relative humidity than those of the other two

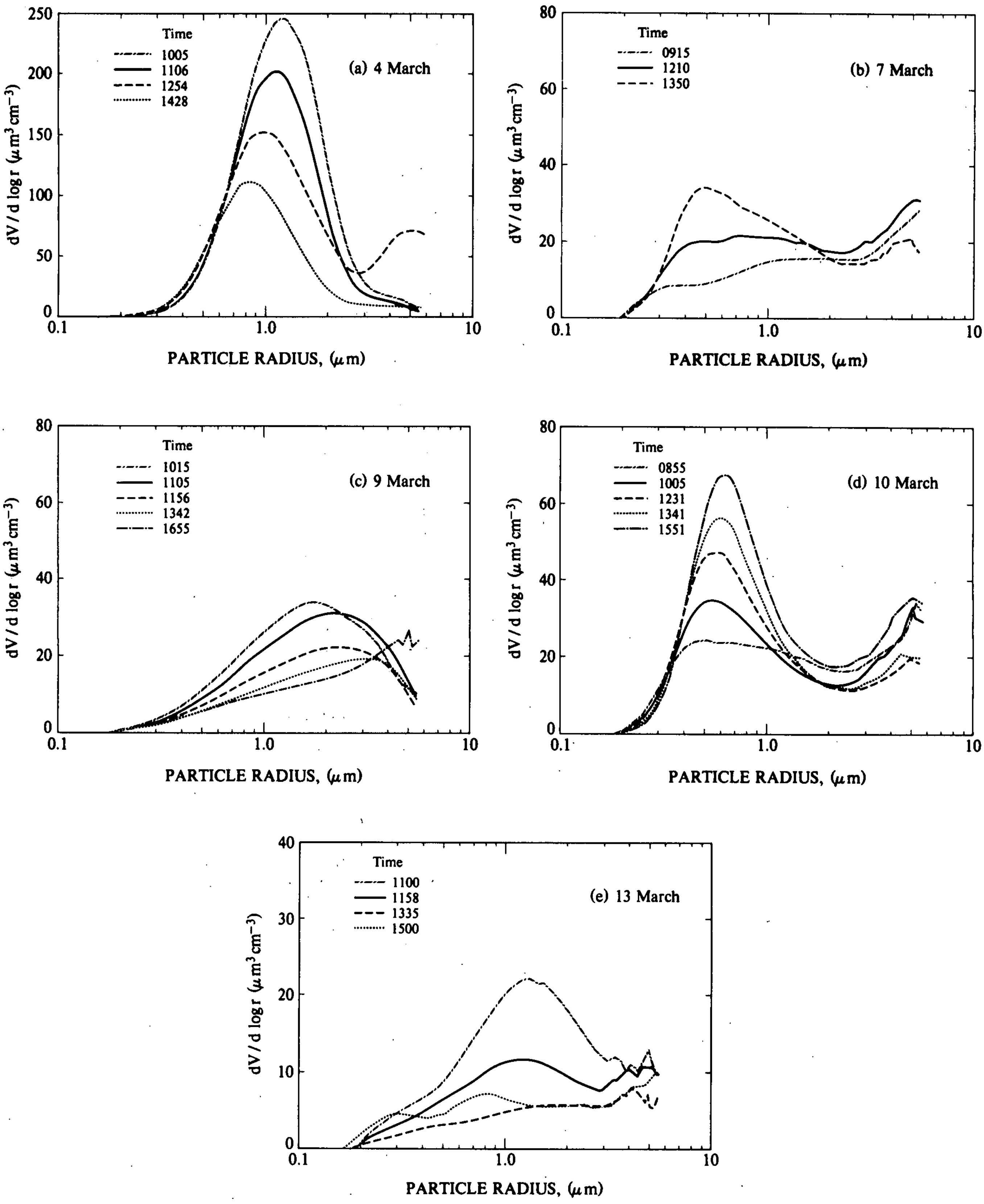

Fig. 2-2. Volume distributions sampled during the day on (a) 4 March, (b) 7 March, (c) 9 March, (d) 10 March, and (e) 13 March. Time is local time. (Fig. 5-2 from AFGL-TR-83-0270).

volume modes. The effect of an increase in relative humidity on extinction, however, not only depends on which modes are present but, also, on the initial number concentration. At Meppen, particles comprising the three modes are advected in from remote sources. Thus, an estimate of the values M cannot be based solely on a measure of the local wind direction but must, also, include an estimate of the type and strength of the downwind aerosol sources. Local sources of aerosol associated with farm operations, such as plowing and burning, may become important additional contributors during the summer months. The case study shows that a measure of local meteorology is useful for estimating the presence or absence of the three modes and for predicting changes in the values of M but is not useful for predicting the magnitudes of M.

SUMMARY & CONCLUSIONS

(Section 6, AFGL-TR-83-0270)

This report presents the results of analysis of a data base consisting of aerosol size distributions measured concurrently with the local meteorology at Meppen. The purpose of the analysis was to corroborate an extensive set of airborne aerosol measurements described in Fitch and Cress (1981 and 1983) and to determine the utility of local meteorological measurements in uniquely defining the local aerosol size and number distribution.

The characteristics and behavior of the ground measured aerosol volume distributions agree well with the airborne measured distributions. Volume distribution plots for both data sets show three volume modes, each well fit by a log-normal distribution. The behavior and values of the log-normal fit parameters for the accumulation and middle modes are in good agreement as shown in Table 2.2. The table presents the average value of standard deviation σ and the range of mode radii $\bar{r}$ for each of the three modes that appear in both the ground and airborne data bases. The greater frequency of occurrence and, generally, bigger size of the ground coarse modes compared to the airborne coarse modes indicates a larger average particle number concentration for the ground modes. The lack of agreement between σ_3 for the two data sets is probably a result of low particle counts in the airborne data and an incomplete sampling of the entire coarse mode. A fit of three log-normal curves to the measured distributions of both data sets explains more than 90% of the variance. The recurring behavior and, often, constant value of the fit parameters $\bar{r}$ and σ for the three modes show that the aerosol distribution over the measured particle radius range could be estimated using only a measure of the maximum volumes M_1, M_2, and M_3.

Table 2.2. Summary of the volume mode parameters. (Table 6.1 from AFGL-TR-83-0270).

Fit Parameters	Airborne	Ground
Accumulation		
σ_1	0.11	0.14
$\bar{r}_1$	0.25-0.5	0.25-0.6
Middle		
σ_2	0.30	0.27
$\bar{r}_2$	0.5-1.4	0.75-1.8
Coarse		
σ_3	0.2	0.33
$\bar{r}_3$	5	8.3

Concurrent measurements of the aerosol distribution and local meteorology show that the formation of large particle volumes associated with mist and fog requires high values of relative humidity. High relative humidity, however, does not always produce a large particle volume. A case study of the aerosol distribution and meteorology indicates conditions which promote high humidity do not always insure the presence of an aerosol necessary for the formation of a mist or fog. The PMS data show that the local meteorology is not a definitive predictor of aerosol presence. During a mist, the Royco data show that the aerosol distribution can be a middle mode solo or all three modes in combination. It is anticipated that as more aerosol and meteorological data become available, the task of determining the presence and characteristics of the aerosol distribution based on a measure of the meteorology will be continued. It is recommended that future studies concentrate on the behavior of the three volume modes.

The data analysis indicates that accurate short term prediction of aerosol size distribution morphisis is possible by combining methodologies of predicting local episodes of mixing and changes in relative humidity with measurements of M_1, M_2 and M_3. This technique would avoid the complexities and expense involved in developing an elaborate scheme which uses air mass trajectory analyses in conjunction with a location and time dependent aerosol source inventory. With a local measure of the values M, there would be no need to develop or maintain an aerosol source inventory or to predict changes in the aerosol distribution during long passages from its source to the site of interest. The data suggest that extinction in the visible and infrared could be predicted using LOWTRAN, a measure of the present values of M and a six to twelve hour estimate of future meteorological conditions. Such a methodology would not require a complex aerosol source inventory and could provide a mesoscale map of the optical environment when implemented over a network of meteorological stations.

2.4 AFGL-TR-84-0096: A Transportable, Machine Oriented Library of European Sky and Terrain Radiance Distributions with Contemporary Radiometric and Meteorological Profiles

by Richard W. Johnson & Miriam K. Oleinik

Introductory Comment: The radiometric and meteorological data base upon which most of the optical properties modelling discussed in previous sections of this Final Report has been based, was obtained by the C-130 mounted system described in AFGL-TR-81-0275, Johnson (1981). These data, similar in nature to much of that obtained since 1968 by the Visibility Laboratory, have not until now been readily available to the general public. A large of sample of these radiometric and meteorological measurements representing nearly 500 4π radiance distributions at 5 degree angular resolution are now in a transportable tape format.

For those readers' not familiar with the nature of these radiometric measurements, two illustrative examples are included in this Final Report, AFGL-TR-84-0168, for quick-look orientation. Data flight number C-379 was conducted south of Lolland Is., Denmark on 17 May 1976. It was a mid-day flight spanning local apparent noon under clear day meteorological conditions. The data for this flight are included in the herein described transportable library and are illustrated photographically in Fig. 2-3, and radiometrically in Fig. 2-4. Both of these figures originally appeared in AFGL-TR-81-0317 an early report analyzing the overall data set.

This report, AFGL-TR-84-0096, describes both the data base, and the tape format, with sample extraction routines included.

DESCRIPTION OF DATA BASE CONTENT

(Section 2, AFGL-TR-84-0096)

The tape-oriented data base that is discussed in this report contains two independent but related sets of measurements which are provided on several separate storage tapes whose format will be discussed in the following section. In this section, we will confine ourselves to a brief discussion of the pertinent characteristics of the measured data itself rather than that of the storage medium.

The two data sets comprising this data base are described herein as; a) the Sky and Terrain Radiance Data, and b) the Scattering Coefficient and Related Meteorological Data. For convenience, the Sky and Terrain Radiance Data will often be referred to as the "Scanner" data, and the Scattering Coefficient and Related Meteorological Data as the "Profile" data. As a general rule, the data are sorted into sub-sets identified by flight number as indicated in Tables 2.3 and 2.4.

As with all of the radiometric data associated with the reports listed in Table 2.5, the radiometric measurements contained in this data library may be characterized by the illustrative information in Fig. 2-5 and Table 2.6. More detailed information regarding the radiometric calibration procedures applied to these data is available in several preceding reports, AFCRL-70-0137, AFCRL-72-0461, and AFGL-TR-80-0207 among others and thus will not be included here.

Users should also be aware that all flight altitudes associated with these data sets are listed in meters above ground level, m(AGL), and have therefore been corrected for local meteorological conditions extant at the time of the measurements.

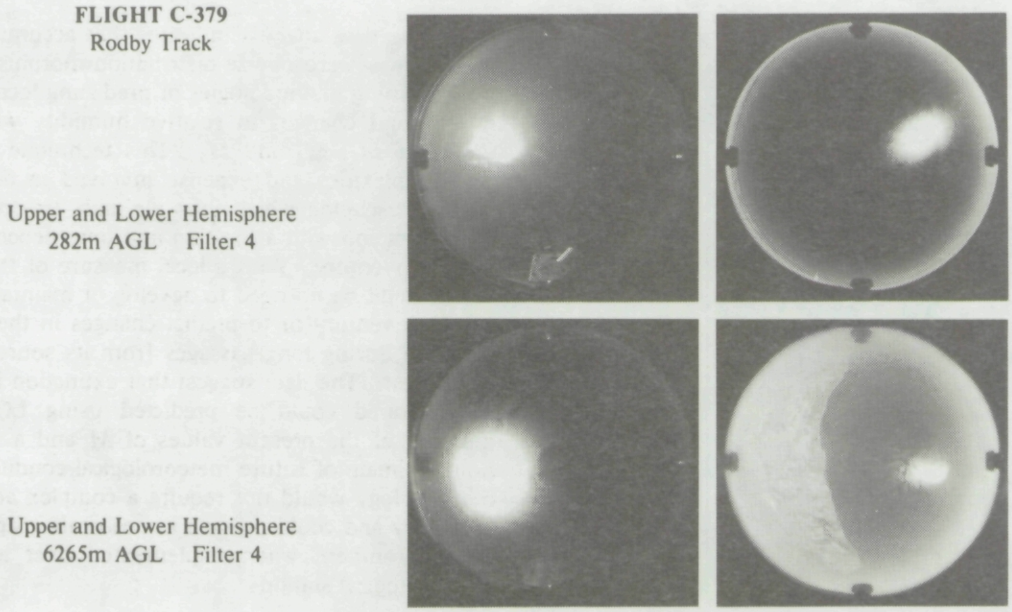

Fig. 2-3. Flight C-379 photographs from AFGL-TR-81-0317.

Table 2.3. Summary of sky and terrain radiance measurements.
(Table 1.2 from AFGL-TR-84-0096).

FLT NO	DATE	SITE*	FILTER 2 Flight Altitudes (m AGL)				AVAILABLE RADIANCE DATA Spectral Bands ($\bar{\lambda}$,*nm*)				Total Arrays	Storage Volume Number
			A	B	C	D	478	664	557	765		
	(1976)											
378	12 May	RB	282	1756	-	-	AB--	AB--	AB--	AB--	16	1
379	17 May	RB	304	1614	3170	6243	ABCD	ABCD	ABCD	A-C-	28	1
	(1976)											
390	25 Oct	RB	286	1514	3006	6079	ABCD	ABCD	ABCD	ABCD	32	1
392	1 Nov	MP	436	1176	-	-	AB--	AB--	AB--	AB--	16	1
393	2 Nov	MP	309	-	-	-	A---	----	----	----	2	1
394	18 Nov	RB	220	943	-	-	AB--	AB--	AB--	AB--	16	1
396	22 Nov	MP	313	-	-	-	A---	A---	A---	A---	8	1
399	3 Dec	BR	673	1592	2832	-	AB--	AB--	ABC-	ABC-	20	1
400	4 Dec	BR	691	-	-	-	A---	A---	----	----	4	1
401	5 Dec	BR	530	1024	2209	5297	ABCD	ABCD	ABCD	ABCD	32	1
402	6 Dec	BR	642	1585	-	4050	AB-D	AB-D	AB-D	AB-D	24	1
	(1977)											1
410	4 Jul	BR	394	1615	3181	-	ABC-	-BC-	ABC-	ABC-	22	1
411	6 Jul	BR	421	1633	2878	-	ABC-	ABC-	ABC-	ABC-	24	1
412	7 Jul	BR	353	1650	2873	-	ABC-	ABC-	----	----	12	1
415	29 Jul	MP	218	848	-	-	AB--	AB--	AB--	AB--	16	1
416	1 Aug	RB	281	1549	3086	4579	ABCD	-BCD	ABC-	ABC-	26	1
419	4 Aug	MP	245	743	-	-	AB--	AB--	AB--	AB--	16	1
421	10 Aug	RB	283	1564	3394	5843	ABCD	ABCD	ABCD	ABCD	32	1
422	11 Aug	RB	333	1569	-	-	AB--	AB--	AB--	AB--	16	1
	(1978)											
431	1 Feb	TR	271	1503	3056	-	ABC-	AB--	----	----	10	2
434	18 Feb	SG	295	1602	3109	6112	ABCD	ABCD	ABCD	AB-D	30	2
435	23 Feb	BK	466	2284	-	-	AB--	AB--	AB--	-B--	14	2
436	23 Feb	BK	435	2099	-	-	AB--	AB--	AB--	AB--	16	2
437	27 Feb	BK	509	1538	3087	5155	ABCD	ABCD	ABCD	ABCD	32	2
438	1 Mar	BK	458	1619	-	-	AB--	AB--	----	----	8	2
439	1 Mar	BK	523	1621	-	-	AB--	AB--	AB--	AB--	16	2
440	2 Mar	BK	517	1664	2877	4095	ABCD	ABCD	ABCD	ABCD	32	2
443	9 Mar	ML	299	926	-	-	AB--	AB--	AB--	AB--	16	2
444	11 Mar	YO	253	714	2171	-	ABC-	ABC-	ABC-	ABC-	24	2
446	15 Mar	YO	207	855	-	-	AB--	AB--	AB--	AB--	16	2
449	18 Mar	YO	257	1029	2454	4595	ABCD	ABCD	A---	A---	20	2
450B	22 Mar	SO	312	1055	-	-	AB--	AB--	AB--	AB--	16	2
454	28 Mar	RB	266	1194	2694	4240	ABCD	ABCD	ABCD	ABCD	32	2
456A	31 Mar	RB	294	886	-	-	AB--	AB--	AB--	AB--	16	2
	(1978)											
462	5 Aug	TR	269	1791	3730	6146	ABCD	AB-D	ABCD	-BCD	28	3
463	7 Aug	TR	276	1819	3674	6083	ABC-	ABCD	ABCD	ABCD	30	3
465	14 Aug	MP	254	1460	-	-	AB--	AB--	AB--	AB--	16	3
466	15 Aug	MP	202	1158	2953	6005	ABCD	ABCD	ABCD	ABC-	30	3
467	18 Aug	SO	250	698	2284	4717	ABCD	ABC-	-BCD	-BCD	26	3
468	21 Aug	MP	263	1349	3103	5850	ABC-	ABCD	ABCD	ABCD	30	3
469	22 Aug	SO	277	747	2475	5838	ABCD	ABCD	ABCD	ABCD	32	3
471	11 Sep	BK	45	535	-	-	AB--	AB--	AB--	AB--	16	3
473	11 Sep	BK	277	852	-	-	AB--	AB--	AB--	AB--	16	3
475	15 Sep	YO	325	933	3070	6135	ABCD	ABCD	AB--	ABC-	26	3
476	16 Sep	YO	324	1008	3085	6150	ABCD	ABCD	ABCD	ABCD	32	3
477	18 Sep	YO	310	623	3481	-	ABC-	ABC-	ABC-	ABC-	24	3
479	26 Sep	RB	307	878	2437	4620	ABCD	ABCD	ABCD	ABCD	32	3

Note: The nominal flight altitudes listed in columns 4 through 7, *i.e.* the altitudes associated with each of the filter 2 measurements, are coded in columns 8 through 11 to designate those altitudes at which additional spectral data are available. Thus for flight 378, the entries "AB--" in columns 8 through 11 indicate that measurements in each of the four spectral bands were made at each of two flight altitudes, A=282m and B=1756m.

*Site Codes
BK - Birkhof, Germany
BR - Bruz, France
ML - Mildenhall, England
MP - Meppen, Germany
RB - Rodby, Denmark
SG - Sigonella, Sicily
SO - Soesterberg, Netherlands
TR - Trapani, Sicily
YO - Yeovilton, England

Table 2.4. Summary of atmospheric vertical profile measurements.
(Table 1.3 from AFGL-TR-84-0096).

FLT NO	DATE	SITE*	FLIGHT ALTITUDES m(AGL) (1)		AVAILABLE SCAT. COEFF. DATA				STORAGE VOLUME NUMBER
					SPECTRAL BANDS, (λ̄, nm)				
			MIN	MAX	478	664	557	765	
	(1976)								
378	12 May	RB	270	1800	Y	Y	Y	Y	4
379	17 May	RB	270	6270	Y	Y	Y	Y	4
	(1976)								
390	25 Oct	RB	300	6090	Y	Y	Y	Y	4
400	4 Dec	BR	480	5100	N	Y	Y	Y	4
401	5 Dec	BR	390	5190	Y	Y	Y	Y	4
402	6 Dec	BR	390	3900	N	Y	Y	Y	4
	(1977)								
410	4 Jul	BR	120	3180	Y	Y	Y	Y	4
411	6 Jul	BR	150	2850	Y	Y	Y	Y	4
412	7 Jul	BR	120	5640	Y	Y	Y	Y	4
421	10 Aug	RB	120	5850	Y	Y	Y	Y	4
422	11 Aug	RB	120	1560	Y	Y	Y	Y	4
	(1978)								
431	1 Feb	TR	90	4560	Y	Y	Y	Y	4
435	23 Feb	BK	90	2310	Y	Y	Y	Y	4
436	23 Feb	BK	120	2040	Y	Y	Y	Y	4
437	27 Feb	BK	90	5160	Y	Y	Y	Y	4
439	1 Mar	BK	30	1650	Y	Y	Y	Y	4
444	11 Mar	YO	120	2460	Y	Y	Y	Y	4
446	15 Mar	YO	90	870	Y	Y	Y	Y	4
467	18 Aug	SO	90	4710	Y	Y	Y	Y	4
468	21 Aug	MP	30	6210	Y	Y	Y	Y	4
469	22 Aug	SO	90	5880	Y	Y	Y	Y	4
471	11 Sep	BK	30	540	Y	Y	Y	Y	4
473	11 Sep	BK	30	870	Y	Y	Y	Y	4
475	15 Sep	YO	30	6180	Y	Y	Y	N	4
476	16 Sep	YO	30	6150	Y	Y	Y	Y	4

Meteorological data is included for all flights.

Note: (1) Max-Min altitudes are nominal and coincide with those listed in previously published references. They do not include extrapolations to ground level nor to arbitrary top altitudes.

*Site Codes
BK - Birkhof, Germany
BR - Bruz, France
ML - Mildenhall, England
MP - Meppen, Germany
RB - Rodby, Denmark
SG - Sigonella, Sicily
SO - Soesterberg, Netherlands
TR - Trapani, Sicily
YO - Yeovilton, England

Table 2.5. OPAQUE related aircraft data reports.
(Table 1.1 from AFGL-TR-84-0096).

Report No.	Deployment		Data Type
	Series	Date	
AFGL-TR-77-0078	I	Spr. '76	Scatt. Coeff. Profiles & Rel. Meteor.
AFGL-TR-77-0239	II	Fall '76	Scatt. Coeff. Profiles & Rel. Meteor.
AFGL-TR-78-0168	III	Sum. '77	Scatt. Coeff. Profiles & Rel. Meteor.
AFGL-TR-79-0159	IV	Win. '78	Scatt. Coeff. Profiles & Rel. Meteor.
AFGL-TR-80-0207	V	Sum. '78	Scatt. Coeff. Profiles & Rel. Meteor.
AFGL-TR-80-0192	I, II, III	See Above	Aerosol Size Dist. and Analysis
AFGL-TR-81-0154	IV, V	-	Scatt. Coeff. Very Low Alt. Profiles
AFGL-TR-81-0237	I, II, III	-	Scatt. Coeff. Very Low Alt. Profiles
AFGL-TR-81-0275	II, III, V	-	Sky and Terrain Radiances
AFGL-TR-81-0317	I-V	-	Variations in Sky and Terr. Radiances
AFGL-TR-82-0049	IV, V	-	Review of Opt. Prop. & Aerosols

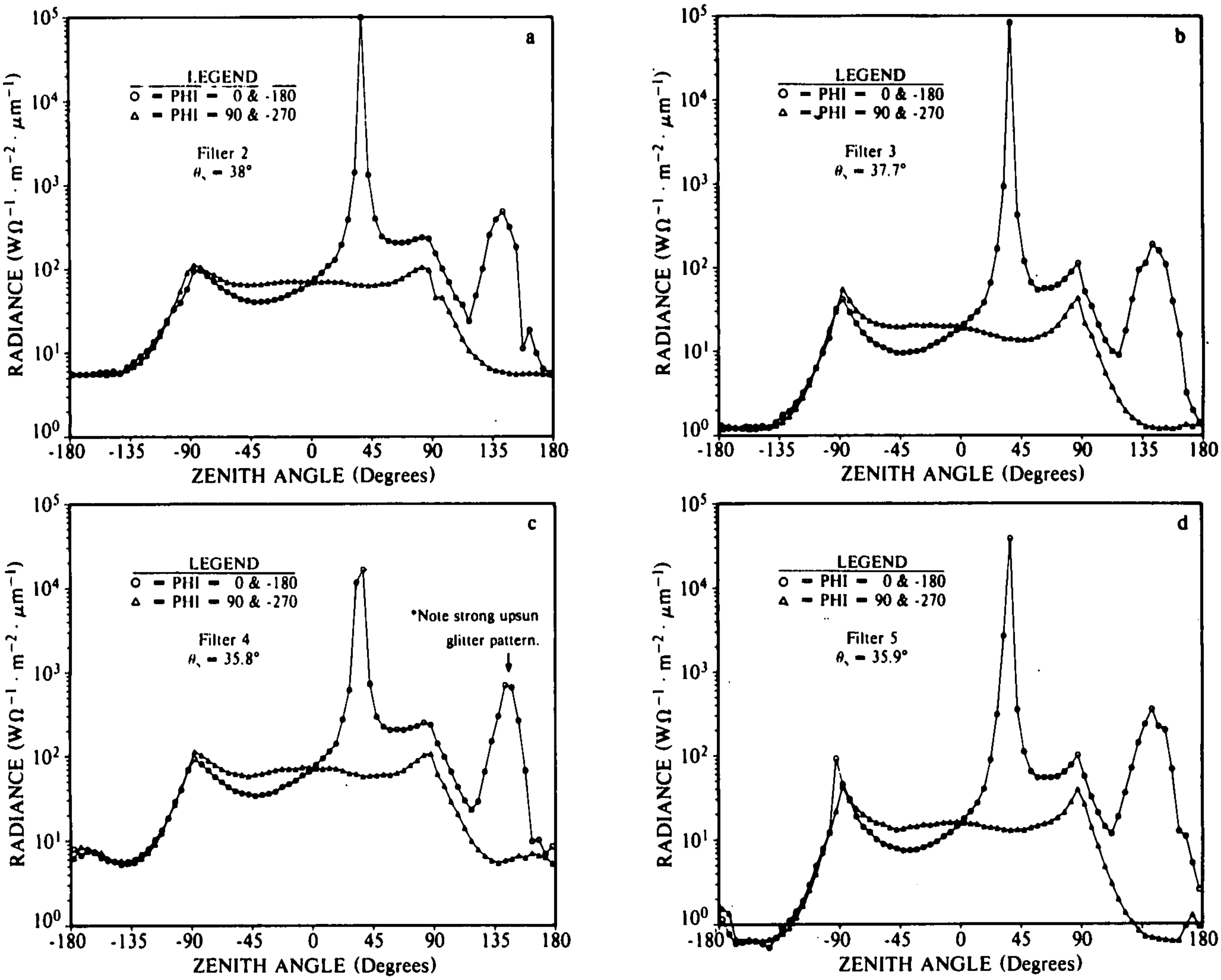

Fig. 2-4. Flight C-379 (Rodby, Denmark), clear sky over ocean with glitter, 300 m AGL. (Fig. 3-7 from AFGL-TR-81-0317).

Table 2.6. Spectral characteristics summary for AVIZ filters. (Table 2.1 from AFGL-TR-84-0096).

Spectral Characteristics				Inherent Sun Properties [Johnson (1954)]			Rayleigh Atmosphere Properties (15°C)		
Filter Code No.	Peak Wavelength (nm)	Mean Wavelength (nm)	Effective Passband (nm)	Irradiance ($W/m^2\mu m$)	Radiance ($W/\Omega m^2 \mu m$) Average	Radiance ($W/\Omega m^2 \mu m$) Center	Attenuation Length (m)	Total Scattering Coefficient (per m)	Vertical Radiance Transmittance
2	475	478	19.9	2.14E+03	3.13E+07	4.07E+07	4.84E+04	2.07E-05	0.839
3	660	664	30.2	1.57E+03	2.30E+07	2.75E+07	1.86E+05	5.41E-06	0.955
4	550	557	78.5	1.90E+03	2.78E+07	3.47E+07	8.93E+04	1.15E-05	0.907
5	750	765	50.4	1.23E+03	1.80E+07	2.10E+07	3.28E+05	3.08E-06	0.974

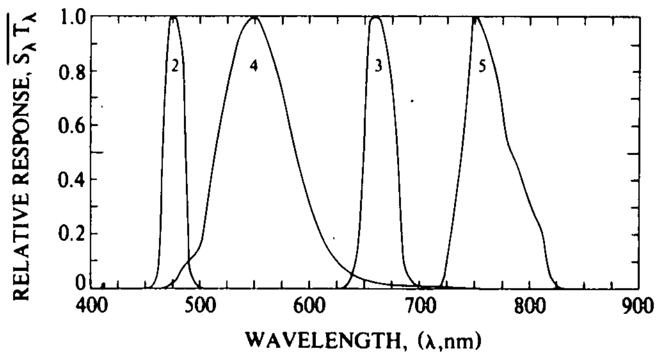

Fig. 2-5. Standard spectral responses. Peak wavelengths are: 2=475nm (Blue), 3=660nm (Red), 4=550nm (Photopic), 5=750nm (NIR). (Fig. 2-1 from AFGL-TR- 84-0096).

Sky and Terrain Radiance Data

As discussed in Johnson (1981) and Johnson and Hering (1981), both of which should be considered companion reports to this current effort, a data set containing nearly 500 arrays representing measurements of sky and terrain radiance values has been developed for general application to image propagation studies within the lower troposphere. The arrays have been organized for storage by flight number primarily, although date and site are also listed in the header information as will be noted in Section 3. As a general rule, the scanner data arrays are organized as illustrated in Table 2.7.

Each of the individual arrays indicated in Table 2.7 contains 1080 data points representing either an upper or lower hemisphere radiance distribution. Each data point represents the apparent radiance of the sky or terrain as "seen" by the 5°FOV of one of the airborne scanning radiometers described in Johnson (1981). There is a data point for every 6° in azimuth and every 5° in zenith angle within each hemisphere. All azimuth notations are taken with respect to the sun as illustrated in Fig. 2-6. It should be noted that for each entry in the data summary listed in Table 2.3, there are two data arrays in the library, one for the upper hemisphere radiances, and one for the simultaneously measured lower hemisphere radiances.

The radiance values included in this data library are the same as those used to create the graphical displays included in Johnson (1981), and Johnson and Hering (1981), and should be used with the same caveats.

THE DATA ARRAYS CONTAINED IN THIS LIBRARY HAVE NOT BEEN CORRECTED FOR THE NEAR SUN STRAY LIGHT EFFECTS AS RECOMMENDED IN SECTION 4 OF JOHNSON (1981), AFGL-TR-81-0275.

An example of the clear day sky and terrain radiance distributions that may be extracted from these data arrays is shown in Appendix A for flight C-379. These graphical displays have been abstracted from Johnson and Hering (1981) as a convenient reference for the reader.

Table 2.7. Sky & Terrain Radiance Data Organization Per Flight. (Table 2.2 from AFGL-TR-84-0096.

I. Flight Identification: Flight No., Date, Site, etc.
  A. Altitude Number One (See Table 1.2)
    1. Spectral Band No. 2 (see Fig. 2-1)
      a. Upper Hemisphere Radiance Array
      b. Lower Hemisphere Radiance Array
    2. Spectral Band No. 3
      a. Upper Hemisphere Radiance Array
      b. Lower Hemisphere Radiance Array
    3. Spectral Band No. 4
      a. Upper Hemisphere Radiance Array
      b. Lower Hemisphere Radiance Array
    4. Spectral Band No. 5
      a. Upper Hemisphere Radiance Array
      b. Lower Hemisphere Radiance Array
  B. Altitude Number Two
    1. 2. 3. 4. } *same as in "A" above*
  C. Altitude Number Three
    1. 2. 3. 4. } *same as in "A" above*
  D. Altitude Number Four
    1. 2. 3. 4. } *same as in "A" above*

The software required to create these displays is not included as part of this report.

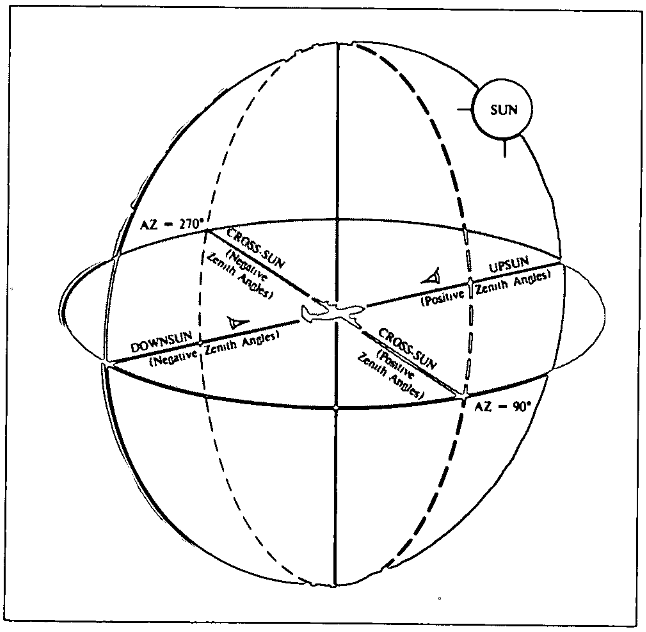

Fig. 2-6. Sky and terrain coordinate system. (Fig. 2-2 from AFGL-TR-84-0096). GREEN

Vertical Profile Data

During each of the data flights listed in Table 2.3, there were radiometric and meteorological measurements conducted at fixed altitudes as well as during ascent and descent modes. The data which were associated with the ascents and descents of the aircraft have been processed and reported in a series of preceding reports which are listed in Table 2.5. However, most of these ascent and descent data, *i.e.* profile data, are also included as part of the general purpose library described herein. These profile data, summarized in Table 2.4, are contained on a separate data tape from the radiance arrays and thus can be conveniently used either with or without the larger radiance data set.

As with the scanner radiance data, these profile data also have been organized for storage by flight number. The data available for each flight is summarized in Table 2.8. Due to a variety of data processing problems, there is not an exact one to one correspondence between the scanner and profile data sets listed in Tables 2.3 and 2.4. The raw data for exact correspondence exists on original storage tapes, but has not been fully retrieved for inclusion in this library.

It should be noted, as discussed in the earlier report series listed in Table 2.5, that the profile measurements were often made over a substantial period of time, and thus represent the spatial and temporal variabilities occurring along a flight track roughly 20 to 30 miles long, over a period of 30 to 120 minutes in time. A brief description of the flight profile used to collect these data has been abstracted from AFGL-TR-80-0207, Johnson and Gordon (1980) and is reproduced as Appendix C.

The radiometric portion of the profile data contains measurements of total volume scattering coefficient as a function of altitude in each of the spectral bands indicated in Table 2.4.

Table 2.8. Scattering coefficient & related meteorological data organization per flight. (Table 2.3 from AFGL-TR-84-0096).

I. Flight Identification: Flight No., Date, Site, etc.
  A. Profile No. 1 (Ascent) (See Appendix C, Fig. C-1)
    1. Scatt. Coeff. in Spectral Band No. 2 (See Fig. 2-1)
    2. Ambient Temperature
    3. Dewpoint/Frostpoint Temperature
    4. Relative Humidity (computed)
    5. Absolute Pressure
    6. Atmospheric Density (computed)
    7. Real Time
  B. Profile No. 2 (Descent)
    1. Scatt. Coeff. in Spectral Band No. 3
    2. to 7. } *same as in "A" above*
  C. Profile No. 3 (Ascent)
    1. Scatt. Coeff. in Spectral Band 4
    2. to 7. } *same as in "A" above*
  D. Profile No. 4 (Descent)
    1. Scatt. Coeff. in Spectral Band 5
    2. to 7. } *same as in "A" above*

The meteorological portion of the profile data contains measurements of ambient temperature, dewpoint/frostpoint temperature, and absolute pressure. The meteorological measurements were made simultaneously with the radiometric set, and are thus listed in association with a specific spectral band for temporal synchronization, although real time data at one second intervals were also included in the original raw data sets.

In both sets, the specific altitude above ground level has been calculated from measurements of absolute atmospheric pressure, and the mean ground elevation as determined from local navigation charts.

Although the profile data points are all listed at even 30m altitude intervals, users should be aware that the data values represent the average of several measurements taken throughout that interval. Scattering coefficient measurements were collected at a rate of four samples per second, and meteorological data were collected at a rate of two samples per second during all ascents and descents. The aircrafts average rate of ascent/descent throughout the lower 3 km AGL was approximately 1200 feet per minute (~6 meters/sec).

Also included in the profile data listings are values for several derived quantities. Relative humidity has been calculated from the ambient and dewpoint/frostpoint temperature measurements, and atmospheric density has been calculated from the temperature and pressure measurements.

An example of the measured profile data for flight C-379 is illustrated in Appendix B. These plots of scattering coefficient, ambient temperature and computed relative humidity have been abstracted from AFGL-TR-77-0078, Duntley *et al.* (1977). The software for producing these plots is not included as part of this report.

Users should also note that the profile listings in this library do not include extrapolations above or below the last measured data point. Thus those data points reported in previous reports (Table 2.5) which were parenthetical *i.e.* representing extrapolations, are not present in this data library. Deletions from the original data base for instrumentation reasons are likewise zeroed out, and have not been re-interpolated.

THE DATA LISTINGS CONTAINED IN THIS LIBRARY HAVE NOT BEEN CORRECTED FOR THE HIGH ALTITUDE BIAS INDUCED BY INCOMPLETE AERODYNAMIC PURGING OF THE AIRBORNE INTEGRATING NEPHELOMETER AS DISCUSSED IN SECTION 2.3 OF JOHNSON AND FITCH (1981), AFGL-TR-82-0049.

2.5 REFERENCES (FOR SEC. 2)

Chandrasekhar, S. (1960), in *Radiative Transfer*, Dover Pub. Inc., New York.

Driscoll, W.G. and W. Vaughn (1978), in *Handbook of Optics*, McGraw Hill, New York, N.Y.

Duntley, S.Q., A.R. Boileau, and R.W. Preisendorfer (1957), "Image Transmission by the Troposphere. I," *J. Opt. Soc. Am.*, **47**, pp. 499-506.

Duntley, S.Q., R.W. Johnson, J.I. Gordon, and A.R. Boileau (1970), "Airborne Measurements of Optical Atmospheric Properties at Night," SIO Ref. 70-7, AFCRL-70-0137, NTIS No. AD 870 734, University of California, San Diego, Scripps Institution of Oceanography, Visibility Laboratory.

Duntley, S.Q., R.W. Johnson, and J.I. Gordon (1972), "Airborne Measurements of Optical Atmospheric Properties, Summary and Review," SIO Ref. 72-82, AFCRL-72-0593, NTIS No. ADA 754 898, University of California, San Diego, Scripps Institution of Oceanography, Visibility Laboratory.

Duntley, S.Q., R.W. Johnson, and J.I. Gordon (1972), "Airborne and Ground-Based Measurements of Optical Atmospheric Properties in Central New Mexico," SIO Ref. 72-71, AFCRL-72-0461, NTIS No. ADA 751 936, University of California, San Diego, Scripps Institution of Oceanography, Visibility Laboratory.

Duntley, S.Q., R.W. Johnson, and J.I. Gordon (1977), "Airborne Measurements of Atmospheric Volume Scattering Coefficients in Northern Europe, Spring 1976," SIO Ref. 77-8, AFGL-TR-77-0078, NTIS No. ADA 046 290, University of California, San Diego, Scripps Institution of Oceanography, Visibility Laboratory.

Duntley, S.Q., R.W. Johnson, and J.I. Gordon (1978), "Airborne Measurements of Optical Atmospheric Properties, Summary and Review III," SIO Ref. 79-5, AFGL-TR-78-0286, NTIS No. ADA 073 121, University of California, San Diego, Scripps Institution of Oceanography, Visibility Laboratory.

Fitch, B.W. and Ted S. Cress (1981), "Measurements of Aerosol Size Distributions in the Lower Troposphere over Northern Europe," *J. Appl. Meteor.*, **20**, pp. 1119-1128. Also issued as University of California, San Diego, Scripps Institution of Oceanography, Visibility Laboratory, SIO Ref. 81-18, AFGL-TR-80-0192, NTIS NO. ADA 104 272.

Fitch, B.W. (1983), "Characteristics of Aerosol Volume Distribution Measured at Meppen, W. Germany," SIO Ref. 84-9, AFGL-TR-83-0270, University of California, San Diego, Scripps Institution of Oceanography, Visibility Laboratory.

Fitch, B.W. and Ted S. Cress (1983), "Spatial and Temporal Variations of Tropospheric Aerosol Volume Distributions," *Clim. Appl. Meteor.*, **22**, pp. 1262-1269.

Gordon, J.I. (1982), "Implications of the Equation of Transfer Within the Visible and Infrared Spectrum," SIO Ref. 83-10, AFGL-TR-82-0223, NTIS No. ADA 133-979, University of California, San Diego, Scripps Institution of Oceanography, Visibility Laboratory.

Hering, W.S. (1981), "An Operational Technique For Estimating Visible Spectrum Contrast Transmittance," SIO Ref. 82-1, AFGL-TR-81-0198, ADA 111 823, University of California, San Diego, Scripps Institution of Oceanography, Visibility Laboratory.

Hering, W.S. (1983), "Analytic Techniques for Estimating Visible Image Transmission Properties of the Atmosphere," SIO Ref. 84-6, AFGL-TR-83-0236, University of California, San Diego, Scripps Institution of Oceanography, Visibility Laboratory.

Johnson, F.S. (1954), "The Solar Constant," *J. Meteor.*, **11**, pp. 431-439.

Johnson, R.W. and J.I. Gordon (1980), "Airborne Measurements of Atmospheric Volume Scattering Coefficients in Northern Europe, Summer, 1978," SIO Ref. 80-20, AFGL-TR-80-0207, NTIS No. ADA 097 134, University of California, San Diego, Scripps Institution of Oceanography, Visibility Laboratory.

Johnson, R.W. and B.W. Fitch (1981), "A Review of Measured Atmospheric Optical Properties and Their Contemporary Aerosol Size Distributions," SIO Ref. 82-22, AFGL-TR-82-0049, NTIS No. ADA 123 940, University of California, San Diego, Scripps Institution of Oceanography, Visibility Laboratory.

Johnson, R.W. and W.S. Hering (1981), "An Analysis of Natural Variations In European Sky and Terrain Radiance Measurements," SIO Ref. 82-6, AFGL-TR-81-0317, NTIS No. ADA 120 487, University of California, San Diego, Scripps Institution of Oceanography, Visibility Laboratory.

Johnson, R.W. (1981), "Airborne Measurements of European Sky and Terrain Radiances," SIO Ref. 82-2, AFGL-TR-81-0275, NTIS No. ADA 114 637, University of California, San Diego, Scripps Institution of Oceanography, Visibility Laboratory.

Kushpil, V.I. and L.F. Petrova (1971), "Determination of the Atmospheric Transmittance from Sky Brightness Distribution," *Optical Technology*, **38**, no. 4, pp. 191-193.

Preisendorfer, R.W. (1976), *Hydrological Optics Vols. I and II,* U.S. Department of Commerce, NOAA, ERL, Honolulu, Hawaii.

Pyaskovskaya-Fesenkova, E.V. (1970), "Determining the Transmission Coefficient and Degree of Optical Stability of the Earth's Atmosphere," in *Atmospheric Optics*, ed. Nikolai B. Divari and translated by S.B. Dresner, Consultants Bureau, pp. 151-156, Plenum Press, New York, N.Y..

Roessler, D.M. and F.R. Faxvog (1981), "Visibility in Absorbing Aerosols," *Atmospheric Environment*, **15**, pp. 151-155.

Shettle, E.P. (1975), "Comment on "Atmospheric Aerosol Size Spectra, Rapid Concentration Fluctuations and Bimodality", by T.E. Graedel and J.P. Franey," *J. Geophys. Res.*, **80**, pp. 3050-3051.

Tashenov, B.T. (1970), "Spectrophotometric Studies of Atmospheric Transmittance and Stability," in *Atmospheric Optics*, ed. Nikolai B. Divari and translated by S.B. Dresner, Consultants Bureau, pp. 70-79, Plenum Press, Inc., New York.

Whitby, K.T., R.B. Husar, and B.Y.H. Liu (1972), "The Aerosol Size Distribution of Los Angeles Smog," *J. Colloid and Interface Sci.*, **39**, pp. 177-204.

Wolfe, W.L. "Radiation Theory," in *The Infrared Handbook*, ed. W.L. Wolfe and G.J. Zissis, U.S. Government Printing Office, Washington, D.C..

3.0 A REVIEW OF FASCAT DEVELOPMENT AND STATUS

The development of techniques for the practical determination of the atmospheric effects on visible image transmission is a central aspect of the optical measurement and analysis program. The objective is to establish computational techniques that are general enough and fast enough to cover a broad span of real-time field applications, yet accurate enough to utilize effectively all available data that are relevant to the calculations. Studies over the past few years have produced a fast atmospheric scattering model (FASCAT) for direct determination of the apparent spectral radiance of distant objects and backgrounds. It represents a natural extension to the overall Visibility Laboratory program of theoretical and experimental research into the structure and behavior of atmospheric optical properties.

The development and testing of the basic multiple scattering model for calculating background radiance fields from conventional meteorological observations and environmental data are described in two previous reports (Hering, 1981, and Hering, 1983). For ready reference, the second of these reports is included as Appendix A of this report. It provides background information on the modeling procedures established for the contrast transmittance calculations and describes performance tests involving comparisons with calculations derived from other radiative transfer models and comparisons with measured radiance data gathered in a wide range of environmental conditions.

Recent refinements and additions to FASCAT have increased the scope of applications that can be addressed with the modeling procedures. Building upon techniques for radiance field calculations in clear and overcast sky conditions, approximate solutions are introduced for dealing with the determination of image transmission characteristics in partly cloudy atmospheres. As described in Section 3.1, solutions are obtained as a function of cloud amount for the conventional types of high, middle, and low clouds.

In a model extension described in Section 3.2, analytic techniques are introduced for the direct calculation of inherent target radiance as determined from the intrinsic target properties and the calculated irradiance distribution. When combined with calculations of directional path radiance and beam transmittance, this model extension provides companion calculations of the apparent spectral radiances of both target and background along any predetermined slant path, and in turn the apparent target contrast at the point of observation.

Other modifications to FASCAT involve substantial revisions to data input procedures in an attempt to simplify the entry of meteorological, optical and target parameters into the computer program. Detailed step by step instructions for the input/output data files are included in the set of user instructions for FASCAT given in Appendix B. A brief discussion of some special input options is given in Section 3.3 including the use of LOWTRAN aerosol models (Shettle and Fenn, 1979) for the specification of optical property profiles.

Finally, in Section 3.4, calculations of visual detection range for simplified targets and backgrounds are used as a yardstick to explore the relative impact of natural variations in atmospheric and target factors on visible image transmission. The examples illustrate the variation in the target detection range as a function of changes in boundary layer extinction coefficient, cloud cover, solar zenith angle, type of aerosol, and target illumination.

3.1 Extension of the Radiance Model to Partly Cloudy Atmospheres

Explicit determination of the instantaneous upper and lower hemisphere radiance fields in a partly cloudy atmosphere requires a detailed knowledge of the actual cloud structure, orientation and illumination that is normally not available. Even if precise determinations were possible, the resultant calculations may be representative for only short time periods. However, we can consider the development of computational schemes that provide estimates of the average (most probable) effects of changes in cloud cover on the apparent target and local background radiance fields. For partly cloudy atmospheres, the calculation of both the direct sun contribution to the irradiance incident on the target and the singly scattered sunlight component of the path radiance can be handled as before with the basic FASCAT model. Cloud-free path algorithms (Allen and Malick, 1983) define the approximate probability that the target, background or observation path will be in sunlight or cloud shadow. The important complicating factor is of course the determination of the diffuse components of the irradiance and radiance fields and their dependence on cloud type and amount. After consideration and rejection of many approaches, we settled on a highly simplified method which solves for the diffuse radiance field as the weighted average of clear-sky and overcast-sky diffuse field calculations. The analytical techniques as derived through reference to SOLMET (1977) data base help ensure that the results are consistent with the average observed surface irradiance as a function of cloud type and amount and solar zenith angle. The SOLMET data base and its application for the determination of the average optical thickness of overcast cloud layers for individual cloud types are described in Appendix A, Section 4. Reference is made also to the discussion of the development and testing of techniques for the determination of the radiance fields in overcast sky conditions given in Appendix A. Extension of the techniques for use in partly cloudy atmospheres is discussed in the following paragraphs.

The SOLMET data were utilized by Shapiro (1982) in a different way with other modeling procedures to determine the average flux transmittance and average albedo for individual layers of partial cloud cover for many cloud types as a function of cloud amount and solar zenith angle. With additional simplifying assumptions, the results of these studies can be applied in part for the calculation of the approximate average diffuse irradiance and radiance fields in partly cloudy atmospheres.

DETERMINATION OF UPWARD IRRADIANCE

The albedo at altitude z_a at the top of the cloud layer is given by

$$A(z_a) = E(z_a, u)/E(z_a, d) , \qquad (1).$$

where $E(z_a, u)$ and $E(z_a, d)$ are the upward and downward irradiance, respectively. Shapiro (1982) assumed that the albedo of the partly cloudy layer, A_{PC}, is given by the weighted average of the albedo for a corresponding clear atmosphere, A_{CR}, and the albedo for the overcast sky, A_{OV}, having the same cloud form, thus

$$A_{PC}(z_a) = F(n, \mu_s) A_{OV}(z_a) + [1 - F(n, \mu_s)] A_{CR}(z_a) . \qquad (2)$$

Selecting SOLMET data subsets with a single cloud type and amount present, Shapiro determined weighting factors which define average values of $F(n, \mu_s)$ as a function of cloud type, cloud fraction, n, and cosine of the solar zenith angle μ_s. The derived empirical values of $F(n, \mu_s)$ exhibit a systematic behavior, but depart significantly from a straight linear dependence on n. Shapiro derived bi-quadratic polynomial expressions which provide close approximations of the derived weighting factors as determined for the individual cloud types. With due consideration to the expected time and space variability of the albedo of partly cloudy layers and the lack of strong systematic variability in $F(n, \mu_s)$ as a function of cloud type, we combined solutions to obtain a general polynomial representation given by

$$F(n, \mu_s) = n(1.43 - 1.21\mu_s - 2.00n + 1.21 n \mu_s + 1.57 n^2) . \qquad (3)$$

It should be emphasized that while Eq. (3) as depicted in Fig. 3.1 applies to all cloud types, the albedo of the partly cloudy layer, as calculated from Eq. (2), is dependent upon the actual optical properties of the cloud used for the calculation of A_{OV}. (See Appendix A, Section 4). Note also that $F(n, \mu_s)$ is zero for clear sky and one for overcast cloud cover.

Since the total downward (solar plus diffuse) irradiance $E(z_a, d)$ incident on the top of a single cloud layer does not vary significantly with n, we can write approximately through combination of Eqs. (1), (2), and (3),

$$E_{PC}(z_a, u) = F(n, \mu_s) E_{OV}(z_a, u) + (1 - F(n, \mu_s)) E_{CR}(z_a, u) , \qquad (4)$$

where $E_{OV}(z_a, u)$ and $E_{CR}(z_a, u)$ are the upward diffuse irradiances as determined for overcast and clear sky respectively.

DETERMINATION OF THE DOWNWARD IRRADIANCE

A similar expression can be derived for the total downward irradiance below the cloud layer. The flux transmittance ${}_F T(l)$ of cloud layer l is given by

$${}_F T(l) = E(z_b, d)/E(z_a, d) \qquad (5)$$

where $E(z_b, d)$ is the downward irradiance at altitude z_b at the base of the cloud layer. Assuming $E_{PC}(z_a, d) = E_{OV}(z_a, d) = E_{CR}(z_a, d)$ we have,

$$E_{PC}(z_b, d) = F(n, \mu_s) E_{OV}(z_b, d) + [1 - F(n, \mu_s)] E_{CR}(z_b, d) . \qquad (6)$$

The total downward irradiance can be expressed as the sum of the diffuse, ${}_D E(z_b, d)$, and direct sun, ${}_s E(z_b, d)$, components hence,

$$E(z_b, d) = {}_D E(z_b, d) + {}_s E(z_b, d) . \qquad (7)$$

Let us assume that the average over time of the solar irradiance component in partly cloudy atmospheres is determined by the cloud-free solar path probability, $G(n, \mu_s)$, such that

$$
{}_s\bar{E}_{PC}(z_b, d) = G(n, \mu_s)\, {}_sE_{CR}(z_b, d) + [\, 1 - G(n, \mu_s)]\, {}_sE_{OV} \,. \tag{8}
$$

Substituting Eqs. (7) and (8) in Eq. (6) and assuming that the diffuse irradiance is represented by the time-averaged diffuse irradiance, we have for partly cloudy skies

$$
\begin{aligned}
{}_DE_{PC}(z_b, d) &= F(n, \mu_s)\, {}_DE_{OV}(z_b, d) \\
&+ [\, 1 - F(n, \mu_s)\,]\, {}_DE_{CR}(z_b, d) \\
&+ [\, 1 - F(n, \mu_s) - G(n, \mu_s)\,]\, [\, {}_sE_{CR}(z_b, d) - {}_sE_{OV}(z_b, d)\,] \,.
\end{aligned} \tag{9}
$$

In the special case where 1-F=G, the downward diffuse irradiance below the cloud layer is given by the weighted average of the diffuse irradiance calculated for the corresponding overcast and clear atmospheres as prescribed by Eq. (4) for the upward irradiance above the cloud layer. However, using the approximation of Allen and Malick (1983) for $G(n, \mu_s)$ and Eq. (3) for $F(n, \mu_s)$, we find that the quantity (1-F) is invariably larger than G in association with an additive component to the downwelling diffuse irradiance below the cloud layer. Likely sources of the enhancement of diffuse irradiance are the forward scatter of direct solar radiance through the thin cloud edges and the reflection downward from the sides of opaque clouds. The additive term increases with increasing solar elevation angle and increases as the cloud cover increases from scattered to broken. Illustrations of these effects through sample model calculations of diffuse radiance are given later in this section.

DETERMINATION OF THE AVERAGE PATH RADIANCE

Conceding for reasons discussed above that detailed calculations of the upper hemisphere radiance fields in partly cloudy atmospheres are not practicable, let us introduce assumptions that greatly simplify calculation of the average directional path radiance distribution that is expected to occur with a given cloud cover and aerosol distribution. A necessary step is to develop approximate expressions that specify the expected changes in the path function at all points in the atmosphere that are associated with changes in cloud amount as a function of cloud type and solar angle. The approach here is to establish general expressions for the path function that are consistent with the average behavior of the diffuse irradiance fields in partly cloudy conditions as represented by Eqs. (4) and (9).

For immediate reference, let us recall the basic expressions for path radiance and path function given in Appendix A, Section 2. The spectral path radiance is given by

$$
L_r^{*}(z, \theta, \phi) = \int_0^r L_{*}(z', \theta, \phi)\, T_r'(z', \theta)\, d_r' \tag{10}
$$

where $L_{*}(z', \theta, \phi)$ is the path function, defined as the point function component of the path radiance that is generated by the scattering of light reaching that point of the path from all directions. The path function can be expressed in terms of its contributions from the scattering of solar (lunar) scalar irradiance $L_{*s}(z, \theta, \phi)$ and from the scattering of sky, cloud and earth radiances $L_{*d}(z, \theta, \phi)$ thus

$$
L_{*}(z, \theta, \phi) = L_{*s}(z, \theta, \phi) + L_{*d}(z, \theta, \phi) \tag{11}
$$

where

$$
L_{*s}(z, \theta, \phi) = {}_s\epsilon(z)\, P(z, \beta)\, s(z) \tag{12}
$$

and

$$
L_{*d}(z, \theta, \phi) = \int_{4\pi} L(z, \theta', \phi')\, P(z, \beta)\, s(z)\, d\Omega' \,. \tag{13}
$$

$P(z, \beta)$ is the normalized single scattering phase function at angle β between the path of sight and the direction of the source light and $s(z)$ is the total volume scattering coefficient. As described in Section 2.1, Appendix A, the delta-Eddington approximation is employed to determine the multiple scattering component of the path function. The resultant expression for the path function (Eq. (17), App. A) can be written,

$$
\begin{aligned}
L_{*}(z, \theta, \phi) = s(z)\, [\, & P(z, \beta_s)\, {}_s\epsilon(z) \\
& + L_D(z) + g\, L_{D'}(z) \cos\theta + \\
& g\, L_{D''}(z) \cos\phi \,] \,,
\end{aligned} \tag{14}
$$

where g is the asymmetry factor, and L_D, $L_{D'}$ and $L_{D''}$ are the average, vertical asymmetry, and azimuthal asymmetry components respectively of the delta-Eddington path function representation.

Given approximate expressions for the calculation of the diffuse component of the path function, $L_{*d}(z, \theta, \phi)$ we can proceed with the FASCAT model to calculate the spectral path radiance distribution in partly cloudy atmospheres in the same way as for clear and overcast atmospheres. Let us specify that the diffuse component of the path function will respond to changes in cloud amount and solar zenith angle in direct correspondence with the changes in the diffuse irradiance above and below the cloud layer. Consistent with Eq. (4), we assume for all points above the cloud layer that

$$
{}_{PC}L_{*d}(z_a, \theta, \phi) = F(n, \mu_s)\, {}_{OV}L_{*d}(z_a, \theta, \phi) + [\, 1 - F(n, \mu_s)\,]\, {}_{CR}L_{*d}(z_a, \theta, \phi) \tag{15}
$$

and by analogy with Eq. (9), we assume for all points below the cloud layer that

$$
{}_{PC}L_{\bullet d}(z_b,\theta,\phi) = F(n,\mu_s)\,{}_{OV}L_{\bullet d}(z_b,\theta,\phi) + [\,1-F(n,\mu_s)\,]\,{}_{CR}L_{\bullet d}(z_b,\theta,\phi) + \frac{1}{\pi}\,[\,1-F(n,\mu_s)-G(n,\mu_s)\,]\,[\,{}_sE_{CR}(z_b,d)-{}_sE_{OV}(z_b,d)\,] \tag{16}
$$

where the weighting factors $F(n,\mu_s)$ are given by Eq. (3). The probability of a cloud free solar path, $G(n,\theta_s)$, can be expressed (Allen and Malick, 1983)

$$
\ln G(n,\theta_s) = (1+c_n\tan\theta_s)\ln p_n\,, \tag{17}
$$

where θ_s is the solar zenith angle

and

$$
p_n = 1-n(1+3n)/4 \tag{18}
$$

and

$$
c_n = 0.55-n/2\,. \tag{19}
$$

For completeness, we assume that Eq. (15) also applies at all points along segments of cloud-free viewing paths that are between the base and top of the partly cloudy layer.

Sample model calculations of the diffuse scalar irradiance as a function of cloud amount and solar angle for a point below an altocumulus cloud layer of average optical thickness are shown in Fig. 3.1. The values represent the calculated diffuse radiant flux arriving at the point from all directions about that point located at 3 km, with the base altitude of the cloud layer at 3.5 km. The values are normalized by dividing by the diffuse scalar irradiance as calculated for corresponding the clear-sky condition. They depict only the normalized diffuse scalar irradiance. If the point is in direct sunlight, the solar irradiance must be added to obtain the total scalar irradiance reaching that point. For solar zenith angles less than that about 65 degrees, the calculated average diffuse scalar irradiance tends to be larger for partly cloudy conditions than for either clear or overcast conditions. As illustrated in Fig. 3.1, the diffuse scalar irradiance increases with increasing cloud amount up to about 7/10 cloud cover and decreases thereafter as the shadowing effects of adjacent cloud elements become more prominent. Notice that the normalized diffuse irradiance increases markedly with increasing solar elevation angle.

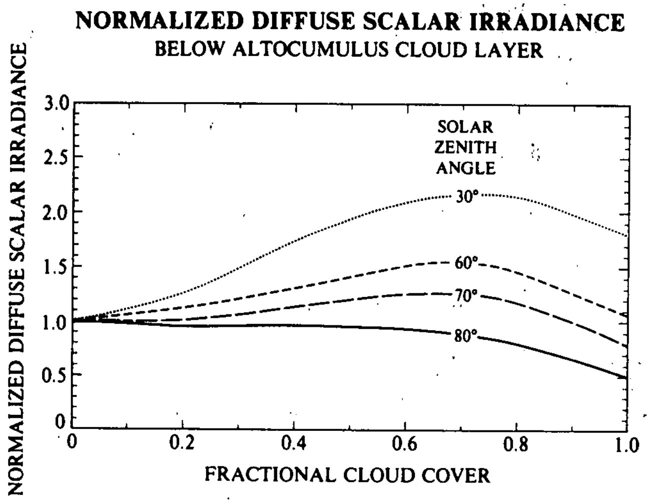

Fig. 3-1. Model calculations of the average diffuse radiant flux arriving at a point 0.5 km below the base of an altocumulus cloud layer as a function of cloud amount. The irradiance values are normalized by dividing by the diffuse scalar irradiance for the clear atmosphere with corresponding aerosol optical properties.

For calculations of the time or space averaged values of path function for points below the cloud layer with Eq. (11), the increase in the diffuse component with increasing cloud amount tends to be offset by a decrease in the direct solar component of the path function due to the increased probability that the points along the observation path will be in cloud shadow. The average or most probable value of the solar component of the path function for partly cloudy atmospheres is given by,

$$
{}_{PC}L_{\bullet s}(z,\theta,\phi) = G(n,\mu_s)\,{}_{CR}L_{\bullet s}(z,\theta,\phi) + [\,1-G(n,\mu_s)\,]\,{}_{OV}L_{\bullet s}(z,\theta,\phi)\,. \tag{20}
$$

TWO-LAYER CLOUD OPTION

The above system of analytic expressions yields estimates of the average path radiance distribution for atmospheres with a single cloud layer of varying cloud amount. A simple strategy was used to extend the FASCAT model calculations to include a second layer of fractional cloud cover, although the physical basis for the determination of the average diffuse spectral radiance is much more tenuous. The assumption is made that the weighting factors $F(n,\mu_s)$ as determined for a single cloud layer will apply in general to conditions where the layer exists in combination with a second layer of variable cloud cover. In the absence of representative experimental data for definitive tests of this assumption, the 2-layer cloud option is included in FASCAT only as a means to obtain rough estimates of the multi-layer cloud effects on image transmission. The diffuse path function component is calculated as the weighted average of the corresponding values as calculated for the overcast upper layer, U, the overcast lower layer, L, overcast both layers, UL, and for the clear atmosphere, CR. For the region above the base of the upper cloud layer, we assume

$$
\begin{aligned}
{}_{PC}L_{\bullet d}(z,\theta,\phi) = {} & [\,1-F_U(n_U,\mu_s)\,]\,[\,1-F_L(n_U,\mu_s\,]\,{}_{CR}L_{\bullet d}(z,\theta,\phi) \\
& + F_U(n_U,\mu_s)\,[\,1-F_L(n_L,\mu_s)\,]\,{}_{OV,U}L_{\bullet d}(z,\theta,\phi) \\
& + F_L(n_L,\mu_s)\,[\,1-F_U(n_U,\mu_s)\,]\,{}_{OV,L}L_{\bullet d}(z,\theta,\phi) \\
& + F_U(n_U,\mu_s)\,F_L(n_L,\mu_s)\,{}_{OV,UL}L_{\bullet d}(z,\theta,\phi)
\end{aligned} \tag{21}
$$

For the region below the base of the upper layer we assume

$$
\begin{aligned}
{}_{PC}L_{\bullet d}(z,\theta,\phi) = {} & [\,1-F_U(n_U,\mu_s)\,]\,[\,1-F_L(n_U,\mu_s\,]\;{}_{CR}L_{\bullet d}(z,\theta,\phi) \\
& + F_U(n_U,\mu_s)\,[\,1-F_L(n_L,\mu_s)\,]\;{}_{OV,U}L_{\bullet d}(z,\theta,\phi) \\
& + F_L(n_L,\mu_s)\,[\,1-F_U(n_U,\mu_s)\,]\;{}_{OV,L}L_{\bullet d}(z,\theta,\phi) \\
& + F_U(n_U,\mu_s)\,F_L(n_L,\mu_s)\;{}_{OV,UL}L_{\bullet d}(z,\theta,\phi) \\
& + \frac{{}_sE_{CR}(z,d)}{\pi}\left\{[\,1-F_U(n_U,\mu_s)\,]\,[\,1-F_L(n_L,\mu_s)\,]\right. \\
& \qquad \left. - G_U(n_U,\mu_s)\,G_L(n_L,\mu_s)\right\} \\
& + \frac{{}_sE_U(z,d)}{\pi}\left\{F_U(n_U,\mu_s)\,[\,1-F_L(n_L,\mu_s)\,]\right. \\
& \qquad \left. - G_L(n_L,\mu_s)\,[\,1-G_U(n_U,\mu_s)\,]\right\} \\
& + \frac{{}_sE_L(z,d)}{\pi}\left\{F_L(n_L,\mu_s)\,[\,1-F_U(n_U,\mu_s)\,]\right. \\
& \qquad \left. - G_U(n_U,\mu_s)\,[\,1-G_L(n_L,\mu_s)\,]\right\} \\
& + \frac{{}_sE_{UL}(z,d)}{\pi}\left\{F_U(n_U,\mu_s)\,F_L(n_L,\mu_s)\right. \\
& \qquad \left. - [\,1-G_U(n_U,\mu_s)\,]\,[\,1-G_L(n_L,\mu_s)\,]\right\}, \qquad (22)
\end{aligned}
$$

where the factors $F(n,\mu_s)$ and $G(n,\mu_s)$ are determined as before from Eqs. (3) and (17), respectively, except that $G_L(n_L,\mu_s) = 1$ above the base of the lower cloud layer. For optically thick clouds, ${}_sE_U$, ${}_sE_L$ and ${}_sE_{UL}$ tend to zero.

Diagnostic model calculations of visual detection range as a function of cloud amount are given in Section 3.3 below.

3.2 Calculation of Apparent Target and Background Radiances

The fundamental equation for the apparent spectral radiance of distant target t at range r, as given by Duntley, *et al.* (1957), [see Eq. (1) Appendix A] is

$$
\begin{aligned}
{}_tL_r(z,\theta,\phi) = {} & {}_tL_o(z_t,\theta,\phi)\;T_r(z,\theta) \\
& + L_r^*(z,\theta,\phi)\,, \qquad (23)
\end{aligned}
$$

where ${}_tL_o$ is the inherent target radiance at altitude z_t, and $T_r = \exp - \int_0^r \alpha(r)dr$ is the path transmittance and α is the volume attenuation coefficient. The apparent radiance of the target is the sum of the residual target radiance and the path radiance, which is given by Eq. (10). We note that the determination of the apparent target radiance requires resolution of 3 inter-related atmospheric effects: the influence of the irradiance distribution on the inherent target radiance, the attenuation of the target radiance, and the generation of the spurious path radiance.

For the specific purpose of calculating the inherent target radiance, it is assumed that both the downward and upward diffuse radiance fields are uniform. Now the diffuse component of the irradiance on the target surface can be expressed

$$
\begin{aligned}
{}_DH_t(z_t,\theta_{Nt}) = {} & {}_DE(z_t,d)\,[\,1+\cos\theta_{Nt}\,]/2 \\
& + {}_DE(z_t,u)\,[\,1-\cos\theta_{Nt}\,]/2 \qquad (24)
\end{aligned}
$$

where, as in Eq. (4) and Eq. (7), $E(z_t,u)$ is the upward irradiance on a horizontal surface, ${}_DE(z_t,d)$ is downward diffuse irradiance on a horizontal surface and the direction of the target surface normal is (θ_{Nt},ϕ_{Nt}). The total (solar plus diffuse) irradiance on the target surface is

$$
H_t(z_t,\theta_{st},\theta_{Nt}) = \epsilon_s(z_t)\cos\theta_{st} + {}_DH_t(z_t,\theta_{Nt})\,, \qquad (25)
$$

where the angle between the solar direction and the target surface normal direction is given by

$$
\begin{aligned}
\cos\theta_{st} = {} & \cos\theta_{Nt}\,\cos\theta_s \\
& + \sin\theta_{Nt}\,\sin\theta_s\,\cos(\phi_{Nt}-\phi_s)\,. \qquad (26)
\end{aligned}
$$

The $\cos\theta_{st}$ is set to zero if $\cos\theta_{st}<0$ or if the target is in local shadow. Finally, it is assumed that the target surfaces reflect in accordance with Lambert's law so that the expression for the inherent spectral radiance of the target becomes

$$
{}_tL_o(z_t,\theta,\phi) = R_tH_t(z_t,\theta_{st},\theta_{Nt})/\pi \qquad (27)
$$

The expressions corresponding to Eqs. (23), (24), (25), and (27) for the apparent spectral radiance of the local background are

$$
{}_bL_r(z,\theta,\phi) = {}_bL_o(z_b,\theta,\phi)\;T_r(z,\theta) + L_r^*(z,\theta,\phi)\,, \qquad (28)
$$

$$
\begin{aligned}
{}_DH_b(z_b,\theta,\phi) = {} & {}_DE(z_b,d)\,[\,1+\cos\theta_{Nb}\,]/2 \\
& + {}_DE(z_b,u)\,[\,1-\cos\theta_{Nb}\,]/2\,, \qquad (29)
\end{aligned}
$$

$$
H_b(z_b,\theta_{sb},\theta_{Nb}) = \epsilon_s(z_b)\cos\theta_{sb} + {}_DH_b(z_b,\theta_{Nb})\,, \qquad (30)
$$

and

$$
{}_bL_o(z_b,\theta,\phi) = R_bH_b(z_b,\theta_{sb},\theta_{Nb})/\pi\,, \qquad (31)
$$

where the subscript b refers to the local background surface which appears in immediate contrast with the designated target surface. As in the case of the target surface, the direction of the normal to the local background is an independent input variable to FASCAT. For objects viewed against a sky background, ${}_bL_o$ is zero. If one selects the sea surface option in FASCAT, R_b is ignored for observing paths directed toward the sea surface, and the inherent radiance is calculated as the Fresnel reflectance of the wind ruffled water surface assuming the wave slope probabilities of Cox and Munk (1954) (see Section 3, Appendix A).

3.3 FASCAT Application Methodology

In order to calculate the apparent spectral contrast of distant targets, one must know or estimate a variety of environmental and target factors. Needless to say, the accuracy and representativeness of data available for these determinations varies markedly depending upon the circumstances under which the model is applied. For this reason emphasis has been placed upon the development of data input procedures that help simplify the input of the required information and are adaptable to the amount and variety of available data. The FASCAT input file and an item by item set of user instruction notes are included as Appendix B of this report. Some recent changes in the input format and some special features of the modeling procedures are reviewed in the following paragraphs.

The basic method used for data entry has been modified to improve both the data handling and the computational efficiency of the model. Under the new format the data are input sequentially in four functional categories: *general parameters, optical property profiles, cloud layer information, and target and local background data.* Selected data entry items in each category will be discussed below to augment the user instructions given in Appendix B.

GENERAL PARAMETERS

Wavelength - Although the model calculations are strictly applicable only for monochromatic radiation, the results are suitable with good approximation for reasonably broad spectral bands in the visible and near infrared portions of the spectrum. The designated wavelength should be chosen to conform as closely as possible with the overall spectral characteristics of the sensor. The model is applicable over the range 450 to 1060 nm.

Average surface reflectance - The weighted spatial average of the surface reflectance is entered to calculate the component of the path radiance that is generated by light reaching the path through reflection by the underlying surface and subsequent scattering by the atmosphere in the direction of the sensor. Thus, the area comprising the spatial average may be small as in the case of slant observation paths near the earth's surface or large as for paths extending from high altitude to the horizon. As described under target data below, another data entry is made for the local background reflectance, which often differs from the average reflectance. The local reflectance is used for the determination of the inherent radiance of the immediate background against which the target appears.

Base altitude of the top layer - This input item sets the lower altitude limit of the primary ozone layer and should, in most instances, correspond with the altitude of the tropopause. Stored climatological values of total ozone as a function of latitude and season are used to calculate the ozone optical depth of the top layer for the designated wavelength. Desired departures from the climatological values can be handled through appropriate changes in the designated single scattering albedo for the top layer. The single scattering albedo for the top layer normally is used to define only the absorption by molecular or aerosol constituents other than ozone.

Observation angles - Up to 20 zenith observing angles may be selected. Default values include every ten degrees beginning at 5 and ending at 175 degrees plus zenith angles of 100 and 110 degrees. Three azimuthal observing angles may be selected. They are specified in items 21 and 22 of the input file as departures from the solar azimuthal angle. The default values are 0 (upsun), 180 (downsun) and 90 (cross sun) degrees.

OPTICAL PARAMETER PROFILES

Under the revised data entry format, the optical property profiles for the cloud-free atmosphere, above, below, and between cloud elements, are established first. Next the cloud properties are superimposed and finally information with respect to sensor, target and background factors are entered.

Optical Properties - Depending upon the completeness of available measurements and observations, one may select up to 10 layers to define the vertical distribution of the individual parameters. For each designated layer, the optical scattering ratio, the single scattering albedo, and the single scattering phase function and the associated asymmetry factor must be entered. Reference is made to Sections 3.2 and 3.3 of Appendix A for a discussion of these optical parameters and for a description of options for their specification and entry into the computer program.

A recent extension to the FASCAT computer code, developed by Lt.Col. John D. Mill and Eric.P. Shettle of the Air Force Geophysics Laboratory, enables specification of the optical properties for each layer through use of the LOWTRAN aerosol models (Shettle and Fenn, 1979). Representative optical properties for rural, maritime, urban and tropospheric atmospheres as well as for advection and radiation fog are supplied through interpolation from stored look-up tables. The aerosol model and associated properties are designated independently for each layer. The operator enters the appropriate aerosol type, the visible (550 nm) extinction coefficient and the relative humidity, and the corresponding values of optical scattering ratio, single scattering albedo and the phase function for the designated wavelength are determined and supplied to the main program for radiance field calculations.

As discussed in Section 3.3, Appendix A, many options are available in particular for the specification of the single scattering phase function. For example, the program will accept the coefficients of two-term Henyey-Greenstein functions and calculate the scattering phase function. When other information is lacking, another model option will estimate the Henyey-Greenstein coefficients from the scattering ratio using algorithms derived from the extensive field measurements of phase function by Barteneva (1960).

It should be emphasized that profile information for all atmospheric levels must be entered before specific cloud type and amount information is entered below. For layers of fractional cloud cover, the data entries in all cases define the optical properties of the cloud-free paths between the individual clouds. For overcast cloud layers, the operator has two choices. First he can simply make dummy entries for the optical properties for the overcast cloud layer for the initial profiles that will be ignored and new data will be supplied through entry of cloud information in the input file items discussed below. The second option for overcast layers can be used if the operator desires to enter his own cloud optical properties (scattering ratio, single scattering albedo, and scattering phase function) rather than rely on the average values prescribed as a function of cloud type. If the second option is chosen for overcast cloud representation, the cloud optical properties are entered along with and in the same manner as for the cloud-free layers, and no entry for the cloud layer is made in the cloud layer input file below.

CLOUD LAYER INFORMATION

The input for the individual cloud layers (2-layer maximum) consists of the base and top altitudes, the cloud amount in tenths, the cloud type (cirrus/cirrostratus, altostratus/altocumulus, cumulus, stratus/stratocumulus, or nimbostratus/precipitation) and the relative optical depth of the cloud. The relative optical depth has 3 options: average, thin (minus standard deviation), and thick (plus standard deviation). In a separate phase of study summarized in Section 4.1, and Table 3 of Appendix A, the average and the variability of cloud optical depth as a function of cloud type were determined empirically from the SOLMET data base. The model algorithms return the optical depth for the specified cloud type and relative optical thickness (average, thick or thin) from the table without direct reference to the specified base and top altitude of the layer. In other words, the optical thickness is determined independently of the specified geometric thickness of the cloud.

TARGET AND LOCAL BACKGROUND DATA

Data sets consisting of sensor, target, and local background information, are entered in the last section of the input file. Once the path function and beam transmittance distributions have been established from prior entry data, the model deals in turn with each of the target/background data sets without need for repeating the basic path function and transmittance calculations. Data entry for all cases where the targets are viewed from above against the earth's surface as the background are listed first, followed by cases where the objects are viewed from below against a sky or cloud background. The number of target/background data entries is unlimited. The input data for each set includes:

DOWNWARD LOOKING OBSERVATION PATHS

Sensor altitude (km msl)

Target altitude (km msl)

Target reflectivity

Target normal zenith angle (deg.)

Target normal azimuthal angle (deg. departure from solar azimuth)

Target illumination (3 options)
(1) full sunlight
(2) cloud shadow - includes direct solar beam and forward peak radiance penetration of thin clouds
(3) local shadow

Local background (against which target appears) reflectivity

Local background surface normal zenith angle (deg)

Local background surface normal azimuthal angle (departure from solar azimuth angle)

Local background illumination (3 options)
(1) full sunlight
(2) cloud shadow
(3) local shadow

UPWARD LOOKING OBSERVATION PATHS

Data entry items for upward paths are the same as for downward paths of sight except that local background input data are not required. The apparent local background radiance for a clear or partly cloudy atmosphere is the calculated sky radiance for a cloud-free path. For the case of an intervening overcast layer, apparent radiance of the cloud is returned as the local background radiance. A separate data set is employed to calculate the apparent radiance of the local background where that background is an opaque cloud element in a partly cloudy sky. For the second data set, the cloud element is assumed to be the target for the upward path of sight, and the appropriate cloud reflectivity, cloud surface normal direction, and cloud illumination (full sun or shadow) are entered as target data.

It should be noted that for both upward and downward looking paths, the choice as to what is the target and what is the local background against which the target appears can be arbitrary in many situations. Model calculations of the apparent radiance of opaque surfaces are the same regardless of the target/background assignment.

3.4 Sensitivity Analysis

Special attention has been given to diagnostic studies of the effects of uncertainties in the input data on the model calculations of image transmission properties. The results of a broad series of trial sensitivity calculations are summarized in Section G of Appendix A. Visual detection range was used as the yardstick to analyze the relative importance of the changes in each of many environmental and target factors on the detection of distant objects.

In this section we will extend the analysis to include targets in shadow as well as in sunlight and to include targets and local backgrounds with non-horizontal surfaces. The following calculations are based on the same average reference atmosphere (Ref. A) with the exception that the height of the boundary layer extends to 1.3 km rather than 1 km. As before, a uniform target, 30 m in diameter, is assumed, which is viewed from aloft against an uncluttered surface background. The analytic representation of contrast threshold for visual detection is described in Section 6.2 of Appendix A. It is based upon the data of Taylor (1964) and corresponds to a 99 percent detection probability for a glimpse time of 1/3 sec and a lack of knowledge of the target position of ± 4 deg or more. The reflectivity of the target is .15 and the background reflectivity is .075. In all cases the target is at sea level and the sensor altitude is 3 km. Unless specified otherwise, the wavelength is 550 nm and the solar zenith angle is 60 deg.

The results of the supplementary model calculations are shown in Figs. 3.2 to 3.5. The cartoon inserts in each figure depict specific conditions with respect to the observing path and the target orientation and illumination. In most examples, the departure of the observation azimuthal angle from the solar azimuthal direction is 180 deg. (downsun). The target surface for these examples is either horizontal or vertical and the target and local background may be in direct sunlight, in local shadow, or in cloud shadow. For the sensitivity calculations, all input variables other than the factor under examination, are held constant and equal to the reference values listed above.

VARIATION WITH EQUIVALENT SURFACE VISIBILITY

Fig. 3.2 shows the variation in horizontal detection distance as measured along the ground surface as a function of the scattering ratio in the boundary layer. The equivalent surface visibility is approximated through Kochmieder's law under the assumption of complete aerosol particle mixing within the boundary layer and an assumed threshold contrast of 5 percent. Calculations are shown for boundary layer scattering ratios of 52, 26, 13, and 7.5 which correspond to equivalent surface visibilities of 5, 10, 20 and 40 km, respectively.

The first two data sets, (a) and (b), assume that the target and local background scene are in direct sunlight. The detection distances are somewhat larger for the vertical target surface in set (b) because of the enhanced solar irradiance of the vertical surface (solar zenith angle of 60 deg.) yields a larger inherent contrast with the local background.

Notice the substantial reductions in detection distance for all values of surface visibility for data set (c) (scene in local shadow) and data set (d) (altocumulus overcast) as compared with the sunlit conditions of sets (a) and (b). The visual detection distances are a minimum for the scene in local shadow (set c) where the inherent target/background signal is small in the shadowed area and the path radiance remains relatively high for the sunlit viewing path. The detection distances are larger for the intervening overcast condition (set d) as compared with the clear-sky, local-shadow case (set c) for two reasons. First, the downwelling diffuse irradiance on target and background is larger for the overcast sky condition, and second, the deleterious effects of path radiance are reduced in the absence of the direct sun component of scattering along the observing path under the overcast. The latter effect is offset a bit by the increase in diffuse irradiance of the path.

VARIATIONS WITH SOLAR ANGLE

Shown in Fig. 3.3 are examples of the changes in the detection distances of sunlit targets as a function of changes in solar zenith angle. The model calculations cover the range of solar angle corresponding to a time span from early morning to noon in middle latitudes in the spring or fall season. Data sets (a) and (b) are for a horizontal and vertical target surface, respectively, as viewed against a horizontal local background. Notice that the detection distances are much lower for the low solar elevation angles in data set (c), where the local background is inclined 30 degrees toward the sun. Since the reflectivity of the local background for all model calculations is assumed to be about one-half of the target reflectivity, the prescribed change in the slope and orientation of the local background in set (c) serves to reduce the inherent target/background contrast, particularly at high solar zenith angles.

VARIATIONS WITH CLOUD COVER

As emphasized in Section 3.1, the model calculations deal only with the average dependence of the apparent radiance distribution on cloud amount in partly cloudy atmospheres. Variations in detection distance with changes in cloud cover from clear, to scattered, to broken, to overcast sky conditions are shown in Fig. 3.4 for three target/background scenes. Data set (a) for a horizontal target surface in sunlight and set (b) for a vertical target surface in sunlight respond in a similar way to changes in cloud amount. The calculated detection distances remain essentially the same in each of these cases for sunlit target scenes with clear, 0.5, and 0.8 cloud cover. The lack of sensitivity of average detection distance to changes in cloud amount is the result of compensation in the atmospheric effects. The increase in the diffuse atmospheric irradiance with increasing cloud cover for the sunlit target produces an increase in the inherent target contrast signal but also serves to increase the troublesome path radiance. On the other hand, as the cloud amount increases the probability that points along the viewing path beneath the cloud layer will be in sunlight decreases and consequently the average observed path radiance is diminished. Fluctuations in cloud amount also affect the spatial average of the downwelling irradiance at the surface and in turn affect the surface reflected component of irradiance reaching the target surface, the local background surface, and the observation path below the cloud layer. The results for the particular reference conditions used for the model calculations in Fig. 3.4 show a modest systematic increase in

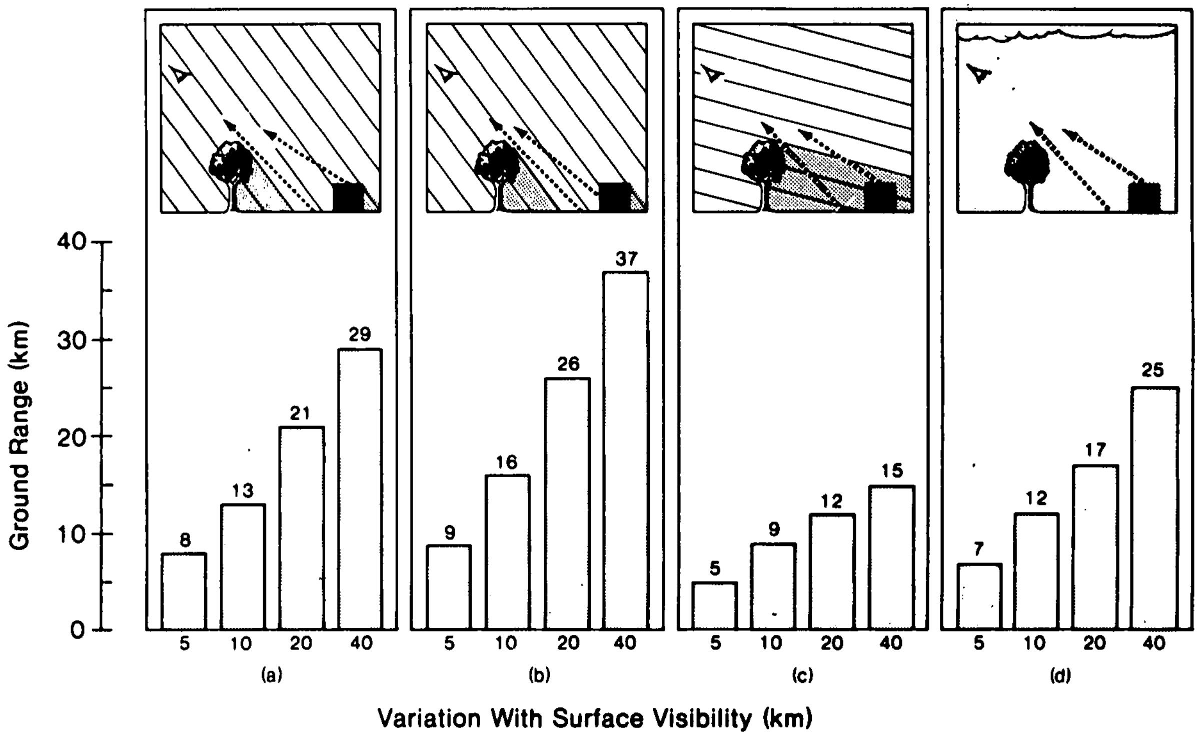

Fig. 3-2. Model calculations of visual detection distance as a function of the optical depth of the boundary layer (expressed as equivalent surface visibility). Ground based target at sea level is viewed downsun ($\phi = 180 degrees$) from 3 km altitude. Scene (a) - horizontal target surface in sunlight. Scene (b) - vertical target surface in sunlight. Scene (c) - horizontal target surface in local shadow. Scene (d) - horizontal target surface under altocumulus overcast with base altitude of 3.5 km.

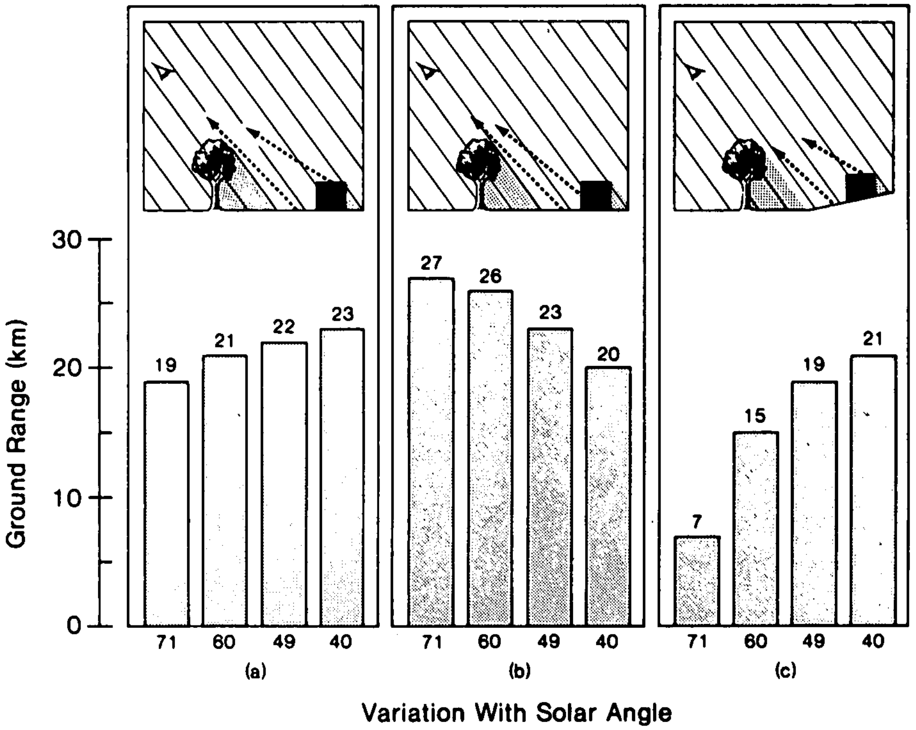

Fig. 3-3. Visual detection distance *vs* solar zenith angle (deg). Target at sea level is viewed downsun ($\phi = 180°$) from an altitude of 3 km. Scene (a) - horizontal target surface in sunlight. Scene (b) - vertical target surface in sunlight. Scene (c) - same as (a) except the local background surface is inclined 30° toward the solar direction.

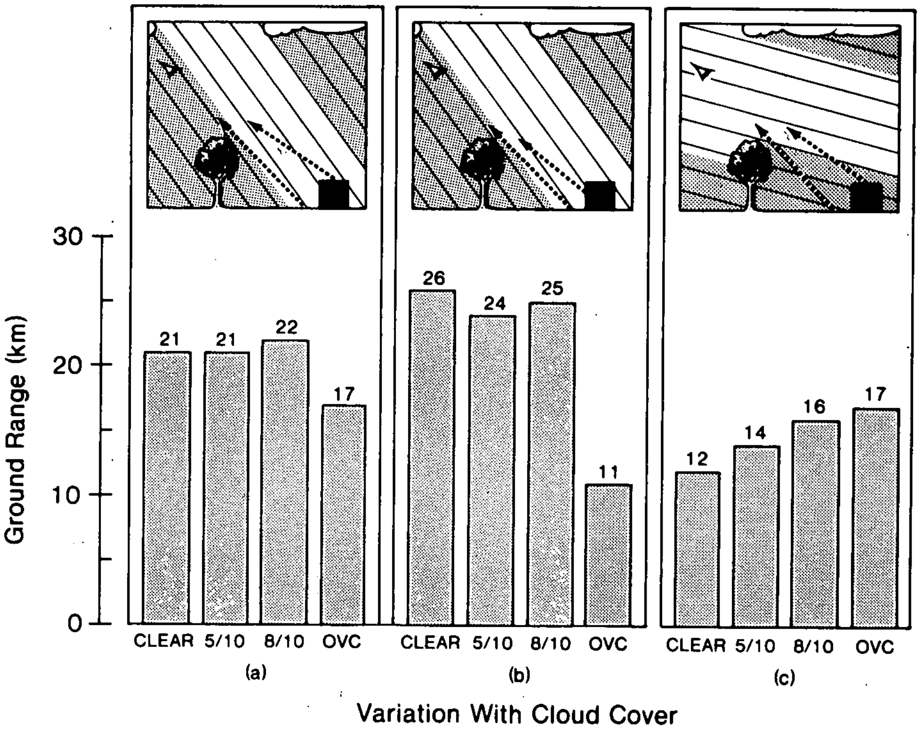

Fig. 3-4. Visual detection distance *vs* fractional amount of altocumulus cloud with base altitude of 3.5 km. Sea level target is viewed downsun from an altitude of 3 km. Scene (a) - horizontal target surface in sunlight. Scene (b) - vertical target surface in sunlight. Scene (c) - horizontal target surface in local shadow.

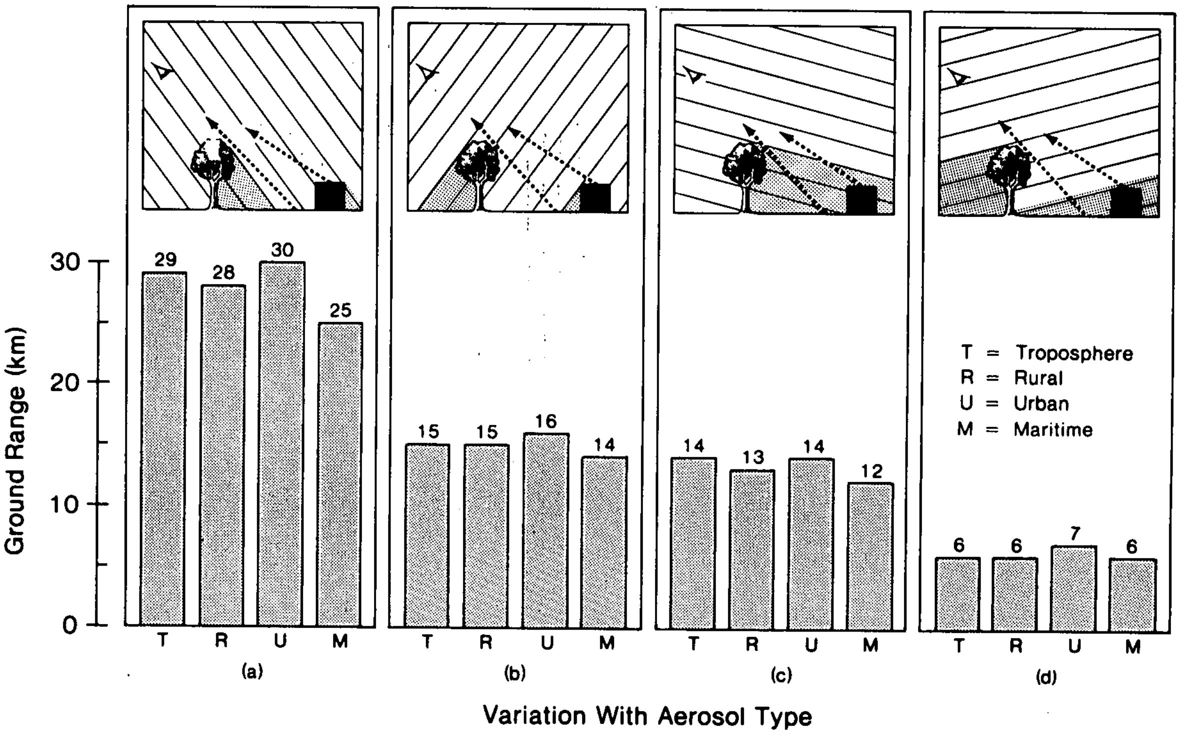

Fig. 3-5. Target detection distance *vs* LOWTRAN aerosol model type for the boundary layer. Ground based target at sea level is viewed from 3 km altitude. Scene (a) - horizontal target surface in sunlight is viewed in the downsun ($\phi = 180°$) azimuthal direction. Scene (b) - horizontal target surface in sunlight is viewed in the upsun ($\phi = 0°$) direction. Scene (c) - horizontal target surface in local shadow is viewed in the downsun direction. Scene (d) - horizontal target surface in local shadow is viewed in the upsun direction.

the average estimated detection distance with increasing cloud amount for target scenes in local shadow; and as stated above there is small net sensitivity to cloud amount changes in the range from zero to 0.8 fractional cloud cover for sunlit surface targets.

VARIATION WITH AEROSOL TYPE

The dependency of visual detection distance on the specific optical properties associated with individual LOWTRAN aerosol models is illustrated in Fig. 3.5. The model calculations were made for a wavelength of 670 nm. For each of the 4 target scenes, calculations were carried out assuming, in turn, that the aerosol characteristics of the boundary layer were given by the troposphere, rural, urban, and maritime aerosol models. All other factors, including the total volume extinction coefficient (550 nm) in the boundary layer, were held constant and equal to the average reference atmosphere values. A 70 percent relative humidity was assumed for all cases.

For the prescribed typical hazy atmosphere, it is evident that the net effect of the differences in aerosol model properties on the calculated detection distance at 670 nm is small for each of the target scenes. The detection distance is systematically above average for the urban model and below average for the maritime model atmosphere. This reflects the differences in single scattering albedo which result in a higher (lower) path radiance for the maritime (urban) atmosphere under the assumption of a constant total volume extinction coefficient in the boundary layer.

Substantial differences are noted in Fig. 3.4 between the model calculations for the various target scenes. For example, the visual detection distance is larger by a factor of 4.5 for case (a) where a sunlit target is viewed downsun as compared with case (d) where the target is in local shadow and is viewed along a sunlit path in the upsun direction. The detection distances as calculated for the sunlit target viewed directly upsun (data set b) and the shadowed target viewed downsun (data set c) are about the same.

3.5 REFERENCES (FOR SEC.3)

Allen, J.H. and J.D. Malick (1983), "The Frequency of Cloud-Free Viewing Intervals," *AIAA 21st Aerospace Sciences Meeting Paper*, **AIAA-83-0441**, 5, Reno, Nevada.

Barteneva, O.D. (1960), "Scattering Functions of Light in the Atmospheric Boundary Layer," *Bull.Acad.Sci. U.S.S.R., Geophysics Series*, pp. 1237-1244.

Cox, C. and W. Munk (1954), "Measurements of the Roughness of the Sea Surface from Photographs of the Sun's Glitter," *J. Opt. Soc. Am.*, **44**, pp. 838-850.

Duntley, S.Q., A.R. Boileau, and R.W. Preisendorfer (1957), "Image Transmission by the Troposphere. I," *J. Opt. Soc. Am.*, **47**, pp. 499-506.

Hering, W.S. (1981), "An Operational Technique For Estimating Visible Spectrum Contrast Transmittance," SIO Ref. 82-1, AFGL-TR-81-0198, ADA 111 823, University of California, San Diego, Scripps Institution of Oceanography, Visibility Laboratory.

Hering, W.S. (1983), "Analytic Techniques for Estimating Visible Image Transmission Properties of the Atmosphere," SIO Ref. 84-6, AFGL-TR-83-0236, University of California, San Diego, Scripps Institution of Oceanography, Visibility Laboratory.

Shapiro, R. (1982), "Solar Radiative Flux Calculations from Standard Surface Meteorological Observations," Sci. Report No. 1, AFGL-TR-82-0039, ADA 085 951, pp. 1-53, Systems and Applied Sciences Corporation.

Shettle, E.P. and R.W. Fenn (1979), "Models for the Aerosols of the Lower Atmosphere and the Effects of Humidity Variations on Their Optical Properties," AFGL-TR-79-0214, ADA 085 951.

SOLMET, (1977), *Hourly Solar Radiation-Surface Meteorolgical Observations, Vol. 1-Users Manual (1977), Vol. 2-Final Report (1979),* National Climatic Center, NOAA, EDIS, TD-9724 (1979).

Taylor, J.H. (1964), "The Use of Visual Performance Data in Visibility Prediction," *Appl. Opt.*, **3**, pp. 562-569.

4.0 SUMMARY

This Final Report under Contract No. F19628-82-C-0060 summarizes the results of several research studies directed toward the development of models of the optical properties of the atmosphere which are suitable for the operational support of tactical weapons and sensors operating in the visible and infrared portions of the electromagnetic spectrum.

The overall contractual effort has been an integral part of the overall Air Force Geophysics Laboratory (AFGL/AFSC) program to develop a thorough understanding of atmospheric effects on visible and infrared radiation through the atmosphere, and ultimately, the concomitant limitations on the performance of electro-optical systems such as target acquisition devices and precision guided munitions.

This Final Report contains a brief review of four previously issued interim reports which were submitted during this contractual interval in support of the primary model development task. It also contains the complete documentation for the FASCAT code and a discussion of the FASCAT model performance under fractional cloud meteorological conditions.

APPENDIX A

AFGL-TR-83-0236 **SIO Ref. 84-6**

ANALYTIC TECHNIQUES FOR ESTIMATING VISIBLE IMAGE TRANSMISSION PROPERTIES OF THE ATMOSPHERE

Wayne S. Hering

Visibility Laboratory
University of California, San Diego
Scripps Institution of Oceanography
La Jolla, California 92093

Approved:

R W Austin

Roswell W. Austin, Director
Visibility Laboratory

Approved:

William A. Nierenberg

William A. Nierenberg, Director
Scripps Institution of Oceanography

CONTRACT NO. F19628-82-C-0060
Project No. 7670
Task No. 7670-14
Work Unit No. 7670-14-02

Scientific Report No. 3
August 1983

Contract Monitor
Lt. Col. John D. Mill, Atmospheric Optics Branch, Optical Physics Division

Approved for public release; distribution unlimited.

Prepared for

AIR FORCE GEOPHYSICS LABORATORY
AIR FORCE SYSTEMS COMMAND
UNITED STATES AIR FORCE
HANSCOM AFB, MASSACHUSETTS 01731

SUMMARY

The development of field oriented techniques for determining the atmospheric effects on visible image transmission are described in this report. Simplified analytic methods are presented for calculating the background sky, cloud and terrain radiance distribution, and in turn the spectral contrast transmittance, of inclined paths of sight in the atmosphere. The directional path radiance is determined as the sum of the singly scattered sunlight component and a multiply scattered diffuse component that is calculated through application of the delta-Eddington approximation. Performance tests of the model radiance calculations were carried out through comparisons with results from more comprehensive radiative transfer models and by direct comparisons with high-resolution scanning radiometer measurements gathered by instrumented aircraft in a broad range of environmental conditions. Techniques for the representation of the optical parameters required as model input data are presented and discussed, including the specification of cloud optical depth as a function of cloud type.

An added feature of the contrast transmittance modeling system deals with the combined influences of atmospheric and target factors in order to calculate visual detection range for objects located at the surface and viewed from aloft. Analytic representations of vision experiment data are added along with target information to explore the relative sensitivity of detection range to selected changes in target and atmospheric parameters. Results are presented for several examples assuming simplified targets and backgrounds.

TABLE OF CONTENTS

LIST OF TABLES AND ILLUSTRATIONS

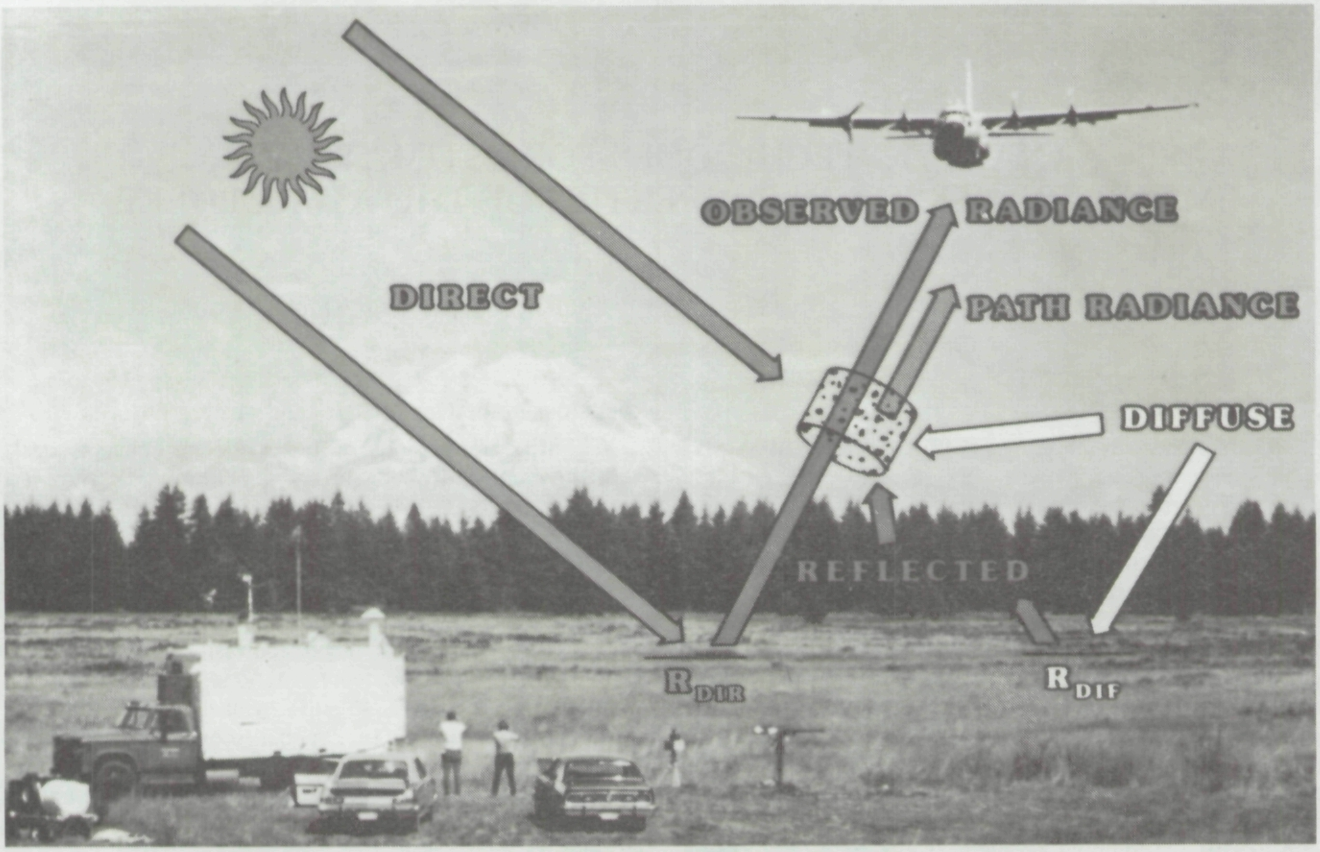

Frontispiece

The analytic techniques described in this report are a natural extension to a broad program of research into the optical properties of the atmosphere carried out by the Visibility Laboratory, University of California, San Diego, in cooperation with and under the sponsorship of the Air Force Geophysics Laboratory. The composite photograph shown above, illustrates some elements of the field program and some of the important components of the radiance field as measured by the instrumented aircraft. The field site near Mt. Rainier, Washington, is one of many locations in the United States and Europe where simultaneous measurements of optical and meteorological variables were gathered. Extensive high resolution measurements of the upper and lower hemisphere spectral radiance fields for scenes such as those illustrated by the fisheye camera photographs shown below (flight C-359) were of prime importance both for algorithm development and for validation of the modeling techniques over a wide range of environmental conditions.

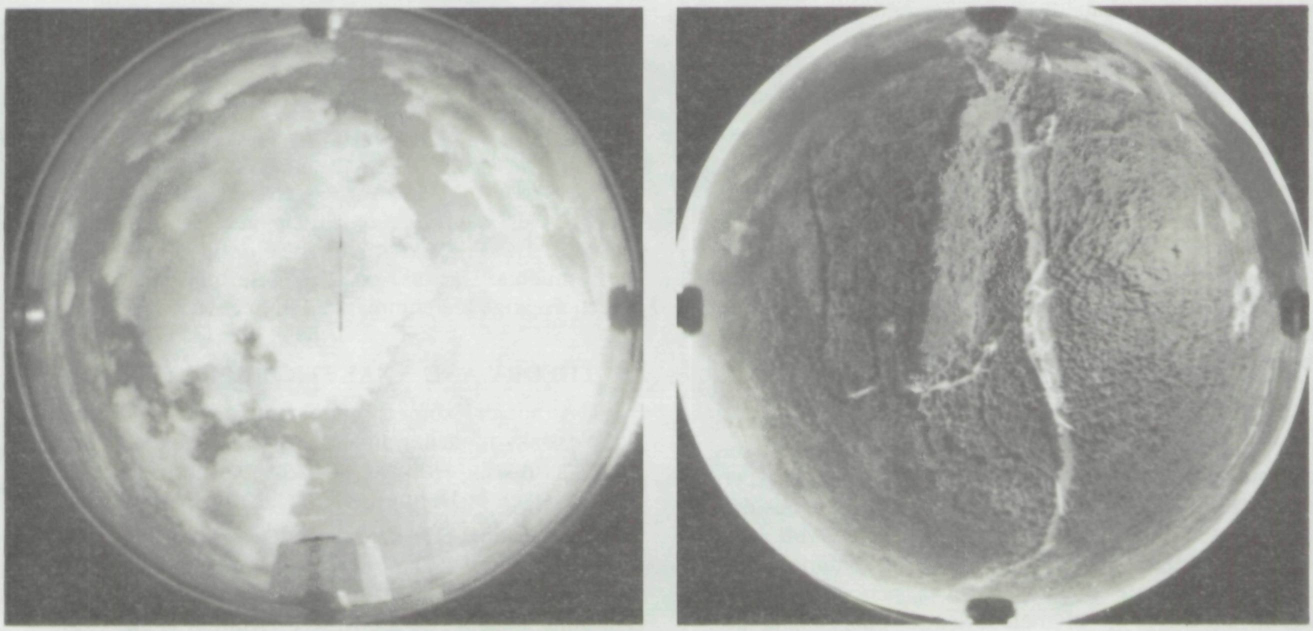

ANALYTIC TECHNIQUES FOR ESTIMATING IMAGE TRANSMISSION PROPERTIES OF THE ATMOSPHERE

Wayne S. Hering

1.0 INTRODUCTION

As set forth by Duntley (1948), the degradation of visible image contrast along a viewing path of increasing length is governed by (1) the attenuation of the inherent background and object radiances by air molecule and aerosol particle scattering and absorption, and (2) the generation of path radiance by molecular and aerosol scattering of incident light into the path of sight. Direct field measurements of the basic optical properties required for the determination of these factors for selected path segments cannot be made simply and inexpensively. Thus, operational estimates of contrast transmittance must be derived from model simulations that relate the aerosol directional scattering and absorption properties to generally available meteorological observations and forecasts (*e.g.* Shettle and Fenn, 1979). Additional problems stem from the complexity of multiple scattering processes and the relatively large amount of computer time and capacity required for treating the radiative transfer calculations completely as a physical problem. Effective simplifications must be made to yield fast yet consistent calculations of the radiance distribution. The successful development of techniques for real time estimates of the atmospheric effects on visible image transmission requires a reasonable balance between the desired accuracy, the complexity of the modeling procedures, and the reliability and representativeness of the available input data. Since these factors may vary considerably from one application to the next, it is important to retain reasonably good flexibility and completeness in the analytic approximations used for the estimates.

The development and testing of field oriented techniques for calculating directional path radiance and the object-background contrast transmittance along inclined paths of sight in clear-hazy atmospheres were described in a previous report (Hering, 1981). This paper addresses extensions and refinements to the modeling procedures and their validation. In particular, techniques are presented for (1) estimating the background radiance and visible image transmission characteristics in overcast sky conditions from conventional observations or forecasts of cloud type and altitude. As in the case of prior studies, technique development was based extensively on experimental data, including a broad series of simultaneous optical and meteorological measurements gathered with a specially instrumented aircraft. The high resolution profile measurements were obtained over a period of several years in a wide range of meteorological and geographical conditions in the United States and western Europe.

Further extensions of the modeling concepts deal with the combined effects of both environmental and target factors on visual detection range. Although independent assessment can be made of the changes in contrast transmittance that are associated with natural changes in the relevant atmospheric variables, the impact of these changes on target detection distance depends markedly on such factors as inherent target contrast, target size, and glimpse time. Analytic representations of vision experiment data (Blackwell, 1946 and Taylor, 1964) were added to the contrast transmittance model to explore the relative sensitivity of visual detection distance to a selected range of target and atmospheric variables. Results are presented for several examples assuming simplified targets and backgrounds.

A review of the basic equations and a summary of the analytic approximations used for calculating path radiance and for estimating visible spectrum contrast transmittance in cloudless atmospheres are given in Section 2. Also presented in Section 2, are comparative radiative transfer calculations between the simplified model and more complete computational methods. In Section 3, techniques are presented for the representation of the input variables that are required for the calculation of background radiance and spectral contrast transmittance. Extension of the modeling concepts to deal with image transmission characteristics for viewing paths below an overcast cloud layer are described in Section 4. Results of validation tests comparing model calculations with experimental measurements of the directional radiance distribution gathered by instrumented aircraft are given in Section 5. The results of sensitivity analyses which give a measure of the relative importance of individual target and environmental factors on the determination of target detection range are summarized in Section 6.

2.0 THEORY AND ANALYTIC APPROXIMATIONS

Although some refinements and additions to cloudless-sky modeling procedures are presented, this section is primarily a review of theory and analytic approximations given in Hering (1981).

Neglecting turbulence effects, the equation for the apparent spectral radiance of the background b at range r along the path of sight specified by zenith angle θ and azimuthal angle ϕ, can be written (Duntley *et al.* 1957)

$${}_bL_r(z,\theta,\phi) = T_r(z,\theta)\,{}_bL_o(z_t,\theta,\phi) + L_r^*(z,\theta,\phi)\,, \qquad (1)$$

where ${}_bL_o$ is the inherent background radiance at target altitude z_t,

$$T_r = \exp - \int_0^r \alpha(r)dr$$

is the path transmittance, α is the volume attenuation coefficient, and L_r^* is the path radiance produced by the scattering of light from the sun and from the surrounding sky, clouds and terrain into the path of sight.

The path radiance is given by

$$L_r^*(z,\theta,\phi) = \int_0^r L_*(z',\theta,\phi)T_r(z',\theta)dr'\,, \qquad (2)$$

where $L_*(z',\theta,\phi)$ is the path function, defined as the point function component of path radiance generated by the directional scattering of light reaching that point of the path. The expression for the path function can be written in terms of its contributions from the scattering of solar (lunar) scalar irradiance ${}_s\epsilon(z)$ and from the scattering of sky and earth radiances $L(z,\theta',\phi')$ as follows (*e.g.* Gordon, 1969b):

$$L_*(z,\theta,\phi) = {}_s\epsilon(z)\sigma(z,\beta_s) + \int_{4\pi} L(z,\theta',\phi')\sigma(z,\beta')d\Omega'\,, \quad (3)$$

where $\sigma(z,\beta)$ is the directional volume scattering function at angle β between the path of sight and direction of the source light, $d\Omega$ is an element of solid angle, and β_s is the scattering angle with respect to the sun.

In turn, the spectral contrast transmittance of the path of sight can be expressed (see Duntley *et al.* 1957) directly as the product of the path transmittance, $T_r(z,\theta)$, and the ratio of the inherent, ${}_bL_o$, and apparent, ${}_bL_r$, background radiances as follows:

$$C_r(z,\theta,\phi)/\,C_o(z_t,\theta,\phi) = T_r(z,\theta){}_bL_o(z_t,\theta,\phi)/\,{}_bL_r(z,\theta,\phi) \quad (4)$$

where $C_r = ({}_tL_r - {}_bL_r)/{}_bL_r$ is the apparent target contrast at path length r, $C_o = ({}_tL_o - {}_bL_o)/{}_bL_o$ is the inherent target contrast at altitude z_t and ${}_tL_o$ is the inherent target radiance. Thus, the contrast transmittance of a given path does not depend upon intrinsic target characteristics but is a function only of the directional radiance distribution in the atmosphere and the path transmittance. The expression is strictly applicable only for monochromatic radiation but may be applied with good approximation to reasonably broad spectral bands in the visible portion of the spectrum.

From Eq. (3) we note that the path function and in turn the contrast transmittance as calculated from Eq. (4) depend upon the direction of the viewing path relative to the distribution of light reaching the path. The first term on the right hand side of Eq. (3) is the contribution of primary scattering of direct solar irradiance. The directional volume scattering function may be expressed

$$\sigma(z,\beta) = P(z,\beta)s(z)\,, \qquad (5)$$

where $s(z)$ is the total volume scattering coefficient, and $P(z,\beta)$ is the single scattering phase function for combined Rayleigh plus aerosol particle scattering (see discussion in Section 3.3), which defines the probability that incident radiation will be scattered in the direction given by scattering angle β. The phase function varies significantly with the scattering properties of the aerosol particle distribution in the atmosphere.

Substituting Eq. (5) in Eq. (3), the expression for $L_*(z,\theta,\phi)$ becomes

$$L_*(z,\theta,\phi) = {}_s\epsilon(z)P(z,\beta)s(z)$$
$$+ \iint_{4\pi} L(z,\theta',\phi')P(z,\beta)s(z)d\Omega'\,. \qquad (6)$$

Modelling techniques for the calculation of the diffuse component of the path function are discussed in the following paragraphs.

2.1 Calculation of the Path Function

The second term on the right hand side of Eq. (6) is the component of the path function resulting from the scattering of diffuse radiance reaching the path from the surrounding sky and terrain. It has a directional dependence due to the asymmetry in the background sky and earth radiance distribution and the scattering phase function asymmetry. Precise numerical calculation of the path radiance resulting from the complex multiple scattering processes requires large amounts of computer time. For this reason, rapid approximate methods are employed extensively for radiation transfer calculations. The appropriate choice of computational method from among the variety of available methods depends upon the results desired for the application at hand.

While it is important to retain complete directionality for calculation of the path radiance component due to single scattering of direct solar radiance, approximate hemispherical two stream methods can be used effectively for fast calculation of the path radiance component due to scattering of the background sky and terrain radiances at any point and direction provided that the asymmetric influence of the prominent forward scatter peak and the irradiance profile are managed adequately. The delta-Eddington approximation introduced by Joseph, Wiscombe and Weinman (1976) satisfies the requirement. It extends the standard Eddington approximation, which assumes a simple cosine dependence of the single scattering phase function, through approximation of the phase function, P_d, by a truncated forward scatter peak and a two-term phase function expansion,

$$4\pi\, P_d(\beta) = 2f'\Delta(1-\cos\beta) + (1-f')(1+3g'\cos\beta) \quad (7)$$

where f' is the fractional scattering represented by the forward peak and g' is the asymmetry factor of the truncated phase function. In effect, the delta-Eddington approximation transforms most of the enhanced radiance in the solar aureole into the direct solar flux component, and it is generally assumed that

$$f'(z) = g^2(z)\,. \quad (8)$$

This assumption is commensurate with representation of the actual phase function with a single term Henyey-Greenstein phase function. Alternate expressions are required (see McKellar and Box, 1981) for other phase function representations such as the 2-term Henyey-Greenstein functions. Joseph *et al.* (1976) show that calculations of radiative transfer with the delta-Eddington approximation can be carried out with the standard Eddington computer code (Shettle and Weinman, 1970) with the following changes of variable

$$\Delta\tau' = (1-\omega f')\,\Delta\tau\,, \quad (9)$$

$$\omega' = \omega(1-f')\,/\,(1-\omega f')\,, \quad (10)$$

and

$$g' = (g-f')\,/\,(1-f')\,, \quad (11)$$

where $\Delta\tau$ is the optical thickness of the layer and ω is the single scattering albedo.

As an integral part of the technique for estimating directional contrast transmittance, the products of the Eddington computer program (Shettle and Weinman, 1970) are used directly to calculate the second term on the right hand side of Eq. (6).

From the standard Eddington approximation, the diffuse radiance is assumed to be given by

$$L(z,\theta',\phi') = L_D(z) + L_{D'}(z)\cos\theta'\,. \quad (12)$$

As shown by Shettle (1981), if we substitute Eq. (12) and the delta-Eddington approximations given by Eq. (7), (8) and (11) into the last term of Eq. (6) and integrate over θ' and ϕ', we have

$$\iint_{4\pi} L(z,\theta',\phi')P(z,\beta)s(z)d\Omega$$

$$= s(z)\,[L_D(z) + gL_{D'}(z)\cos\theta]\,. \quad (13)$$

A recent refinement in the above expression for the diffuse component of the path function consists of an additional term to help account for the effects of the azimuthal asymmetry in the background sky-terrain radiance distribution. The term is introduced as a rough approximation to an iteration of the singly scattered sunlight component of the path function. Its magnitude is assumed proportional to the single scattering component, ${}_s\epsilon(z)P(z,\beta)$, and proportional to the fractional contribution of the total diffuse energy, $4\pi\, L_D(z)$, to the sum of the total diffuse energy and singly scattered sunlight component at the level of computation. In other respects, the modification conforms with the extension of the delta-Eddington model introduced by Davies (1980); in particular, the contribution of the asymmetry term is proportional to $\sin\theta$, $\sin\theta_s$ and $\cos\phi$. The modified expression for the diffuse component of the path function is

$$\iint_{4\pi} L(z,\theta',\phi')P(z,\beta)s(z)d\Omega$$

$$= s(z)\,[L_D(z) + gL_{D'}(z)\cos\theta + gL_{D''}(z)\cos\phi]\,, \quad (14)$$

where

$$L_{D''}(z) = \frac{4\pi\, L_D(z)P(z,\beta)\,{}_s\epsilon(z)\sin\theta_s\sin\theta}{4\pi\, L_D(z) + P(z,\beta)\,\epsilon_s(z)} \quad (15)$$

Commensurate with the delta-Eddington approximations and Eq. (9), the expression for the solar scalar irradiance at altitude z is

$${}_s\epsilon(z) = {}_s\epsilon(\infty)\exp(-\tau_x\,/\cos\theta_s)\,, \quad (16)$$

where ${}_s\epsilon(\infty)$ is the extraterrestrial solar scalar irradiance. The optical depth τ_x is assumed equal to the delta-Eddington optical depth, τ', everywhere except within the forward peak ($\beta < 25$ deg) where τ_x is equal to the unmodified value of τ. Substituting Eqs. (13) and (14) into Eq. (6), the expression for the path function becomes

$$L_*(z,\theta,\phi) = s(z)\,[P(z,\beta_s)\,{}_s\epsilon(\infty)\exp(-\tau_x\,/\cos\theta_s)$$

$$+ L_D(z) + gL_{D'}(z)\cos\theta + gL_{D''}(z)\cos\phi]\,. \quad (17)$$

2.2 Calculation of Sky and Terrain Radiance

For an assumed plane parallel and horizontally homogeneous atmosphere, the directional path radiance, $L_r^*(z,\theta,\phi)$, and the radiance, $L(z,\theta,\phi)$, can now be calculated from Eqs. (1), (2) and (17) through finite summation over adjacent atmospheric layers using the trapezoidal rule. For upward paths of sight, the inherent background radiance of clear sky at target altitude is given by

$${}_bL_o(z_t,\theta,\phi) = L_\infty^*(z_t,\theta,\phi)\,, \quad (18)$$

where $L_\infty^*(z_t,\theta,\phi)$ is the path radiance as determined at altitude z_t for the slant path from the top of the atmosphere to z_t. Looking downward, the inherent background radiance for the case of uniform Lambertian reflectance and a horizontal surface is given by

$$ {}_bL_o(z_t,\theta,\phi) = T_{ro}(z_t,\theta)R(\theta,\phi)E(0,d)/\pi + L^{*}_{ro}(z_t,\theta,\phi)\,, \tag{19}$$

where $R(\theta,\phi)$ is the local surface reflectance, $E(0,d) = \epsilon_s(0)\cos\theta_s + \pi[L_D(0) + 2/3L_{D'}(0)]$ is the downwelling irradiance at the surface, and T_{ro} is the transmittance of the slant path from the surface to target altitude z_t.

2.3 Comparisons with Other Model Calculations

Tests were carried out to evaluate the performance of the simplified model for the radiance calculations as described above. Model calculations of radiance distributions were compared with the results calculated from more comprehensive radiative transfer models, which are mathematically precise but in general require relatively large computer capacity and time for the radiative transfer calculations. For these tests, the comparative accuracy was determined under the assumption that the physical system is perfectly observed, and the input data are identical for the approximate operational model and, the comprehensive numerical models. The set of examples used for the analysis were selected from those proposed by the ad hoc Working Group of the Radiation Commission, International Association of Meteorology and Atmospheric

Table 1. Summary of numerical comparison cases listed in the Working Group Report (Lenoble, 1977) of the Radiation Commission, IAMAP, for 5 reference atmospheres.

Case	Atmosphere	Optical Thickness	Single Scattering Albedo	Solar Zenith Angle
1	Haze L	1	1.0	0°
2	Haze L	1	0.9	0°
3A	Haze L (ϕ = 0°)	1	0.9	60°
3B	Haze L (ϕ = 90°)	1	0.9	60°
3C	Haze L (ϕ = 180°)	1	0.9	60°
4	Cloud	64	1.0	0°
5	Cloud	64	0.9	0°

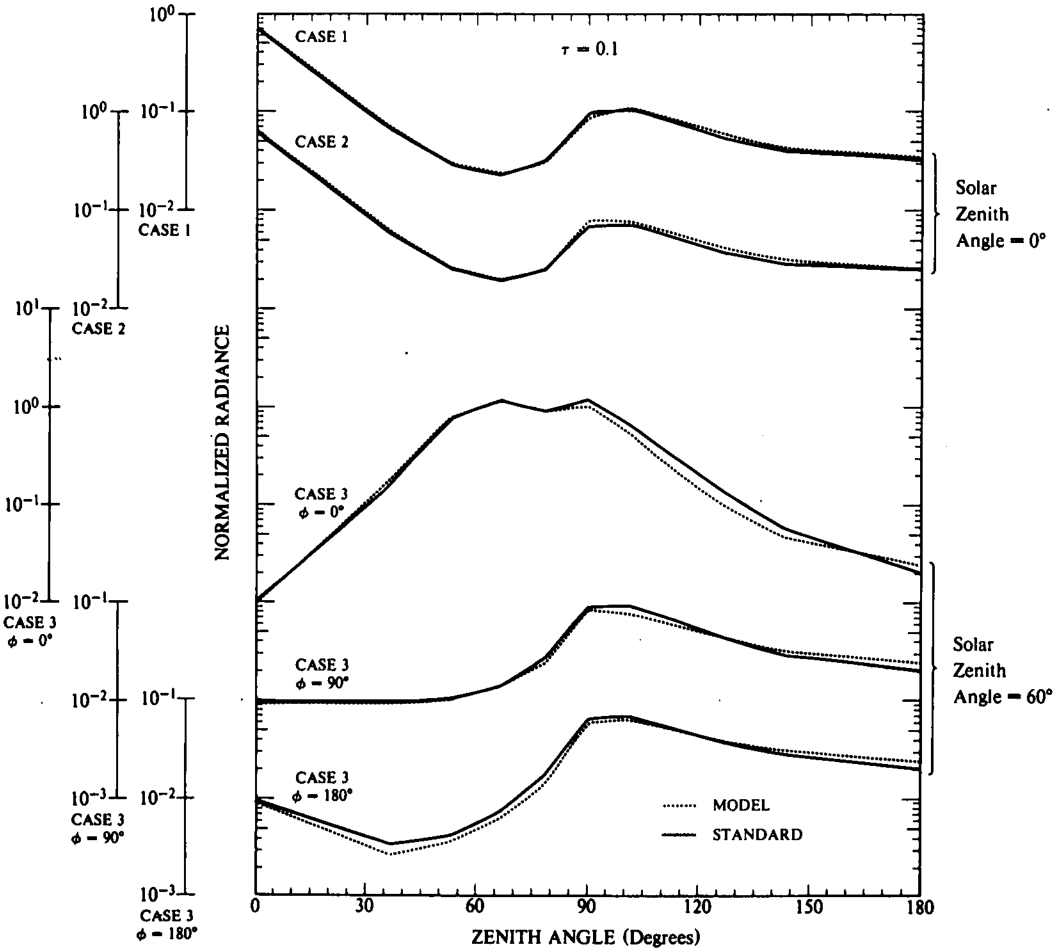

Fig. 1. Comparative radiance calculations for optical depth 0.1 for reference cases 1,2 and 3. Model results (dashed lines) are compared with the spherical harmonics method, (Lenoble, 1977), (solid lines). Optical parameter data for each case are given in Table 1.

Physics (Lenoble, 1977, see Table 1). The results of the spherical harmonic method listed in the Working Group report were chosen for a reference standard since comparative calculations using this method were presented for all five test cases. A single layer, plane parallel and homogeneous atmosphere with a black underlying surface was prescribed in each case. Three cases have a Haze L (Deirmendjian, 1969) aerosol particle distribution with an optical thickness of 1, and the other two have assumed cloud particle distributions with an optical thickness of 64. The phase function for single scattering and the single scattering albedo are specified for each case. Comparative results of the radiance calculations are illustrated in Figs. 1-4.

It is important to note that the agreement among the more rigorous numerical methods, as given in the Working Group report, is generally within a few percent depending upon the completeness of scattering history retained in the calculations. We see from Fig. 1 that the departures of the simplified model radiance calculations from the reference values for the haze cases are significantly larger, yet the indicated accuracy is good when considered in context with the uncertainties and completeness of the observational data base from which the estimates must be derived in operational practice. The simplified model requires only a few seconds of large scale computer time for each case, and the model is designed for easy microprocessor application for real time requirements. The approximations inherent in the computationally fast model serve to smooth out the asymmetry in the calculated radiance component due to the scattering of incident diffuse light; hence it is expected that the error of estimate would continue to increase somewhat in the solar azimuthal plane (ϕ = 0–180 deg) as the solar zenith angle increases beyond 60°.

The relative effectiveness of the azimuthal asymmetry term, $g\,L_{D}''\cos\phi$, is illustrated in Table 2. Model calculations for Case 3 (θ_s = 60 deg, ω=0.9) are listed with and without the azimuthal component contribution for comparison with the reference model results. It is evident that the accuracy of Eq. (17) is much better with the azimuthal correction. However, systematic errors remain such that further study of this aspect of the modeling procedures is particularly important.

The relative performance of the model calculations of radiative transfer in a high extinction environment is illustrated in Figs. 3 and 4. Both of the cloud examples in the reference series assume an overhead sun position.

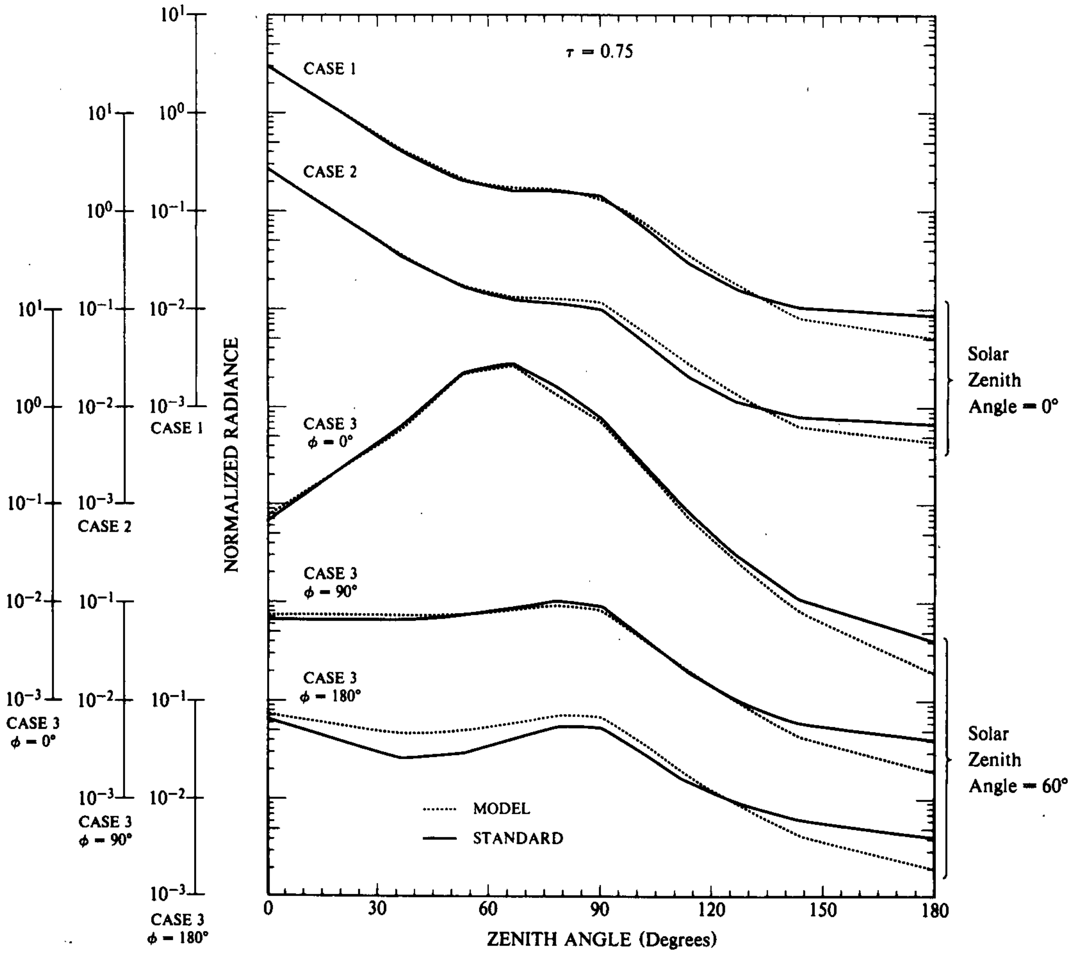

Fig. 2. Same as Fig. 1 except for 0.75 optical depth.

Table 2. Comparison of Case 3 radiance distributions as calculated by the Spherical Harmonics method (column SH), the simplified model without azimuthal asymmetry term (column A), and simplified model with the azimuthal asymmetry term (column B). The solar zenith angle is 60 deg. Calculations are shown for a level near the top of the haze layer ($\tau = 0.1$) and a level near the base ($\tau = 0.75$). Note that the azimuthal term, $g\, L_{D''} \cos\phi$, is zero for ϕ=90 deg, hence columns A and B are identical.*

$\tau = 0.1$

	ϕ=90°		ϕ=0°			ϕ=180°		
μ	SH	A	SH	A	B	SH	A	B
1	1.01-2	9.58-3	1.01-2	9.58-3	9.58-3	1.01-2	9.58-3	9.58-3
.8	9.50-3	9.43-3	1.65-1	1.66-1	1.82-2	3.50-3	3.84-3	2.79-3
.6	1.04-2	1.04-2	7.78-1	7.50-1	7.84-2	4.30-3	5.29-3	3.79-3
.4	1.42-2	1.38-2	1.17-0	1.11-0	1.17-0	7.46-3	9.14-3	6.55-3
.2	2.75-2	2.42-2	9.07-1	7.90-1	8.89-1	1.78-2	2.00-2	1.43-2
-.2	9.11-2	7.72-2	6.50-1	3.80-1	5.30-1	6.92-2	8.51-2	6.47-2
-.4	6.56-2	5.92-2	3.08-1	1.59-1	2.21-1	5.11-2	6.40-2	5.10-2
-.6	4.32-2	4.36-2	1.36-1	7.52-2	9.78-2	3.72-2	4.84-2	3.92-2
-.8	2.87-2	3.24-2	5.74-2	4.04-2	4.75-2	2.83-2	3.84-2	3.21-2
-1.0	2.00-2	2.47-2	2.00-2	2.47-2	2.47-2	2.00-2	2.47-2	2.47-2

$\tau = 0.75$

	ϕ=90°		ϕ=0°			ϕ=180°		
μ	SH	A	SH	A	B	SH	A	B
1	6.73-2	7.64-2	6.73-2	7.64-2	7.64-2	6.73-2	7.64-2	7.64-2
.8	6.69-2	7.53-2	6.79-1	5.25-1	6.10-1	2.61-2	5.16-2	4.71-2
.6	7.38-2	7.72-2	2.30-0	2.00-0	2.21-0	3.00-2	5.77-2	5.19-2
.4	8.82-2	8.44-2	2.78-0	2.39-0	2.68-0	4.13-2	6.97-2	6.13-2
.2	1.05-1	9.44-2	1.61-0	1.03-0	1.30-0	5.56-2	8.59-2	7.34-2
-.2	4.41-2	4.36-2	2.66-1	1.66-1	2.39-1	2.92-2	4.68-2	3.48-2
-.4	1.94-2	2.03-2	8.41-2	5.12-2	7.20-2	1.48-2	2.18-2	1.77-2
-.6	1.00-2	1.02-2	2.95-2	1.89-2	2.53-2	8.96-3	1.15-2	8.97-3
-.8	5.98-2	4.67-2	1.10-2	6.73-3	8.60-3	6.24-3	6.23-3	4.57-3
-1.0	4.02-3	2.14-3	4.02-3	2.14-3	2.14-3	4.02-3	2.14-3	2.14-3

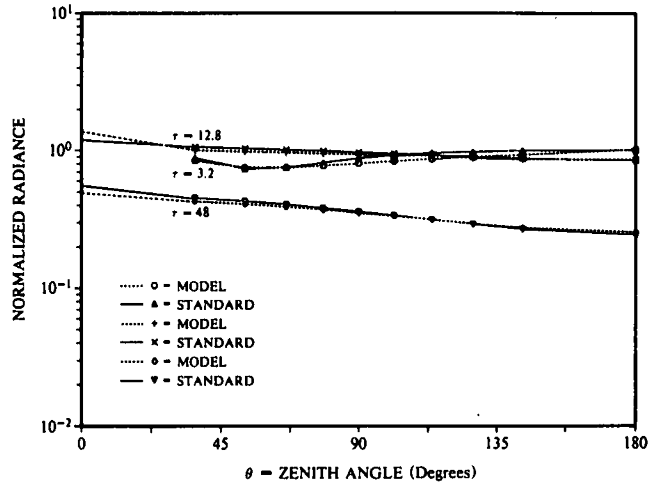

Fig. 3. Same as Fig. 1 except for cloud case 4 at optical depths 3.2, 12.8, and 48 and no absorption.

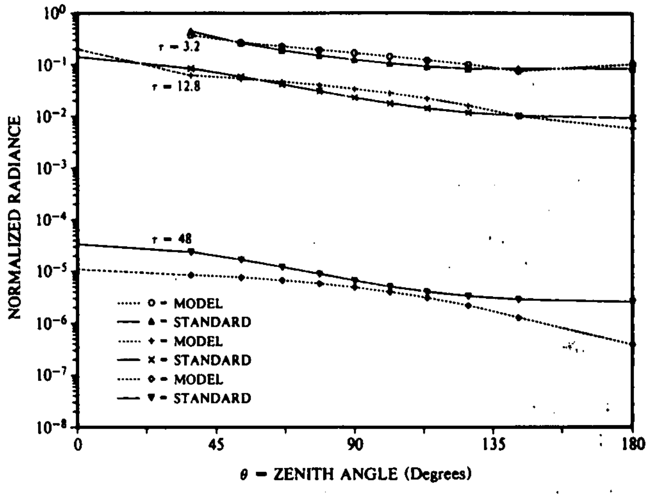

Fig. 4. Same as Fig. 3 except for cloud case 5 with single scattering albedo of 0.9.

The agreement with the reference model calculations holds well for both cloud cases, although the disparity increases with increasing depth for the case with strong absorption. The simplified model calculations of in-cloud radiance were carried out through division into sub-layers with boundaries corresponding to levels where reference model calculations were available. These subdivisions represent large increments of optical depth in the cloud cases. However, the estimates if in-cloud radiance are good in general over the full range of optical depth and observing angles shown in Fig. 3 and 4. A notable exception is for the data point directly upsun, $\theta=\theta_s=\phi=0$, at optical depth 3.2. The calculated values of in-cloud radiance for this data point result in overestimates by at least an order of magnitude and plot offscale in Figs. 3 and 4. The modeling procedures require important refinement in layer by layer resolution in order to handle combined effects of the rapid attenuation of the direct solar beam in the cloud near the upper limit of the cloud layer and the strong change in the single scattering phase function with scattering angle for β less than 5 deg. The large errors are confined to viewing paths within a few degrees of the sun and to the region near upper limit of the cloud layer. In this region, the singly scattered sunlight component makes a significant contribution to the path function and it changes rapidly along the path.

3.0 APPLICATION OF ANALYTIC TECHNIQUES

Environmental data and forecasts relevant to the determination of the background spectral radiance distribution and image transmission characteristics may be available in many forms and with varying degrees of completeness and representativeness. Emphasis has been placed on the development of a general modular format for requisite data entry seeking to take full advantage of all available information important for a particular application of the radiance model. A summary of input variables and alternate techniques for the specification of the atmospheric properties are included in Appendix A. Basic data entries include the wavelength representative of the sensor spectral characteristics, solar zenith angle, and the observational paths of interest for the problem at hand. Specification of the underlying surface reflectivity is discussed below in Section 3.1.

Several options are available for the input of specific atmospheric variables. One may introduce as many atmospheric layers as warranted by the accuracy and completeness of the meteorological observations or forecasts available for the specification of the optical parameter profiles. Minimum information for each designated layer includes the altitude limits, the average scattering coefficient, the average absorption coefficient and the single scattering phase function for aerosol particle scattering. Techniques for the representation of these variables are discussed in Sections 3.2 and 3.3.

3.1 Representation of Surface Reflectance

The background surface reflectance contributes to the calculated radiance distribution in two ways. First, the general or broad area average surface reflectance is entered to calculate the component of path radiance that is generated by light reaching the path through scattering from the underlying surface and in turn scattered in the direction of the sensor as given by Eq. (6). For a land surface, the reflectance is assumed to conform with Lambert's law, so that the resultant radiance is independent of observation angle and depends only on the downwelling irradiance and the average surface reflectance.

Second, the local background reflectance, which may differ from the area averaged reflectance discussed above, is entered for the determination of the inherent background radiance and its contribution to the apparent spectral radiance as given by Eqs. (1) and (19).

The above algorithms deal with surface reflectance over land areas. Another option, for use primarily over an open water surface, assumes specular surface reflection. Here the surface radiance is a function of both the viewing angle and the downwelling radiance distribution. For the water option, the Fresnel reflectance of the water surface as a function of observation angle is set equal to average values for a sea surface roughened by light surface winds (4m sec^{-1}). These values as calculated by Gordon (1969a), assume that the crosswind and upwind wave slope probabilities of Cox and Munk (1954) may be approximated by a single circular distribution of wave slopes.

3.2 Representation of Total Volume Scattering Coefficient

The spatial distribution of total volume scattering coefficient deserves prime consideration since it is the major determinant of visible spectrum contrast transmittance. Techniques for the specification of the scattering coefficient profile have been investigated during the course of the aircraft measurement and analysis program. Some of the results of these studies and their application to operational modeling procedures were summarized by Hering (1981). A brief review is given here for immediate reference.

For profile modeling purposes, it is important to consider a conservative measure of scattering coefficient that in the absence of local aerosol particle sources or sinks does not change appreciably following the air motion. The optical scattering mixing ratio, $Q(z)$, is such a parameter. As the vertical mixing within an identifiable atmospheric layer becomes more complete, $Q(z)$ becomes more constant with height within the layer.

The optical scattering ratio is defined

$$Q(z) = s(z)/s_R(z)\ , \tag{20}$$

where $s_R(z)$ is the total volume coefficient for Rayleigh scattering at altitude z. Note that

$$s(z) = s_R(z) + s_M(z) = \omega(z)\alpha(z)\ , \tag{21}$$

where $\alpha(z)$ is the extinction coefficient and $s_M(z)$ is the aerosol scattering coefficient. It follows that the aerosol scattering ratio is given by

$$s_M(z)/s_R(z) = Q(z) - 1 . \tag{22}$$

The aerosol scattering ratio also would be constant under conditions of complete aerosol mixing. An additional computational advantage of a scattering ratio representation is that it provides normalization with respect to both density altitude and wavelength.

Profiles of $Q(z)$ derived from the extensive series of airborne optical measurements made by the Visibility Laboratory, reveal large variability depending upon the aerosol particle source strength and the nature of the convective and turbulent mixing processes. The problem is to model the essential characteristics of the $Q(z)$ profiles in a way that recognizes operational observing and forecasting limitations yet takes maximum advantage of existing capabilities. A prominent feature of the daytime aircraft soundings over inland areas was the marked tendency for $Q(z)$ to remain essentially constant with height within the boundary layer, and also in the relatively haze-free region of the upper troposphere above the primary haze layer. It should be emphasized that the assumption of constant scattering ratio with height does not hold well for ground-based stable layers with little vertical mixing such as those associated with the nocturnal formation of fog. However, for application to problems of contrast transmittance in hazy atmospheres in the daytime following the dispersion of any surface inversion existing at sunrise, a simple 3-layer troposphere model with constant $Q(z)$ in each layer provides in most cases a good first approximation of the aerosol scattering profile. Thus, the forecasting problem is reduced to the prediction of the upper altitude limit of mixed boundary layer and the average scattering ratio within each layer. An evaluation of model representations of the high resolution scattering ratio profiles as measured during several deployments of the instrumented aircraft in western Europe is given in Hering (1981).

Three examples of scattering coefficient profiles as measured by the integrating nephelometer are shown in Fig. 5. Each experimental flight usually included profile measurements with 4 spectral filters having peak wavelengths of 475, 550, 660, and 750 nm. The 4 profiles were measured sequentially over approximately a 2-hour period. Data for individual profiles were extracted at 30-m intervals. Figure 5 illustrates some recurrent features of the lower tropospheric profiles; the well mixed boundary layer in late morning and afternoon over inland areas of northern Europe (Soesterberg profile), the multi-structured profile in low-level fog conditions offshore near Rodby, Denmark, and the deep haze layer typical of the summer profiles measured in the Mediterranean Sea area (Trapani, Sicily).

Cursory analysis of a large number of simultaneous aircraft measurements of temperature and scattering coefficient profile structure indicate that a temperature lapse rate equal to the standard lapse rate of 6.5°C per km or greater will support rather complete vertical mixing of aerosol particles in the size range contributing predominantly to extinction in the visible portion of the spectrum. On the other hand, atmospheric layers of thickness greater than about 300 m and lapse rate less than about 4.5°C per km significantly inhibit vertical mixing and in general appear sufficient to cap the mixed boundary layer.

3.3 Representation of Single Scattering Phase Function and Single Scattering Albedo

The single scattering phase function $P(z,\beta)$ as employed in Eq. (6) is a bulk parameter of the atmos-

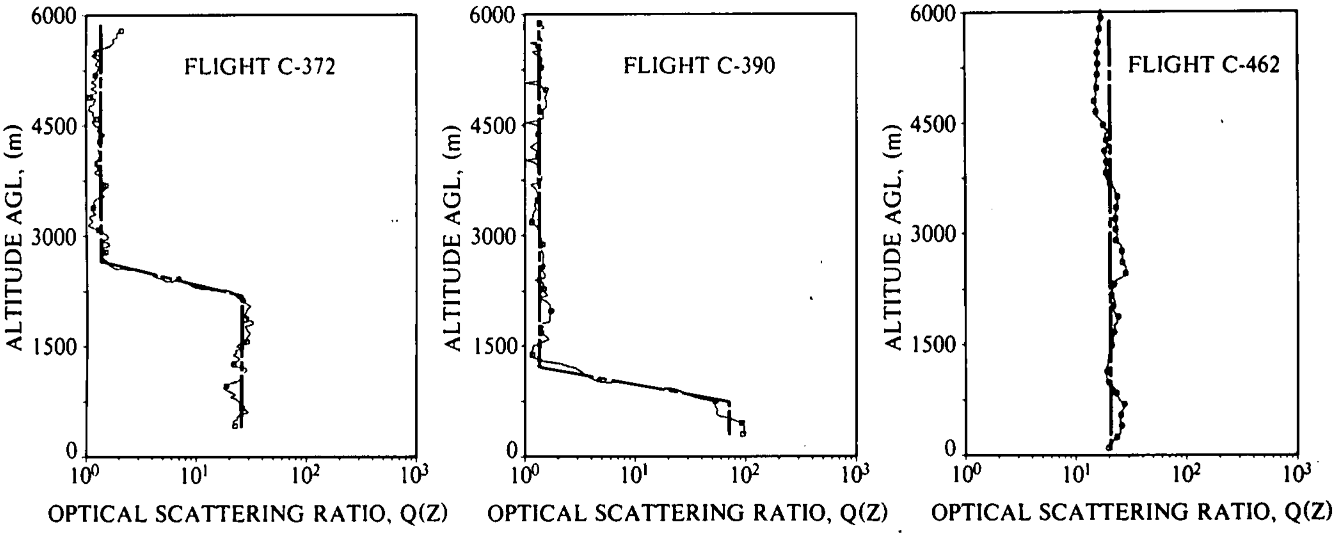

Fig. 5. Scattering ratio profiles as measured for flight C-372 (Soesterberg, Netherlands), flight C-390 (Rodby, Denmark) and flight C-462 (Trapani, Sicily). The heavy dashed line is an objective model representation of the profile. The spectral nephelometer measurements were corrected for the effects of incomplete purging of the instrument.

pheric layer, representing the combined aerosol and Rayleigh phase functions. It is given by

$$P(\beta,z) = \frac{P_R(\beta) + [Q(z) - 1]P_M(\beta,z)}{Q(z)}, \quad (23)$$

where $P_M(\beta,z)$ is the phase function for aerosol scattering and the theoretical Rayleigh phase function is

$$P_R(\beta) = 3(1 + \cos^2\beta) / 16\pi . \quad (24)$$

The phase function for single scattering has the normalized form,

$$\int_{4\pi} P(z,\theta,\phi)d\Omega = 1 . \quad (25)$$

The computational scheme offers several options for specification of the average single scattering phase function $P(z,\beta)$, for each designated atmospheric layer. Detailed estimates of $P_M(\beta)$ available from prescribed aerosol models such as those associated with LOWTRAN (Shettle and Fenn, 1979), may be entered directly and used in a table look-up format. A second option is the representation of the aerosol phase functions by two-term Henyey-Greenstein functions (Irvine, 1968) as follows,

$$P_M(\beta,g_1,g_2,c) = c\,P_{HG}(\beta,g_1) + (1 - c)\,P_{HG}(\beta,g_2) , \quad (26)$$

where

$$P_{HG}(\beta,g) = (1 - g^2)/ [4\pi(1 - 2g\cos\beta + g^2)^{3/2}] , \quad (27)$$

and the asymmetry factor, g, is given by

$$g = \frac{1}{2}\int_0^\pi P(\beta)\cos\beta \sin\beta \, d\beta . \quad (28)$$

To the extent that the Henyey-Greenstein asymmetry factors, g_1 and g_2, and the partitioning factor, c, can be estimated from reference atmosphere calculations they can be entered for the specification of the required scattering phase functions. In the absence of information that may serve to identify the directional scattering properties of individual aerosol layers, yet another option may be used as described in Hering (1981). Empirical functions were developed which prescribe the Henyey-Greenstein function parameters, g_1, g_2, and c, as a function of the scattering ratio $Q(z)$. The derived expressions are based to a large extent on the average phase functions for selected ranges of scattering coefficient as measured by Barteneva (1960).

The other direct-entry variable for each designated atmospheric layer is the single scattering albedo, $\omega(z)$. It is defined by the expression

$$\omega(z) = s(z)/\alpha(z) . \quad (29)$$

So that the fraction of radiation absorbed for each single photon collision is $1 - \omega(z)$. Commensurate with other variables, $\omega(z)$ is introduced as a bulk parameter and is a measure of the combined absorption effects of both air molecules and aerosol particles. In the visible spectrum, $\omega(z)$ in the boundary layer ranges from 1.0 (no absorption) to less than 0.7 in urban atmospheres with appreciable carbon concentration.

4.0 APPLICATION TO OVERCAST SKY CONDITION

The clear-sky modeling concepts and computational scheme can be applied in the same form to calculate the visible spectrum radiance fields and contrast transmittance for continuous cloud cover conditions. Given reliable empirical estimates of cloud optical properties, the delta-Eddington method yields good estimates of the irradiance profiles in overcast atmospheres. In turn, the directional path radiance fields and the contrast transmittance for selected slant paths may be calculated from the expressions given in Section 2. In practice, one must rely on cloud model estimates of the optical depth, the single scattering phase function, and the single scattering albedo as a function of standard cloud type.

4.1 Estimates of Optical Depth from Conventional Cloud Observations

Rough empirical approximations of the average optical depth as a function of cloud type were derived through reference to a climatological summary of the SOLMET (1977) data base as included in a report by Shapiro (1982). The SOLMET data base was compiled by the National Climatic Center under the sponsorship of the Department of Energy. It consists of a long record of edited and adjusted solar radiation data (hourly averages) for 26 National Weather Service stations spread throughout the United States coupled with the conventional hourly surface observations for these stations. The climatological tabulations of the broad-band solar irradiance were available in the form of averages for all stations and all seasons for standard cloud types (10/10 cloud cover) for selected solar zenith angles. These data were combined with the average irradiance data for cloudless skies to calculate the ratio of the average broad-band irradiance for the sky covered by clouds of specific types to the average broad-band irradiance for cloudless atmospheres.

It is important to note that the calculated overcast/clear irradiance ratios for different cloud types and solar angles derived from the SOLMET data base agree very closely with the average overcast/clear irradiance ratios calculated by (Haurwitz (1948)) for comparable cloud classifications using 8 years of observations at the Blue Hill Observatory in Massachusetts.

To the extent the fractional transmittance for the different cloud types as determined from the broad-band

(.295-2.8μm) pyronometer measurements are representative in general of the visible spectrum, one can use the delta-Eddington method to estimate the effective average optical depth associated with the individual cloud types. The results of trial calculations made to obtain rough estimates of the optical depth of standard cloud types are shown in Fig. 6. Through successive approximation, determination was made of the best least-squares fit between the average overcast/clear irradiance ratios as a function of solar zenith angle derived from the SOLMET data base and the corresponding values calculated with the delta-Eddington model. A central wavelength of 550 nm and an average surface reflectance of .07 were used for the model calculations and absorption within the cloud layer was assumed negligible. The altitude limits of the cloud layers were chosen so as to conform in general with typical values for each cloud type.

Except as noted below, the asymmetry factor, g, was assumed equal to .85 in calculations for all cloud types. It should be emphasized that the model calculations are sensitive to variations in g. However, in the case of water clouds, the variation in g is small (Twomey, 1980) and the resultant uncertainties are negligible in comparison with the natural variations in optical depth for each cloud type. In the case of ice clouds, very significant fluctuations in g are associated with variations in ice crystal size, shape, and orientation. For this reason, as emphasized by Welch, *et al.* 1980, attempts to estimate the optical depth of clouds composed of non-spherical particles from observed cloud reflectance (or transmittance) are subject to considerable error. For comparison purposes, estimates were derived for both a nominal value of .85 for the asymmetry factor in cirrus clouds and a marked reduction to .75. In agreement with the results of Welch, *et al.* 1980, the calculated optical depths corresponding to the same average cirrus cloud transmittance differ by more than a factor of 2 for the two assumed values of g as shown in Table 3.

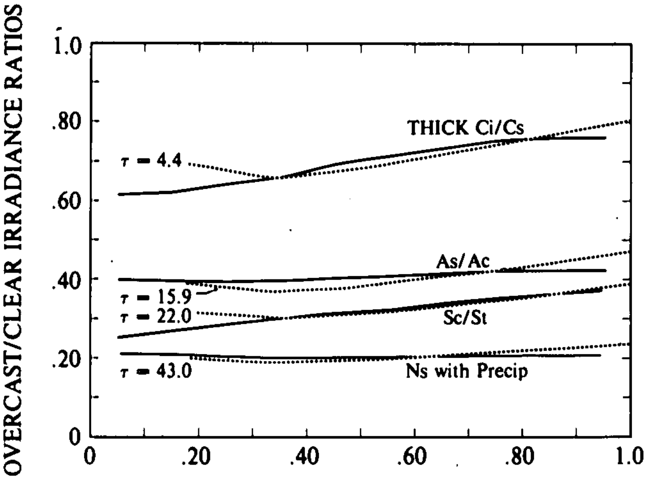

Fig. 6. Average overcast/clear irradiance ratios from SOLMET data base (solid lines) and estimated with delta-Eddington approximation (dashed lines). Listed are the values of optical depth, τ, giving the best correspondence.

Table 3.

The approximate average and ± standard deviation values of optical thickness for various cloud forms as calculated using the delta-Eddington approximation and the SOLMET data base. The assumed value of asymmetry factor is given in column g. For reference purposes a value of scattering ratio, Q(550nm), is shown for each value of $\Delta\tau$ as determined for a cloud of geometric cloud thickness of 1 km and a base altitude as indicated.

Cloud Type	Optical Thickness	Q(550 nm) $\Delta z = 1\,km$	Base Alt.(km)	g
St/Sc	22.0	2200	1 km	
	13.5	1350		.85
	41.0	4100		
Cu/Cb	15.0	1500	1 km	
	10.0	1000		.85
	26.5	2650		
As/Ac	15.9	1950	3 km	
	9.8	1200		.85
	25.3	3100		
Ns (precip.)	43.0	4300	1 km	
	20.7	2700		.85
	126	12600		
Ci/Cs (thick)	4.4	750	6 km	
	3.2	550		.85
	6.2	1050		
Ci/Cs (thin)	1.5	250	6 km	
	0.7	125		.85
	2.4	400		
Ci/Cs (thick)	2.6	440	6 km	
	1.5	250		.75
	4.3	725		
Ci/Cs (thin)	0.7	120	6 km	
	0.2	30		.75
	1.5	250		

As indicated by the examples in Fig. 6, one can obtain a rather close fit of the average irradiance ratios *vs* solar zenith angle for the standard cloud types using the delta-Eddington model. The optical depths corresponding to the closest approximations of the SOLMET data averages for each cloud type are listed in Table 2. Rough estimates of the variability in the optical depth were obtained in a similar manner from the SOLMET data. The tabulated values of optical depth labeled "± rms variation" were calculated from SOLMET irradiance ratios equal to the average ratio for a given cloud type and solar zenith angle plus and minus the root-mean-square departure of the individual SOLMET values of irradiance ratio from the averages for that cloud type.

Thus, for overcast sky conditions, the radiance field at any altitude may be calculated using the optical properties given in Table 2 corresponding to the observed cloud type and altitude and the estimated input variables for the additional atmospheric layers above and below the cloud layer. The optical scattering ratio for the cloud layer is given by the cloud optical depth divided by the Rayleigh optical depth for the corresponding altitude interval of the cloud. In view of the uncertainty in the asymmetry factor for cirrus cloud particle distributions, estimates for g equal to .75 are shown as well as for the more representative value of .85. In the absence of other information, operational use of the results for g=.85 are suggested.

Several comparisons of the calculated spectral radiance fields with the high resolution aircraft measurements for both clear and cloudy atmospheres are given in the following section.

5.0 COMPARISONS OF MODEL RESULTS WITH MEASURED DATA

From the fundamental Eq. 4, we note that the reliability of model calculations of slant-path contrast transmittance are dependent directly upon the accuracy with which the radiance fields $L_r(z, \theta, \phi)$ are determined. For this reason, continuing emphasis has been given to direct comparisons of the radiance fields as calculated by the modeling procedures and the corresponding radiance fields observed as part of the extensive airborne measurement program. The upper and lower scanning radiometers measured the apparent radiance fields surrounding the aircraft as it probed the lower troposphere up to an altitude of 6 km. The processed radiometer measurements provided data with 5-degree resolution in the 4 specific wavebands commensurate with the integrating nephelometer measurements of total volume scattering coefficient (peak wavelengths of 475, 550, 670 and 750 nm).

Several of the comparisons between model calculations and measured radiance fields are shown in Figs. 8 to 12. The plotted data are presented for either one of two vertical planes (0-180 deg or 90-270 deg) with respect to the solar azimuth and depict data sweeping from the nadir (θ = 180 deg) up through the horizon and zenith and then downward through the opposite horizon to nadir, as shown in Fig. 7. A series of examples were selected in order to illustrate model performance over a wide range of haze-layer extinction, solar zenith angle, and surface reflectance (land and sea) for both clear and overcast sky conditions.

The specific input data for each of the illustrated examples are listed in Appendix B. Except for the scattering mixing ratio profile in the lower troposphere, the other input variables were approximated by their average or climatological values. The scattering mixing ratio for the boundary layer was entered as determined directly from the nephelometer measurements for that particular flight profile. The scattering ratio for the upper troposphere and stratosphere during this period of minimal volcanic activity was held constant for all cases and set equal to a characteristic value of 1.2 at 550 nm. The mixing ratio for other wavelengths at upper levels was determined assuming the wavelength dependence of the aerosol scattering coefficient equal to $(\lambda/\lambda_{550})^{-1}$. The aerosol single scattering phase function for all haze layers and all cases was specified by a two-term Henyey-Greenstein function with parameters; g_1 = .714, g_2 = -.613, and c = .963. The corresponding values for the cloud layers are .890, -.660 and .980.

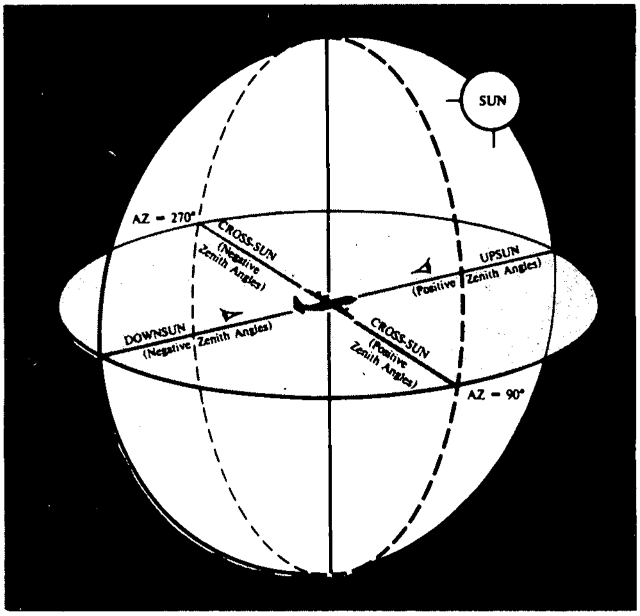

Fig. 7. Coordinate system for the calculation of sky and terrain radiance and slant-path contrast transmittance.

Optical depths for the overcast sky layers were specified equal to the average value for the observed cloud type as developed in Section 4 (see Table 2). The single scattering albedo and surface reflectance were assumed equal to average values for the prevailing conditions. For flights conducted over open water, the average Fresnel reflectance distribution for wind-ruffled sea (see Section 3.1) was used.

5.1 Comparative Results for Individual Flights

Flight C-379, Fig. 8, was a midday flight off the south coast of Lolland Island, Denmark. The example depicts the characteristic changes with altitude of the upper and lower hemisphere radiance fields under cloudless skies and light haze conditions. Note the characteristic uniformity and symmetry of the sea surface radiance fields in the cross-sun plane.

Flight C-466, Fig. 9, was conducted over open farmland and wooded areas in northwestern Germany. Scattered cirrus clouds and isolated patches of altocumulus were observed. A layer of moderate haze extended to an altitude of 1350m. Notice the marked fluctuations in the observed apparent terrain radiance associated with variations in ground cover (green and brown fields and dark

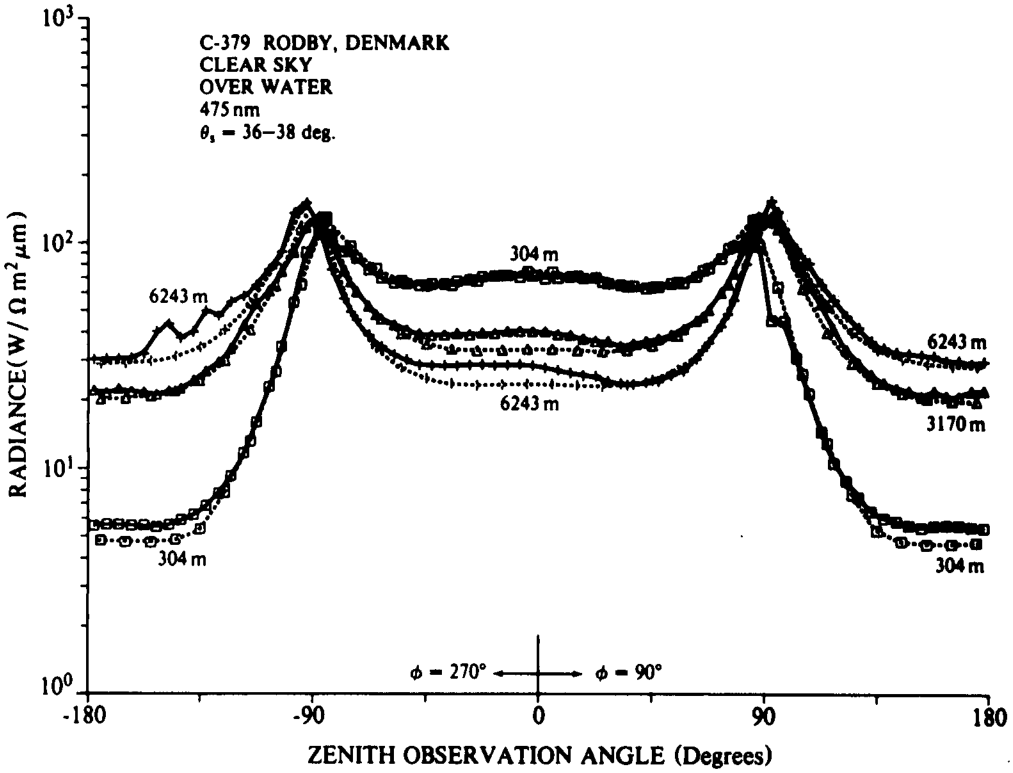

Fig. 8. Comparison of sky and terrain radiance as measured by airborne scanning radiometer (Johnson 1981d) (solid line) and model calculations (dashed line).

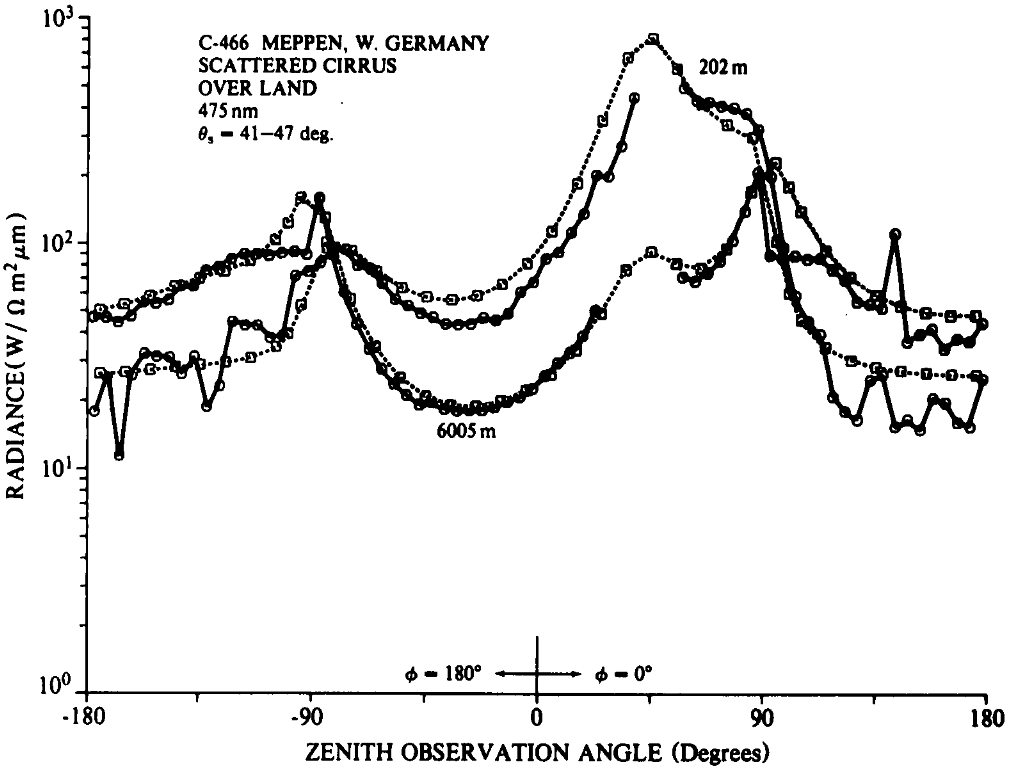

Fig. 9. Comparison of sky and terrain radiance as measured by airborne scanning radiometer (Johnson 1981d) (solid line) and model calculations (dashed line).

woods), as opposed to the smooth terrain radiance distribution calculated with the assumption of uniform Lambertian surface reflectance.

Flight C-469, Figs. 10 and 11, was an afternoon flight over open farmland in central Netherlands. The examples illustrate the variations in radiance fields with altitude in dense haze conditions. Depicted also are the characteristic differences in the radiance distributions as observed in the narrow blue passband (475 nm) as shown in Fig. 10 and in the near infrared passband (750 nm) shown in Fig. 11. Note in particular the reduction in overhead sky radiance at 750 nm associated with diminished molecular and aerosol particle scattering and the enhanced apparent terrain radiance due to the greater surface reflectance in the near infrared portion of the spectrum.

Flight C-401, Fig. 12, was a winter day flight with low sun elevation over a rural area in northwestern France. Scattered cumulus and scattered thin cirrus clouds were observed with a layer of light haze extending to an altitude of about 1 km. The relatively bright horizon in contrast with low overhead sky and terrain radiance is a prominent feature of low-sun radiance fields. As indicated by this example, the good agreement between model calculations and measured radiance fields characteristically found in the comparisons extends to the cases with low solar elevation angle.

Flight C-422, Fig. 13, is also an over water flight off the coast of Denmark, but on this day the sky was overcast with stratocumulus clouds having a base altitude of 1800m. Heavy haze was present at all levels below the cloud base. The example illustrates the highly symmetric and uniform distribution of cloud and sea radiance typical of measurements made with the flight path over open water and under an overcast cloud layer.

Flight C-465, Fig. 14, was an afternoon flight in mid summer over northwestern Germany. The sky was overcast with stratocumulus clouds having a base altitude of 1600m. A layer of light haze was observed below the cloud base. In contrast to the previous case, the radiance field was more irregular in structure due to the variations in cloud optical thickness and to the variations in ground cover reflectivity.

Flight C-435, Fig. 15, was a winter flight over a snow covered plateau in southwestern Germany. The sky was overcast with altostratus clouds with a base altitude of 3 km. The apparent radiance of the snow surface as measured at an altitude of 6 km is roughly equal to the apparent radiance of the overcast sky. The minimum values of lower hemisphere radiance are associated with underlying areas of dark woods having an effective average reflectance of about .04 in this case. Notice that the effective reflectance of the snow covered areas is somewhat higher than the average value of 0.75 that was assumed for the model calculations.

The correspondence between the field measurements and the model calculations illustrated above are representative in general of the many such comparisons made during the course of model development and validation. It should be emphasized that the accuracy of the illustrated model calculations is enhanced considerably by the availability of the detailed vertical profile of scattering coefficient in the boundary layer, which is the major determinant of the fluctuations in path radiance in the troposphere. On the other hand, the correspondence between the actual and calculated radiance fields could be improved through relaxation of the constraint that other input variables be held equal to their typical or average values. For example, identification of an aerosol model appropriate for the boundary layer in a given synoptic situation would provide estimates of the single scattering phase function and single scattering albedo that are more realistic than the prescribed overall average values used in illustrated comparisons. A brief assessment of the sensitivity of estimates of the maximum detection range of distant objects to uncertainties in both atmospheric and target factors is given in the following Section.

6.0 SENSITIVITY OF TARGET DETECTION RANGE TO ENVIRONMENTAL AND TARGET FACTORS

Diagnostic calculations have been made routinely during the course of the investigations to determine the sensitivity of the model calculations to variations in the input data. In prior investigations (Hering, 1981), attention was directed primarily toward analysis of the sensitivity of contrast transmittance to changes or uncertainties in the relevant optical properties of the atmosphere. The interpretations of these results are straightforward in that, except for scintillation effects, Eq. 4 describes completely the atmospheric effects upon contrast transmittance. On the other hand, contrast transmittance must be coupled with the effects of specific target factors to estimate the maximum distance an object can be detected and identified. A given change in the slant-path, contrast transmittance may or may not be critical for target detection depending the minimum contrast required for detection. Thus, the assessment of the combined influences of atmospheric and target factors is important.

For this purpose, analytic techniques were introduced into the computer program to calculate visual detection range as an additional output variable. The representation of target information and visual search factors in this preliminary analysis are greatly simplified. Nevertheless, the results provide important insight into the sensitivity of visual detection distance to changes in specific atmospheric variables for selected combinations of target characteristics.

6.1 Determination of Visual Detection Range

The analytic representations of the contrast thresholds for visual detection were derived from basic visual data from the Tiffany experiments (Blackwell, 1946) and the Visibility Laboratory experiments (Taylor, 1964) which were adapted and summarized by Gordon (1979). The graphical representations of threshold contrast as a function of angular target size shown in Fig. 16 are taken

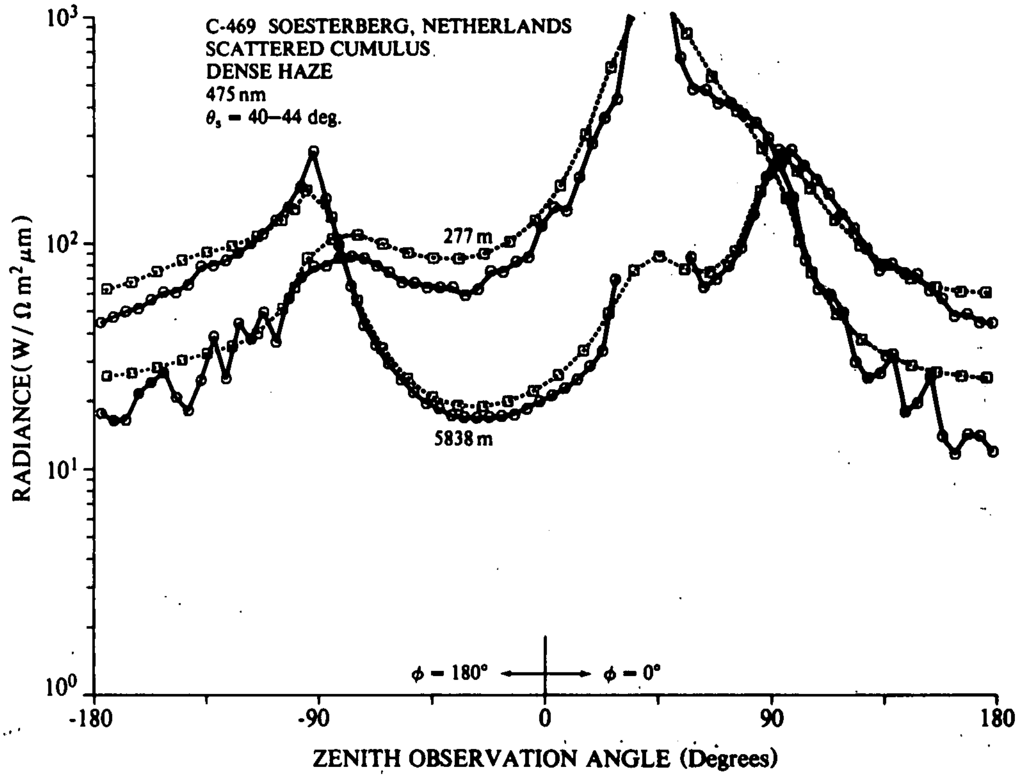

Fig. 10. Comparison of sky and terrain radiance as measured by airborne scanning radiometer (Johnson 1981d) (solid line) and model calculations (dashed line).

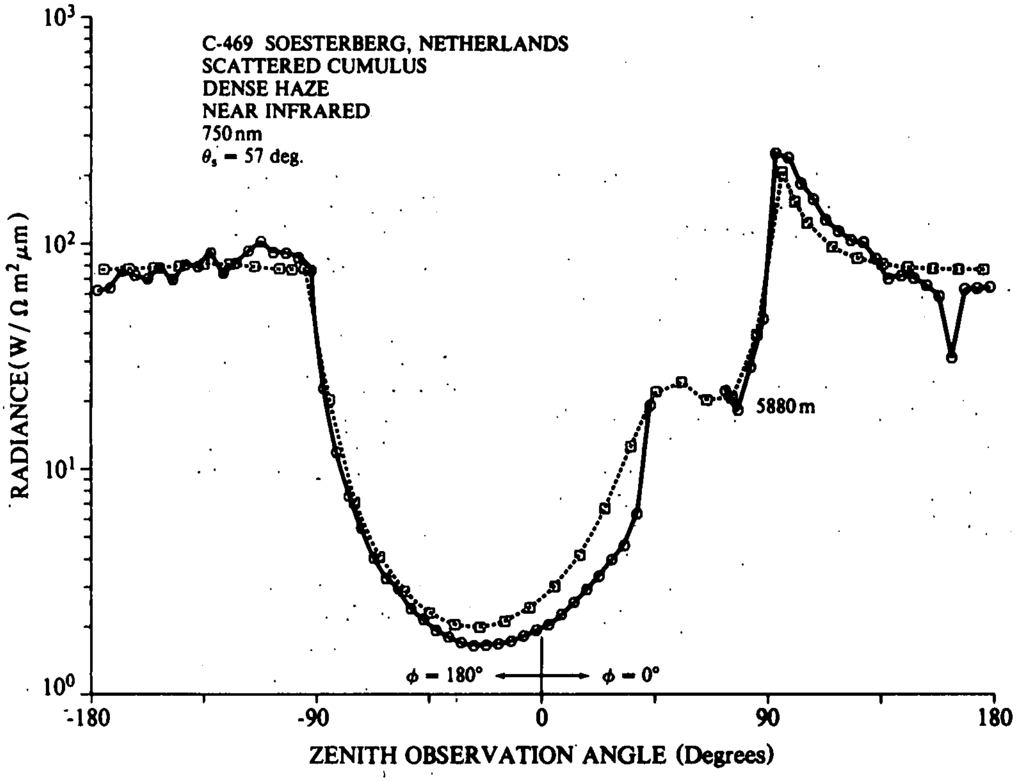

Fig. 11. Comparison of sky and terrain radiance as measured by airborne scanning radiometer (Johnson 1981d) (solid line) and model calculations (dashed line).

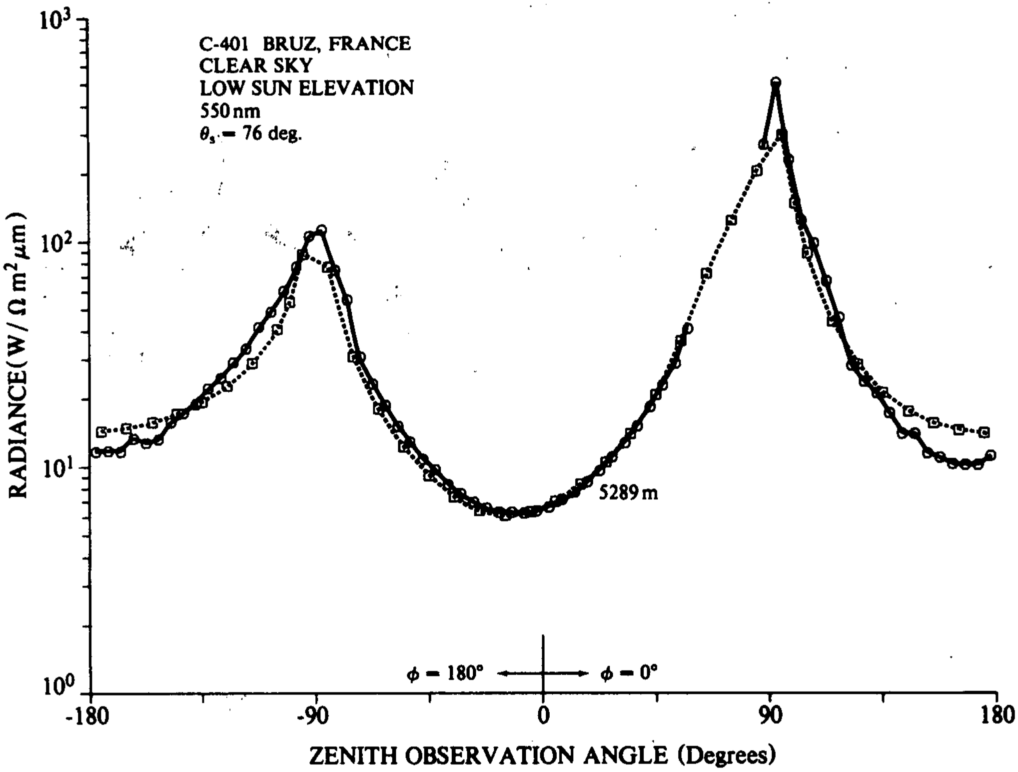

Fig. 12. Comparison of sky and terrain radiance as measured by airborne scanning radiometer (Johnson 1981d) (solid line) and model calculations (dashed line).

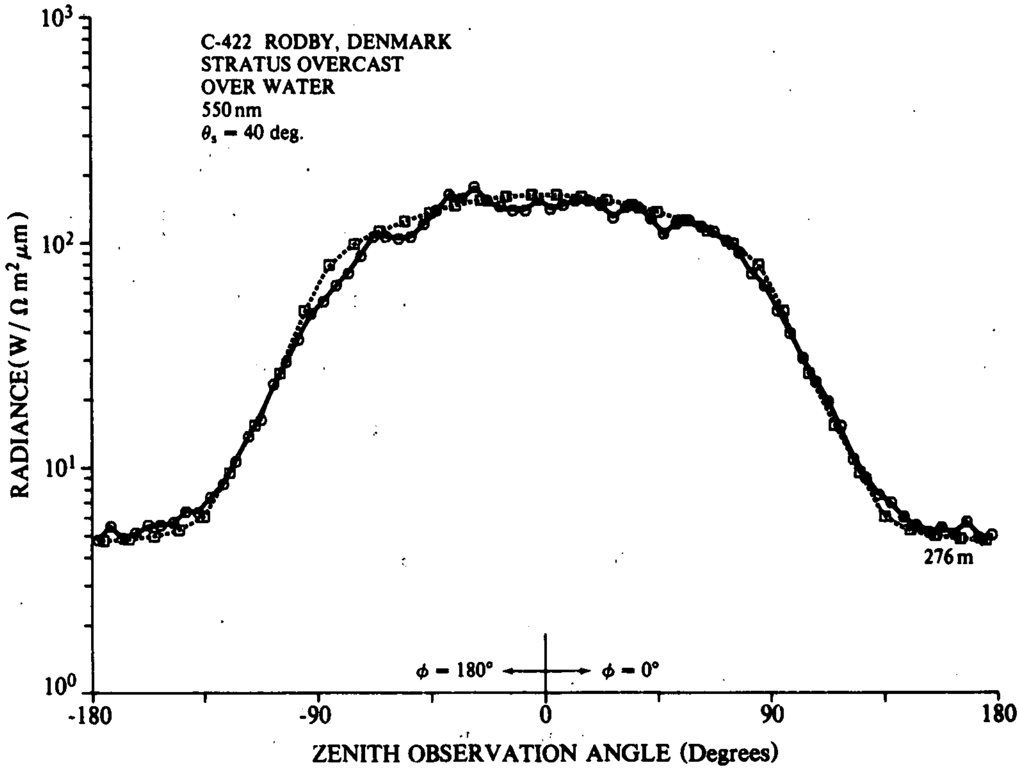

Fig. 13. Comparison of sky and terrain radiance as measured by airborne scanning radiometer (Johnson 1981d) (solid line) and model calculations (dashed line).

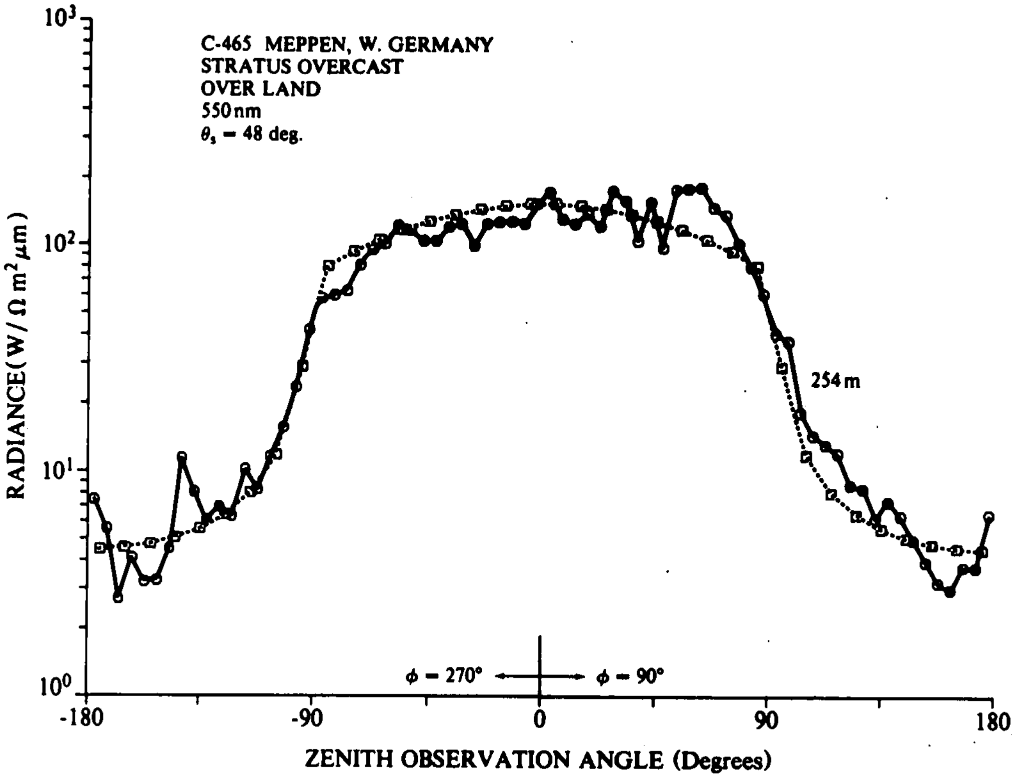

Fig. 14. Comparison of sky and terrain radiance as measured by airborne scanning radiometer (Johnson 1981d) (solid line) and model calculations (dashed line).

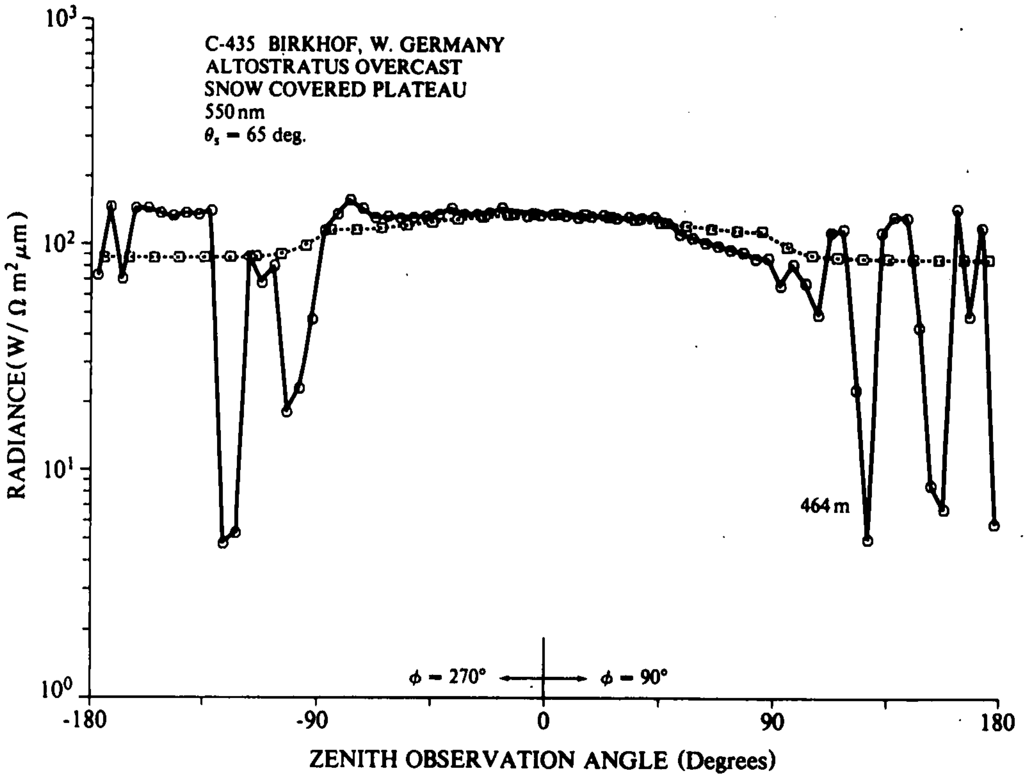

Fig. 15. Comparison of sky and terrain radiance as measured by airborne scanning radiometer (Johnson 1981d) (solid line) and model calculations (dashed line).

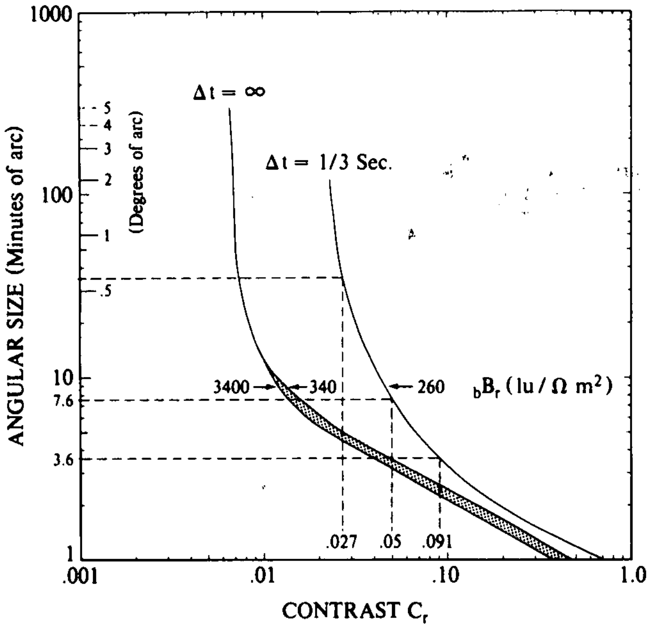

Fig. 16. Angular subtense of target as a function of threshold contrast for a 99 percent probability (confidence) of detection and a lack of knowledge of target position of ± 4 deg or more (Gordon, 1979). $_bB_r$ is the adaptation brightness and Δt is the assumed visual fixation (dwell) time.

directly from Fig. 1 of Gordon (1979). Two search modes are represented. The first corresponds to long duration viewing (>24 seconds, Tiffany data). The second corresponds to a viewing time of one-third of a second (Visibility Laboratory data), which is the approximate fixation time associated with search performed by the human eye (White, 1964).

From Fig. 16 we see that, for the normal range of daylight conditions, the visual contrast threshold does not vary significantly with background luminance. However, the contrast threshold does vary markedly with the angular subtense of the target. The relationships shown in Fig. 16, represent the contrast threshold associated with confident detection (99 percent probability) under conditions where the lack of knowledge of target position is ±4 degrees or more.

For application to the problem at hand, the prescribed relationships given in Fig. 16 were approximated analytically by the expression,

$$\ln \gamma = A+B(-\ln C_T) + C(-\ln C_T)^2 + D(-\ln C_T)^3 \quad (30)$$

where γ is the angular size of the target, C_T is the contrast detection threshold and A,B,C and D are the parameterization coefficients as determined for the two search modes.

Given the above method for the representation of target factors, let us now consider analytic representation of the model calculations of slant path contrast transmittance. The computational scheme provides discrete values of contrast transmittance for designated paths of sight. As an additional option, the contrast transmittance of air to ground observation paths for fixed values of azimuthal viewing angle and sensor altitude is represented through the method of least squares as a continuous function of path length (range) by the expression,

$$r = a+b[\ln \frac{C_r}{C_o}(z,\theta)] + c[\ln \frac{C_r}{C_o}(z,\theta)]^2 \quad (31)$$

Since the angular subtense of the target is less than a degree or so, the slant range, r, can be approximated by $r = d/\gamma$ where d is the effective diameter of the target. Given the inherent target contrast, C_o, the range associated with a selected value of apparent contrast C_r, is determined by Eq. 31. The maximum detection range for specified sensor altitude and azimuthal viewing angle corresponds to the range where $C_r = C_t$. The method of successive approximation yields rapidly converging solutions for maximum detection range from trial values of C_r and C_t using Eqs. 30 and 31.

6.2 Diagnostic Calculations of Visual Detection Distance

A series of additional model calculations were carried out to illustrate the relative sensitivity of target detection range to changes or uncertainties in some of the key variables. For this purpose, reference conditions were assumed which reflect a typical visual detection scenario for hazy atmospheres in the daytime. In an attempt to isolate the effects of fluctuations in individual factors, the procedure was to vary a given parameter over its normal range while holding all other reference conditions constant. The reference atmospheres used in this analysis are summarized in Appendix B (Ref. A for clear sky and Ref. B for overcast sky). The reference atmospheres have a surface equivalent visibility of 20 km and a boundary-layer hazy depth of 1 km. Except as noted, an ideal circular target is assumed having a diameter of 30m and an inherent contrast of one. The functional representation of psychophysical data of Taylor (1964) corresponding to the 0.33 sec fixation time (see Fig. 16) was used for the trial calculations except for the one comparative example (paragraph 6.2.5) based upon the Tiffany visual threshold data for a fixation time greater than 24 seconds.

Visual Horizontal Detection Distance versus Observer Altitude and Azimuthal Viewing Angle (Fig. 17).

For intermediate size targets of good inherent contrast, the maximum horizontal detection distance (ground range) increases significantly with increasing observer altitude in the lower troposphere above the boundary layer. The variations in ground range with azimuthal viewing angle are determined largely by the directional dependence of the path radiance as defined by the combined phase

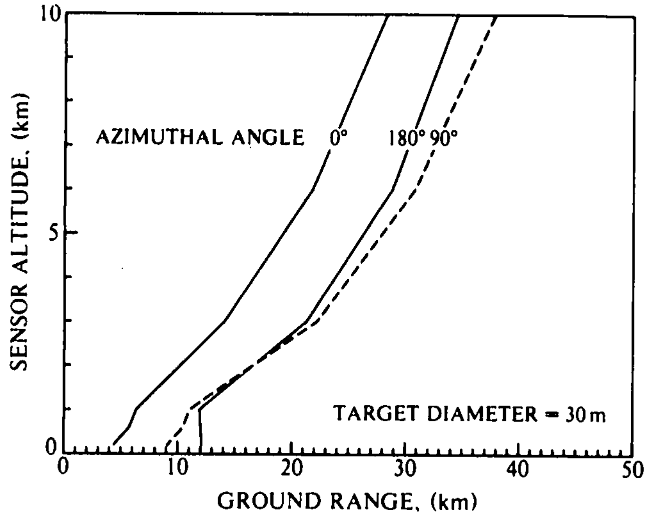

Fig. 17. Visual horizontal detection distance as a function of observer altitude and azimuthal observation angle.

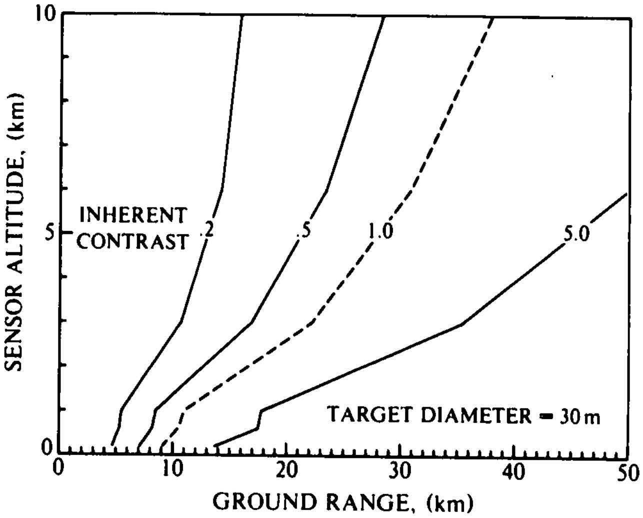

Fig. 18. Visual horizontal detection distance as a function of inherent contrast for 30-m target.

function for molecular and aerosol scattering. For the typical condition in the free atmosphere above the haze layer where the aerosol particles have low concentration, the difference in detection distance in the upsun ($\phi = 0$ deg) and downsun ($\phi = 180$ deg) viewing directions remains rather constant with increasing observer altitude above the boundary layer and increases with increasing solar zenith angle. Of special interest in Fig. 17 is the relatively small variation in detection range with azimuthal angle in the antisolar hemisphere as indicated by the rather close correspondence in the 180 degree (downsun) and 90 degree (cross sun) profiles. It should be noted that the trial calculations which follow in subsequent examples assume a 90-degree azimuthal viewing direction.

Visual Detection Distance versus Inherent Contrast (Fig. 18).

The rate of increase in visual detection range with increasing observer altitude depends significantly upon the initial target contrast. Notice in Fig. 18 the dramatic increase in detection range with increasing viewing altitude for bright targets viewed against a dark background ($C_o = 5$) as contrasted with the restricted increase in detection distance for low contrast targets ($C_o = 0.2$). As a point of reference information, the detection range is independent of the sign of the target contrast. For targets darker than the background, the lower contrast limit is $C_o = -1$ (black target). The inherent contrast of targets brighter than background is unbounded. The assumed reference value of target contrast of $C_o = 1$ (dashed curve) corresponds to the case where, under the same irradiance, the reflectivity of the target is twice the background reflectivity.

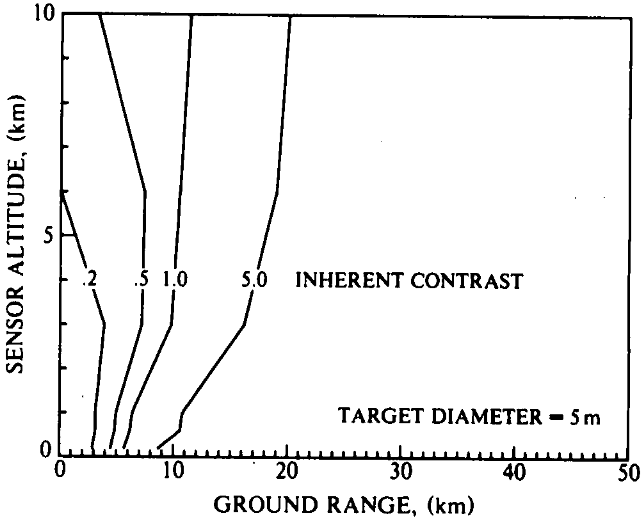

Fig. 19. Visual horizontal detection distance as a function of inherent contrast for 5-m target.

Visual Detection Distance versus Inherent Contrast for Reduced Target Size (Fig. 19).

Diagnostic model calculations for a smaller 5-m target diameter (Fig. 19) show the corresponding reduction in visual detection distance as compared with the results for the 30-m target (Fig. 18). Notice, for example, in the case of a target of 0.2 inherent contrast under the assumed conditions, there is little advantage in increased detection range to be gained by climbing to an observation altitude above the haze layer top and that the reference target having 0.2 contrast cannot be detected with 99 percent probability above a viewing altitude of 6 km. The calculated visual detection range for 5-m targets for this example is everywhere less than 12 km for targets having an inherent contrast less than one.

Visual Detection Distance as a Function of Environmental Factors (Fig. 20).

Sensitivity calculations of the response of ground detection range to selected changes in individual factors

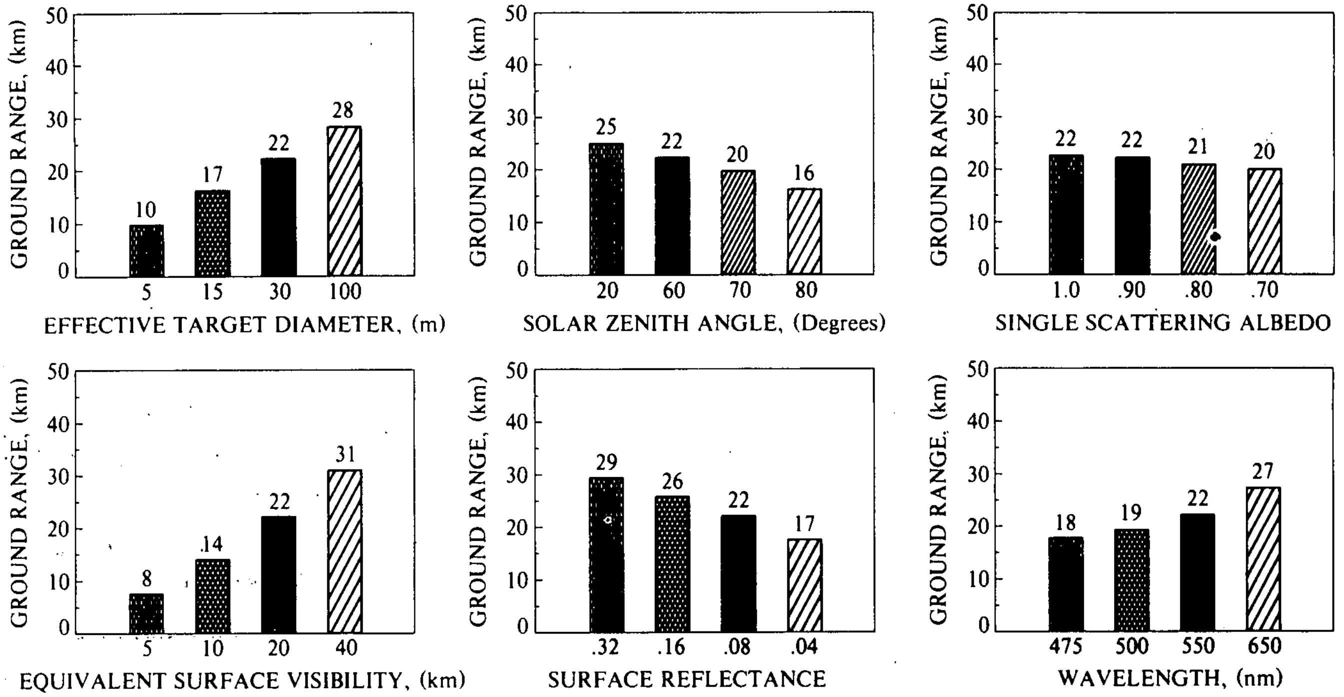

Fig. 20. Sensitivity of horizontal detection distance to changes in relevant factors. Solid bar in each case (22 km) corresponds to the calculation for reference target (30-m diameter) and reference atmosphere parameters. Surface target with a contrast of one is viewed against at a uniform background from an altitude of 3 km. For each case, all variables are fixed equal to reference values except for the variable under examination.

are shown in Fig. 20 for a ground target viewed from an altitude of 3 km. All variables except the factor under examination are held constant and equal to the reference values listed in paragraph 6.1 and Appendix B (Ref. A). The scattering and absorption coefficients are allowed to change only within the primary haze layer. The calculations assume a λ^{-1} wavelength dependence of the aerosol scattering coefficient and no changes in surface reflectance with wavelength. The illustrated changes in detection distance relative to changes in single scattering albedo were calculated assuming that the optical thickness of the haze layer remains constant, *i.e.* the scattering ratio was changed by an amount sufficient to compensate for the postulated change in absorption coefficient.

The solid bar in each of the graphs shown in Fig. 20 depicts the ground range (22 km) associated with the reference values for the individual variables. Notice for the prescribed conditions that a decrease in target distance of about 25 percent is associated with: (1) a reduction in target size by 50%; (2) a reduction in surface equivalent visibility by 35%; (3) an increase in solar zenith angle from 60 to 78 degrees; (4) a decrease in surface reflectance by 50 percent, and (5) a change in wavelength from 550 to 450 nm. The detection distance is less sensitive to changes in the absorption contribution to a fixed value of total volume extinction coefficient in the boundary layer. It should be emphasized that the results shown in Fig. 20 are specific only for the conditions assumed for the diagnostic calculations. Simultaneous changes in two or more variables could of course result in a much broader range in the variation of target detection distance.

Visual Detection Distance versus Visual Fixation Time (Fig. 21).

The variations in target detection distance that are associated with changes in stimulus duration are shown in Fig. 21. The two functional relationships for contrast threshold data used for the calculations are the same as those depicted in Fig. 16. As discussed above, the first applies to unlimited viewing time (>24 sec) and the second applies to the average fixation time (1/3 sec) for the performance of visual search by the human eye. Comparative calculations for the two viewing conditions are shown for two atmospheres. Both atmospheres and target factors are the same as reference conditions cited above except that the haze layer of depth 1.3 km is represented by the LOWTRAN (Shettle and Fenn, 1979) rural model atmosphere for relative humidity equal to 70 percent for the one case and for relative humidity equal to 99% in the other case. Notice that the relative difference in detection distance versus glimpse time for the example with high humidity and high extinction coefficient is roughly the same as that for the lower humidity and lower extinction coefficient example.

Visual Detection Distance for Overcast Sky (Fig. 22).

A cloudless atmosphere was assumed for the sensitivity analyses described above. Let us now consider

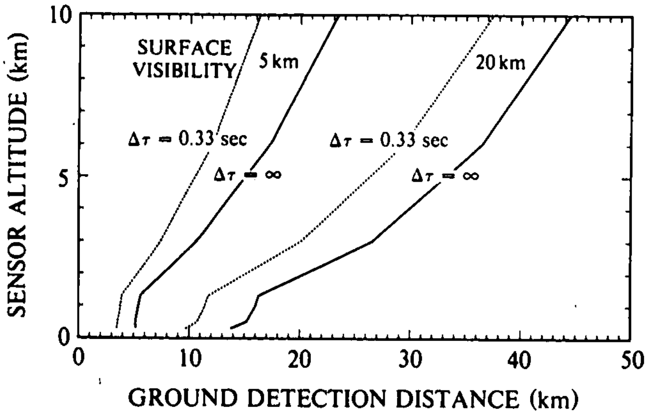

Fig. 21. Visual horizontal detection distance versus altitude for fixation times (Δt) of 0.33 sec and infinity. Calculations assume LOWTRAN rural model for boundary layer with 70 percent humidity (equivalent surface visibility of about 20 km) and with 99 percent humidity (equivalent surface visibility of about 5 km).

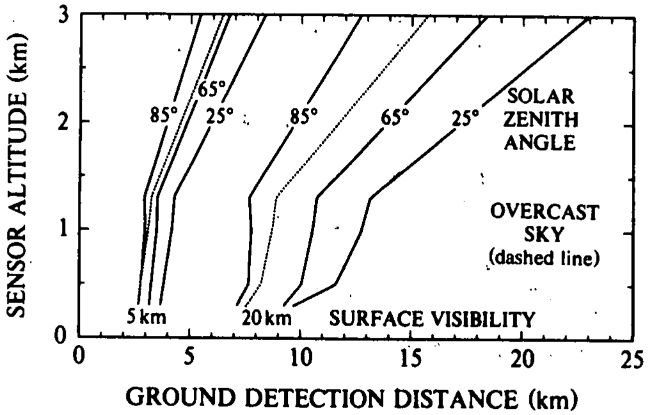

Fig. 22. Comparison of calculated target detection distance for a reference atmosphere with and without an overcast cloud layer. Calculations for clear sky case (solid lines) are shown for solar zenith angles of 25, 65, and 85 deg. Calculations for case with stratocumulus overcast (dashed line) are for solar zenith angle of 55 deg.

briefly the behavior of contrast transmittance and the variations in target detection distance that are associated with overcast sky conditions. In the region below the cloud layer in the daytime, both the inherent background radiance $_bL_o(z_t,\theta,\phi)$ and the apparent radiance $_bL_r(z,\theta,\phi)$ are essentially proportional to the downwelling radiance at the cloud base when the direct sun component of the irradiance is small in comparison with the diffuse component. Thus, except for thin clouds with significant direct sun penetration, the contrast transmittance of slant paths below the cloud deck is to a good approximation independent of the downwelling irradiance from the cloud layer (see Eq. 4). However, the path radiance and radiance transmittance (hence the contrast transmittance) are of course strongly dependent upon the optical properties along the cloud free paths of sight below the overcast.

A comparison of target detection distance as calculated with and without an overcast cloud are shown in Fig. 22. The diagnostic calculations again were made using both the 70-percent and 99-percent humidity LOWTRAN rural models for the boundary layer. For the cloud free cases, calculations are shown for solar zenith angles of 25, 65 and 85 degrees. A solar zenith angle of 55 degrees and stratocumulus overcast of average optical depth were assumed for the calculation of the cloud case. As discussed above, the slant path contrast transmittance and detection distance for the overcast condition are not sensitive to cloud optical depth (or solar zenith angle). Notice in Fig. 22 that the calculated detection distance for the cloud case corresponds to the case where the cloud is removed and the solar zenith angle is near 75 degrees. This is a typical result for conditions where a Lambertian surface reflectance is assumed and the optical properties along the viewing path are the same for both the clear and cloud examples.

7.0 SUMMARY COMMENTS

The analytic techniques that were developed as part of the experimental optical measurement and analysis program provide relatively fast and consistent estimates of the visible spectrum contrast transmittance along vertically inclined paths of sight. Essential elements of the scheme include modeling techniques suitable for field use for the determination of the apparent background sky, cloud and terrain radiance distribution as well as the radiance transmittance along the viewing path. Emphasis was placed upon the development of algorithms which are simple and easy to apply yet are adaptable so as to take advantage of all relevant observations and forecast information. The procedures developed for the calculation of clear sky radiance distribution are directly applicable to the overcast sky condition through introduction of the appropriate optical properties of the cloud layer. Comparisons of model calculations with experimental aircraft measurements of cloud radiance indicate that use of average optical depths for various cloud types as derived from the SOLMET data base yields a good first approximation to the actual overcast cloud radiance distribution.

Another recent extension to the image transmission modeling procedures is the addition of techniques to deal with the combined influences of atmospheric and target factors in order to determine target detection range for objects located at the surface and viewed from aloft. Although the results described in this report pertain to simple targets with uniform backgrounds, the diagnostic model calculations provide insight into the relative importance of the uncertainties involved in the estimates of target detection distance. Not surprisingly, the determinations are most sensitive to uncertainties in the optical depth of the atmosphere which in turn impact directly all three components of contrast transmittance, *i.e.* the inherent and apparent background radiance and the path transmittance. The sensitivity calculations also confirm the strong dependence of target detection distance on knowledge of target and background reflectivity. The model capability for joint assessment of target and environmental effects on target detection range also reveals the interactive effects of such parameters as solar zenith angle, surface reflectivity, target size, and visual fixation time for overcast and clear sky conditions.

Efforts are underway to improve the methodology for estimating image transmission characteristics by relaxation of some of the constraints which limit the applicability and accuracy of the techniques. It is important in particular, to develop techniques to exploit expanding knowledge of the directional dependence of the reflectivity of various types of ground cover. Work is also underway to incorporate analytic techniques to estimate slant-path contrast transmittance and target detection distance for inclined paths of sight in fractional cloud cover conditions.

8.0 ACKNOWLEDGEMENTS

Technique development was made possible by the extensive base of information on the behavior of atmospheric optical properties created in recent years through the program of experimental measurement and analysis carried out by the Visibility Laboratory under the direction of Mr. Richard W. Johnson. The author is grateful to Mr. Eric P. Shettle of the Air Force Geophysics Laboratory, for his valuable suggestions and guidance, especially during the early phases of the investigation. He also expresses his appreciation to Ms. Jacqueline I. Gordon and Mr. Richard W. Johnson of the Visibility Laboratory and Lt.Col. John D. Mill of the Air Force Geophysics Laboratory for their many informative discussions during the course of this work and for suggestions on improvements in the modeling procedures. He wishes to thank Mr. Nils R. Persson and Ms. Miriam K. Oleinik for their expert assistance in the computer programming phases of this study.

9.0 REFERENCES

Barteneva, O.D., (1960) "Scattering Functions of Light in the Atmospheric Boundary Layer", Bull. Acad. Sci. U.S.S.R., Geophysics Series, 1237-1244.

Blackwell, H.R., (1946) "Contrast Thresholds of the Human Eye", J. Opt. Soc. Am. **36**, 624-643.

Cox, C. and W. Munk, (1954) "Measurements of the Roughness of the Sea Surface from Photographs of the Sun's Glitter", J. Opt. Soc. Am. **44**, 838-850.

Davies, R., (1980) "Fast Azimuthally Dependent Model of the Reflection of Solar Radiation by Plane-parallel Clouds", J. Appl. Opt. **19**, 250-255.

Duntley, S.Q., (1948) "Reduction of Contrast by the Atmosphere", J. Opt. Soc. Am. **38**, 179-191.

Duntley, S.Q., A.R. Boileau, and R.W. Preisendorfer, (1957) "Image Transmission by the Troposphere I", J. Opt. Soc. Am. **47**, 499-506.

Gordon, J.I., (1969a) "Directional Radiance (Luminance) of the Sea Surface", University of California, San Diego, Scripps Institution of Oceanography, Visibility Laboratory, SIO Ref. 69-20.

Gordon, J.I., (1969b) "Model for a Clear Atmosphere", J. Opt. Soc. Am. **59**, 14-18.

Gordon, J.I., (1979) "Daytime Visibility, A Conceptual Review", University of California, San Diego, Scripps Institution of Oceanography, Visibility Laboratory, SIO Ref. 80-1, AFGL-TR-79-0257, NTIS No. ADA 085 451.

Haurwitz, B., (1948) "Insolation in Relation to Cloud Type", J. Meteor. **5**, 110-113.

Hering, W.S., (1981) "An Operational Technique for Estimating Visible Spectrum Contrast Transmittance", University of California, San Diego, Scripps Institution of Oceanography, Visibility Laboratory, SIO Ref. 82-1, AFGL-TR-81-0198, ADA 111823.

Irvine, W.M., (1968) "Multiple Scattering by Large Particles II Optically Thick Layers", Astrophys. J. **152**, 823-834.

Johnson, R.W., (1981d) "Airborne Measurements of European Sky and Terrain Radiances", University of California, San Diego, Scripps Institution of Oceanography, Visibility Laboratory, SIO Ref. 82-2, AFGL-TR-81-0275.

Joseph, J.H., W.J. Wiscombe, and J.A. Weinman, (1976) "The delta-Eddington Approximation for Radiative Flux Transfer", Atmos. Sci. **33**, 2452-2459.

Lenoble, J., (1977) "Standard Procedures to Compute Radiation Transfer in a Scattering Atmosphere", Working Group Report, Radiation Commission, International Association of Meteorology and Atmospheric Physics, 125pp..

McKellar, B.H.J., and M.A. Box, (1981) "A Scaling Group of the Radiative Transfer Equation", J. Atmos. Sci., **38**, 1063-1068.

Shapiro, R., (1982) "Solar Radiative Flux Calculations from Standard Surface Meteorological Observations", Sci. Rpt. No. 1, Systems and Applied Sciences Corporation, AFGL-TR-82-0039, 53pp., AD 118775.

Shettle, E.P., and J.A. Weinman, (1970) "The Transfer of Solar Irradiance Through Inhomogeneous Turbid Atmospheres Evaluated by Eddington's Approximation", J. Atmos. Sci. **27**, 1048-1055.

Shettle, E.P., Private Communication. See Hering (1981), Appendix A.

SOLMET (1977), "Hourly Solar Radiation-Surface Meteorological Observations Vol. 1 - Users Manual. Vol. 2 Final Report, National Climatic Center, NOAA, EDIS, TD-9724 (1979).

Taylor, J.H., (1964) "The Use of Visual Performance Data in Visibility Prediction", Appl. Opt. **3**, 562-569.

Twomey, S., (1977) "Atmospheric Aerosols", Developments in Atmospheric Science **7**, Elsevier Scientific Publishing Company, 245pp.

Welch, R.M., S.K. Cox, and W.G. Zdunkowski, (1980) "Calculations of the Variability of Ice Cloud Radiative Properties at Selected Solar Wavelengths", J. Appl. Opt., **19**, 3057-3066.

White, C.T., (1964) "Occular Behavior in Visual Search", Appl. Opt. **3**, 369-570.

SUMMARY OF INPUT DATA, COMPUTATION STEPS AND RESULTANT DATA

A.1 General Input Data

A.1.1 Number of atmospheric layers

A.1.2 Representative wavelength (μm)

A.1.3 Extraterrestrial solar (lunar) irradiance ($W/m^2\mu m$)

A.1.4 Rayleigh optical depth of top layer

A.1.5 Solar zenith angles (deg.)

A.1.6 Zenith viewing angles (deg.)

A.1.7 Average reflectance of underlying surface and reflectance of background in the vicinity of target if different than the average reflectance.

A.2 Input Data Each Layer

A.2.1 Base altitude (km)

A.2.2 Scattering mixing ratio

A.2.3 Single scattering albedo

A.2.4 Single scattering phase function (normalized to integral of one)

A.3 Computation Steps

A.3.1 Compute Rayleigh atmosphere optical thickness for each layer

A.3.2 Compute total optical thickness for each layer.

A.3.3 Compute optical depth for the base of each layer.

A.3.4 Compute single scattering phase function and asymmetry factors for each layer. (These parameters may be specified if desired in lieu of the use of model algorithms).

A.3.5 Transform optical depth, single scattering albedo, and asymmetry factor in accordance with delta-Eddington approximation.

A.3.6 Compute path function distribution for the base of each sub-layer (each layer is divided equally into 2 sub-layers).

A.3.7 Compute path radiance distribution for each sub-layer.

A.3.8 Compute path transmittance distribution for each sub-layer.

A.3.9 Compute sky/terrain radiance distribution at sub-layer boundaries.

A.3.10 Compute slant path contrast transmittance of selected paths.

A.4 Output Tables and Data

A.4.1 Path radiance, $L_r(z,\theta,\beta)$, for $0° \leqslant \theta \leqslant 85°$ (upward looking paths) for selected levels (max 5) for each θ_s (i.e. Sky Radiance) ($W/m^2\mu m\ sr$)

A.4.2 Path radiance, $L_r(z,\theta,\beta)$ for $95° \leqslant \theta \leqslant 180°$ (downward looking paths) for selected levels (max 5) for each θ_s ($W/m^2\mu m\ sr$)

A.4.3 Path plus terrain radiance $L_r(z,\theta,\beta)$ for $95° \leqslant \theta \leqslant 180°$ for selected levels (max 5) for each θ_s ($W/m^2\mu m\ sr$)

A.4.4 Contrast transmittance, $T_c(z,\theta,\beta)$ between object and sensor altitudes (max. 5 altitude intervals) for $0° \leqslant \theta \leqslant 85°$ and for each θ_s.

A.4.5 Contrast transmittance $T_c(z,\theta,\beta)$ between object and sensor altitudes (max. 5) for $95° \leqslant \theta \leqslant 180°$ and for each θ_s.

A.5 Additional Output From The Supplemental Eddington Computer Program

The standard Eddington computer program is employed as an integrated part of the model calculations of contrast transmittance. The following output from the program as modified by the delta-Eddington transformation of input parameters is available in tabular form for the base of each sub-layer and for each solar zenith angle:

- optical depths, τ and τ'
- components of Eddington diffuse radiance, $L_D(z)$ and $L_{D'}(z)$ ($W/m^2\mu m\ sr$)
- total scalar irradiance ($W/m^2\mu m$)
- downward diffuse irradiance ($W/m^2\mu m$)
- upward diffuse irradiance ($W/m^2\mu m$)
- solar irradiance ($W/m^2\mu m$)
- total downward irradiance ($W/m^2\mu m$)

SPECIFIC INPUT DATA FOR MODEL CALCULATIONS

Figure Number	8	9	10	11	12	13	14	15	Ref. A	Ref. B
Flight Number	379	466	469	469	401	422	465	435	-	-
Wavelength (nm)	475	475	475	750	550	475	550	550	550	-
Primary Haze Layer										
Upper Altitude Limit (km)	1.6	1.3	1.2	1.2	1.0	1.8	1.6	3.0	1.0	1.0
Scattering Ratio	5.1	12.0	28.0	54.0	5.3	25.0	9.0	9.3	13.0	1.3
Single Scattering Albedo	.93	.87	.87	.87	.97	.90	.90	.90	.90	.90
Upper Troposphere										
Scattering Ratio	1.16	1.16	1.16	1.5	1.2	1.2	1.16	1.2	1.2	1.2
Single Scattering Albedo	.99	.99	.99	.99	.99	.99	.99	.99	.99	.99
Cloud Layer										
Optical Depth						22.0	22.0	15.9		22.0
Base Altitude (km)						1.8	1.6	3.0		1.0
Single Scattering Albedo						1.0	1.0	1.0		1.0
Solar Zenith Angle (Deg)	36	41	44	48	72	40	51	63	60	60
Surface Reflectance	Frsnl	.06	.06	.30	.06	Frsnl	.06	.75	.08	.08

APPENDIX A

GLOSSARY AND NOTATION

The notation used in reports and journal articles produced by the Visibility Laboratory staff follows, in general, the rules set forth in pages 499 and 500, Duntley *et al.* (1957). These rules are:

- Each optical property is indicated by a basic (parent) symbol.
- A presubscript may be used with the parent symbol as an identifier, *e.g.*, b indicates background while t denotes an object, *i.e.* target.
- A postsubscript may be used to indicate the length of a path of sight, *e.g.*, r denotes an apparent property as measured at the end of a path of sight of length r, while o denotes an inherent property based on the hypothetical concept of a photometer located at zero distance from an object, *i.e.* target.
- A postsuperscript* or postsubscript$_*$, is employed as a mnemonic symbol signifying that the radiometric quantity has been generated within the path or path segment by the scattering of ambient light reaching the path from all directions and/or by emission.
- The parenthetical attachments to the parent symbol denote altitude and direction. The letter z indicates altitude in general; z_t is used to specify the altitude of a target. The direction of a path of sight is specified by the zenith angle θ and the azimuth ϕ. In the case of irradiances, the downwelling irradiance is designated by d, the upwelling by u.
- The radiometric symbols used herein now correspond to the OSA recommendations in Section 1 of Driscoll and Vaughn (1978). Prior to June 1980, the symbol used for radiance L was N, for irradiance E was H, and for attenuation length $\mathcal{L}$ was L.

Symbol	Units	Quantity
A(z)	none	Albedo at altitude z, defined $A(z) = E(z,u) \,/\, E(z,d)$.
$a(z)$	m^{-1}	Absorption coefficient.
$C(z)$	$sr^{-1}\ m^{-1}$	Diffuse component of the solar almucantar sky radiance ratio to the sun scalar irradiance and relative airmass $C(z) = \int_{4\pi} L(z,\theta',\phi')\sigma(z,\beta')d\Omega \,/\, {}_s\epsilon(z) + L_{*_a}(z) \,/\, {}_s\epsilon(z)$.
c	m/s	Speed of light $c = 2.99792458E8$.
c_1	Wm^2	First radiation constant $c_1 = 2\pi hc^2 = 3.741832E{-16}$.
c_2	mK	Second radiation constant $c_2 = ch/k = 1.438786E{-2}$.
$D(z)$	none	Radiance distribution function $D(z) = \int_{4\pi} L(z,\theta',\phi') sec\theta' d\Omega \,/\, \epsilon(z)$.
$D(\lambda)$	none	Limb darkening factor relating the average sun radiance and the center sun radiance $D(\lambda) = {}_s\bar{L}_o \,/\, {}_sL_o$.
E_λ	W/m^2	Spectral irradiance (formerly symbol H) defined as $E_\lambda = \int_{2\pi} L_\lambda(z,\theta,\phi) \cos\theta \, d\Omega$.

Symbol	Units	Quantity
E	$W/m^2 \mu m$	Broad band sensor irradiance, defined as $E = \int_0^\infty E_\lambda \overline{S_\lambda T_\lambda}\, d\lambda \,/\, \delta\lambda$.
$E(z,d)$	W/m^2	Irradiance produced by downwelling flux as determined on a horizontal flat plate at altitude z [formerly $H(z,d)$]. In this report d is used in place of the minus sign in the notation $[H(z,-)]$ which appears in Duntley (1969). This property may be defined by the equation $E(z,d) = \int_{2\pi} L(z,\theta',\phi') \cos\theta'\, d\Omega'$.
$E(z,u)$	W/m^2	Irradiance produced by the upwelling flux as determined on a horizontal flat plane at altitude z [formerly $H(z,u)$]. Here u is substituted for the plus sign formerly used in the notation $[H(z,+)]$.
$H(z)$	m	Scale height at altitude z, the height of a homogeneous atmosphere having the density of the layer at altitude z.
h	J/s	Planck constant $h = 6.626176E{-}34$.
k	J/K	Boltzmann constant $k = 1.380662E{-}23$.
L_λ	$W/sr\ m^2$	Spectral radiance (former symbol N).
L	$W/sr\ m^2 \mu m$	Broad band sensor radiance is defined as $L = \int_0^\infty L_\lambda \overline{S_\lambda T_\lambda}\, d\lambda \,/\, \delta\lambda$.
$L_o(z_t,\theta,\phi)$	$W/sr\ m^2$	Inherent radiance based on the hypothetical concept of a photometer located at zero distance from an object at altitude z in the direction specified by zenith angle θ and azimuth ϕ.
$L_r(z,\theta,\phi)$	$W/sr\ m^2$	Apparent radiance as determined at altitude z, from the end of a path of sight of length r at zenith angle θ and azimuth ϕ. This property may be defined by $L_r(z,\theta,\phi) = L_o(z_t,\theta,\phi)\, T_r(z,\theta) + L_r^*(z,\theta,\phi)$.
$L(\lambda,T)$	$W/sr\ m^2$	Black body radiance at wavelength λ and temperature T.
$L_q(z,\theta,\phi)$	$W/sr\ m^2$	Equilibrium radiance at altitude z with the direction of the path of sight specified by zenith angle θ and azimuth ϕ. This property is a point function of position and direction. As discussed by Duntley *et al.* (1957), many image transmission phenomena are most clearly understood in terms of the concept of equilibrium radiance. This concept is a natural consequence of the equation of transfer which states analytically that in any path segment the difference between the output and input radiances is attributable to a gain term and a loss term, such that some unique equilibrium radiance $L_q(z,\theta,\phi)$ must exist at each point such that the loss of radiance within the path segment is exactly balanced by the gain, *i.e.*, $\Delta L(z,\theta,\phi) = 0$.

Symbol	Units	Quantity
		By virtue of this concept and the equation of transfer, one can show that each segment of every path of sight has associated with it an equilibrium radiance, and that the space rate of change in image forming radiance caused by the path segment is in such a direction as to cause the output radiance to be closer to the equilibrium radiance than is the input radiance. This segment by segment convergence of the apparent radiance of the object field to the dynamic equilibrium radiance was clearly illustrated by the data in the 1957 paper referenced above.
$L_*(z,\theta,\phi)$	$W/sr\ m^2$	Path function at altitude z with the direction of the path of sight specified by zenith angle θ and azimuth ϕ. This property is defined by the equation $L_*(z,\theta,\phi) = L_{*_s}(z,\theta,\phi) + L_{*_a}(z)$.
$L_{*_s}(z,\theta,\phi)$	$W/sr\ m^2$	Path function due to scattering, defined by $L_*(z,\theta,\phi) = \int_{4\pi} \sigma(z,\beta')L(z,\theta',\phi')d\Omega'$.
$L_{*_a}(z)$	$W/sr\ m^2$	Path function due to emittance (absorption) $L_{*_a}(z) = a(z) L(\lambda,T)$.
$L_r^*(z,\theta,\phi)$	$W/sr\ m^2$	Path radiance as determined at altitude z at the end of a path of sight of length r in the direction of zenith angle θ and azimuth ϕ.
$L_\infty^*(z,\theta,\phi)$	$W/sr\ m^2$	Sky radiance at altitude z, zenith angle θ and azimuth ϕ. Also the path radiance for the path of sight of length ∞ from out of the atmosphere to altitude z.
${}_sL_\infty(z,\theta_s,\phi)$	$W/sr\ m^2$	Apparent radiance of the center of the solar disk as determined from the end of a path of sight of length ∞ from out of the atmosphere to altitude z at the zenith angle of the sun θ_s.
$\mathscr{L}(z)$	m	Attenuation length at altitude z. The attenuation length is the distance at which the signal is attenuated to 1/e.
$M(\lambda,T)$	W/m^2	Black body exitance (emittance) $M(\lambda,T) = \pi L(\lambda,T)$.
$\boldsymbol{m}(\lambda,T)$	W/m^2	Black body scalar exitance (emittance) $\boldsymbol{m}(\lambda,T) = 4\pi L(\lambda,T)$.
$\boldsymbol{m}_*(z)$	W/m^3	Scalar exitance (emittance) per length $\boldsymbol{m}_*(z) = \int_{4\pi} L_*(z,\theta,\phi)d\Omega$.
$\boldsymbol{m}_{*_s}(z)$	W/m^3	Scalar exitance (emittance) per length due to scattering $$\boldsymbol{m}_{*_s}(z) = \int_{4\pi} L_{*_s}(z,\theta,\phi)d\Omega = \epsilon(z)s(z).$$
$\boldsymbol{m}_{*_a}(z)$	W/m^3	Scalar exitance (emittance) per length due to absorption $\boldsymbol{m}_{*_a}(z) = a(z)\boldsymbol{m}(\lambda,T)$.
$m_\infty(z,\theta)$	kg/m^2	Absolute air mass at angle θ $m_\infty(z,\theta) = \int_z^\infty \rho(z)dr$.

Symbol	Units	Quantity
$m_\infty(z,\theta)/m_\infty(z,0^\circ)$	none	Relative optical air mass.
$m(\theta_s)$	none	Relative optical airmass at zenith angle of the sun, shorthand for $m_\infty(z,\theta_s)/m_\infty(z,0^\circ)$.
$N(z)$	none	Refractive modulus $N(z) = [n(z) - 1]E6$.
$n(z)$	none	Refractive index.
$Q(z)$	none	Optical scattering mixing ratio at altitude z. This quantity is defined as the ratio of the total volume scattering coefficient at altitude z, to the molecular (or Rayleigh) volume scattering coefficient at the same altitude z. $Q(z) = s(z)/{}_R s(z)$.
$\mathcal{Q}(z,\beta)$	none	Volume scattering function ratio at altitude z. This quantity is defined as the ratio of the total volume scattering function at altitude z and scattering angle β, to the molecular (or Rayleigh) volume scattering function at the same altitude and scattering angle. $\mathcal{Q}(z,\beta) = \sigma(z,\beta) / {}_R\sigma(z,\beta)$.
r	m	Path length, for paths of sight at zenith angles 0 to 70 degrees, $r = sec\theta\ \Delta z$.
$\overline{S_\lambda T_\lambda}$	none	Standardized relative spectral response of filter/cathode combination where S_λ is spectral sensitivity of the multiplier phototube cathode and T_λ is spectral transmittance of optical filter. The relative spectral response values are normalized to the peak value.
$s(z)$	m^{-1}	Total volume scattering coefficient as determined at altitude z. This property may be defined by the equations $s(z) = \int_{4\pi} \sigma(z,\beta)\, d\Omega = {}_R s(z) + {}_M s(z).$ In the absence of atmospheric absorption, the total volume scattering coefficient is numerically equal to the attenuation coefficient.
${}_M s(z)$	m^{-1}	Volume scattering coefficient for Mie *i.e.* particulate or droplet, scattering at altitude z.
${}_R s(z)$	m^{-1}	Volume scattering coefficient for Rayleigh *i.e.* molecular, scattering at altitude z.
T	K	Absolute temperature in degrees Kelvin.
$T_r(z,\theta)$	none	Radiance transmittance as determined at altitude z for a path of sight of length r at zenith angle θ (formerly referred to as "beam" transmittance). This property is independent of azimuth in atmospheres having horizontal uniformity. It is always the same for the designated path of sight or its reciprocal.
$T_\infty(z,\theta)$	none	Radiance transmitance for the path of sight at zenith angle θ from out of the atmosphere to the altitude z.

Symbol	Units	Quantity
$t_{\Delta z}(z)$	none	Optical thickness $t_{\Delta z}(z) = \int_{z_t}^{z} \alpha(z)dz$.
${}_a t_{\Delta z}(z)$	none	Absorption optical thickness ${}_a t_{\Delta z}(z) = \int_{z_t}^{z} a(z)dz$.
${}_M t_{\Delta z}(z)$	none	Mie optical thickness ${}_M t_{\Delta z}(z) = \int_{z_t}^{z} {}_M s(z)dz$.
${}_R t_{\Delta z}(z)$	none	Rayleigh or molecular optical thickness ${}_R t_{\Delta z}(z) = \int_{z_t}^{z} {}_R s(z)dz$.
w	J/m^3	Radiant density.
W	W	Watt W = J/s.
z	m	Altitude, usually used as above ground level.
z_t	m	Altitude of any applicable object or target.
$\alpha(z)$	m^{-1}	Volume attenuation coefficient as determined at altitude z. $\alpha(z) = a(z) + s(z)$.
β	deg	Symbol for scattering angle of flux from a light source. It is equal to the angle between the line from the source to any unit scattering volume and the path of a ray scattered off this direct line. See illustration. 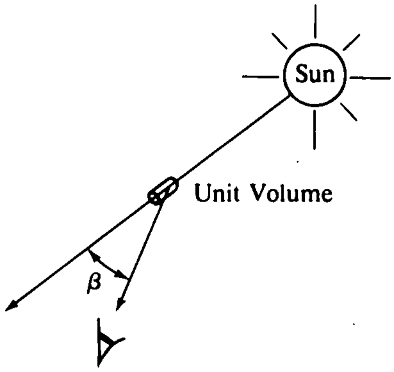
Δ	none	Symbol to indicate incremental quantity and used with r and z to indicate small, discrete increments in path length r and altitude z.
$\delta\lambda$	nm	Effective passband (formerly designated "response area") for a filtered sensor is defined as $\delta\lambda = \int_{0}^{\infty} \overline{S_\lambda T_\lambda}\, d\lambda$.

Symbol	Units	Quantity
$\epsilon(z)$	W/m^2	Scalar irradiance. This may be defined as the radiant flux arriving at a point, from all directions about that point, at altitude z (Tyler and Preisendorfer (1962)). $\epsilon(z) = \int_{4\pi} L(z,\theta',\phi')d\Omega'$.
${}_d\epsilon(z)$	W/m^2	Diffuse scalar irradiance ${}_d\epsilon(z) = \epsilon(z) - {}_s\epsilon(z)$.
${}_s\epsilon(z)$	W/m^2	Sun scalar irradiance at altitude z ${}_s\epsilon(z) = {}_s\epsilon(\infty)T_\infty(z,\theta_s)$.
ζ	m	Radius of the earth.
θ	deg	Symbol for zenith angle. This symbol is usually used as one of two coordinates to specify the direction of a path of sight.
θ'	deg	Symbol for zenith angle usually used as one of two coordinates to specify the direction of a discrete portion of the sky.
θ_s	deg	Zenith angle of the sun.
λ	nm	Symbol for wavelength.
$\bar{\lambda}$	nm	Mean wavelength is defined as $\bar{\lambda} = \int_0^\infty \lambda\, \overline{S_\lambda T_\lambda}\, d\lambda \,/\, \delta\lambda$.
$\mu(z,\beta)$	sr^{-1}	Ratio of solar almucantar sky radiance to scalar sun irradiance and airmass. $\mu(z,\beta) = L^*_\infty(z,\theta_s,\beta) \,/\, [{}_s\epsilon(z)m(\theta_s)]$.
$\xi(z)$	W/m^2	Net irradiance. $\xi(z) = E(z,d) - E(z,u)$.
$\rho(z)$	kg/m^3	Density at altitude z.
$\sigma(z,\beta)$	$m^{-1}sr^{-1}$	Symbol for volume scattering function. Parenthetical symbols are z to designate altitude and β to designate the scattering angle from a source.
$\sigma(z,\beta)/s(z)$	sr^{-1}	Normalized volume scattering function. This may be defined by the equation $\int_{4\pi}[\sigma(z,\beta) \,/\, s(z)]d\Omega = 1$.
$\tau_{\Delta z}(z,\beta)$	sr	Optical thickness function. $\tau_{\Delta z}(z,\beta) = \int_{z_t}^{z} \sigma(z,\beta)dz$.

Symbol	Units	Quantity
ϕ	deg	Symbol for azimuth. The azimuth is the angle in the horizontal plane of the observer between a fixed point and the path of sight. The fixed point may be for example, true North, the bearing of the sun, or the bearing of the moon. This symbol is usually used as one of two coordinates to specify the direction of a path of sight.
ϕ'	deg	This symbol for azimuth is usually used as one of two coordinates to specify the direction of a discrete portion of the sky.
ψ	deg	Angular solar radius at true earth-to-sun distance.
$\bar{\psi}$	deg	Angular solar radius at mean solar distance.
Ω	*sr*	Symbol for solid angle. For a hemisphere, $\Omega = 2\pi$ steradians. For a sphere, $\Omega = 4\pi$ steradians.
$\omega(z)$	none	Single scattering albedo $\omega(z) = s(z) / \alpha(z)$.

Table C.1. Notational equivalencies.

Chandrasekhar (1960)		Visibility Laboratory	
Symbol	Definition	Symbol	Definition
E	Radiant energy	E	Irradiance
πF	Net flux	ξ	Net irradiance
I	Specific intensity	$L(z,\theta,\phi)$	Radiance
J	Average intensity	$\epsilon/4\pi$	Average radiance
j	Mass emission coefficient	$\frac{L_*(z,\theta,\phi)}{\rho(z)}$	Path function/density
$j\rho$	Mass emission coefficient × density	$L_*(z,\theta,\phi)$	Path function
$j^{(s)}$	Mass emission coefficient due to scattering	$\frac{L_{*s}(z,\theta,\phi)}{\rho(z)}$	Path function due to scattering divided by the density
k	Mass absorption coefficient	α/ρ	Attenuation coefficient divided by the density
$k\rho$	Mass absorption coefficient × density	$\alpha(z)$	Attenuation coefficient
$p(\cos\Theta)$	Phase function	$4\pi\sigma(\beta)/\alpha$	Four π times volume scattering function/attenuation coefficient
s	Thickness	r	Path length
$\mathfrak{J}$	Source function	L_q	Equilibrium radiance
u	Integrated energy density	w	Radiant density
ω_0	Single scattering albedo	$\omega(z)$	Single scattering albedo
Θ	Scattering angle	β	Scattering angle
ϑ	Polar angle	θ	Zenith angle
μ	cosine of polar angle	$\cos\theta$	cosine of zenith angle
ν	Frequency	$1/\lambda$	Inverse wavelength
ρ	Density	ρ	Density
τ	Normal optical thickness	$t_{\Delta z}$	Optical thickness
φ	Azimuth	ϕ	Azimuth
ω	Solid angle	Ω	Solid angle

APPENDIX B

FASCAT PROGRAM

STRUCTURE CHART

SUBROUTINE SUMMARY

INPUT/OUTPUT FILES

USER NOTES

FLOW DIAGRAM

```
C************************* TITLE *****************************
C      FASCAT......(FORTRAN PROGRAM)
C
C      A FAST ATMOSPHERIC SCATTERING MODEL FOR CALCULATING
C      APPARENT BACKGROUND AND TARGET RADIANCE FIELDS.
C       RESEARCH BY WAYNE S. HERING
C      VISIBILITY LABORATORY
C      SCRIPPS INSTITUTION OF OCEANOGRAPHY
C      UNIVERSITY OF CALIFORNIA AT SAN DIEGO
C      LA JOLLA, CALIFORNIA 92093
C
C************************ METHOD ******************************
C      THE FASCAT COMPUTER CODE CALCULATES THE SPECTRAL RADIANCE
C      OF DISTANT OBJECTS AND BACKGROUNDS FOR  DESIGNATED SLANT
C      PATH IN THE ATMOSPHERE.THE APPARENT RADIANCE IS THE SUM
C      OF RESIDUAL BACKGROUND OR TARGET RADIANCE PLUS THE PATH
C      RADIANCE GENERATED BY  SCATTERING OF LIGHT REACHING THE
C      PATH FROM THE SUN AND THE SURROUNDING SKY AND TERRAIN.
C      SEVERAL INPUT OPTIONS ARE AVAILABLE FOR THE SPECIFICATION
C      OF THE VERTICAL PROFILES OF AEROSOL PROPERTIES.  CLOUD
C      INFORMATION IS ENTERED BY SPECIFICATION OF THE CLOUD TYPE
C      AMOUNT,ALTITUDE OF BASE AND TOP AND THE RELATIVE OPTICAL
C      THICKNESS (AVERAGE,THIN OR THICK).  FOR DESIGNATED SENSOR
C      AND TARGET ALTITUDES,THE APPARENT CONTRAST IS CALCULATED
C      FOR CLOUD FREE SLANT PATHS,WHICH MAY OR MAY NOT TRANS-
C      VERSE A FRACTIONAL CLOUD LAYER.  OBJECTS IN SUNLIGHT OR
C      SHADOW MAY BE VIEWED AGAINST SKY, CLOUD OR TERRAIN BACK-
C      GROUNDS.
```

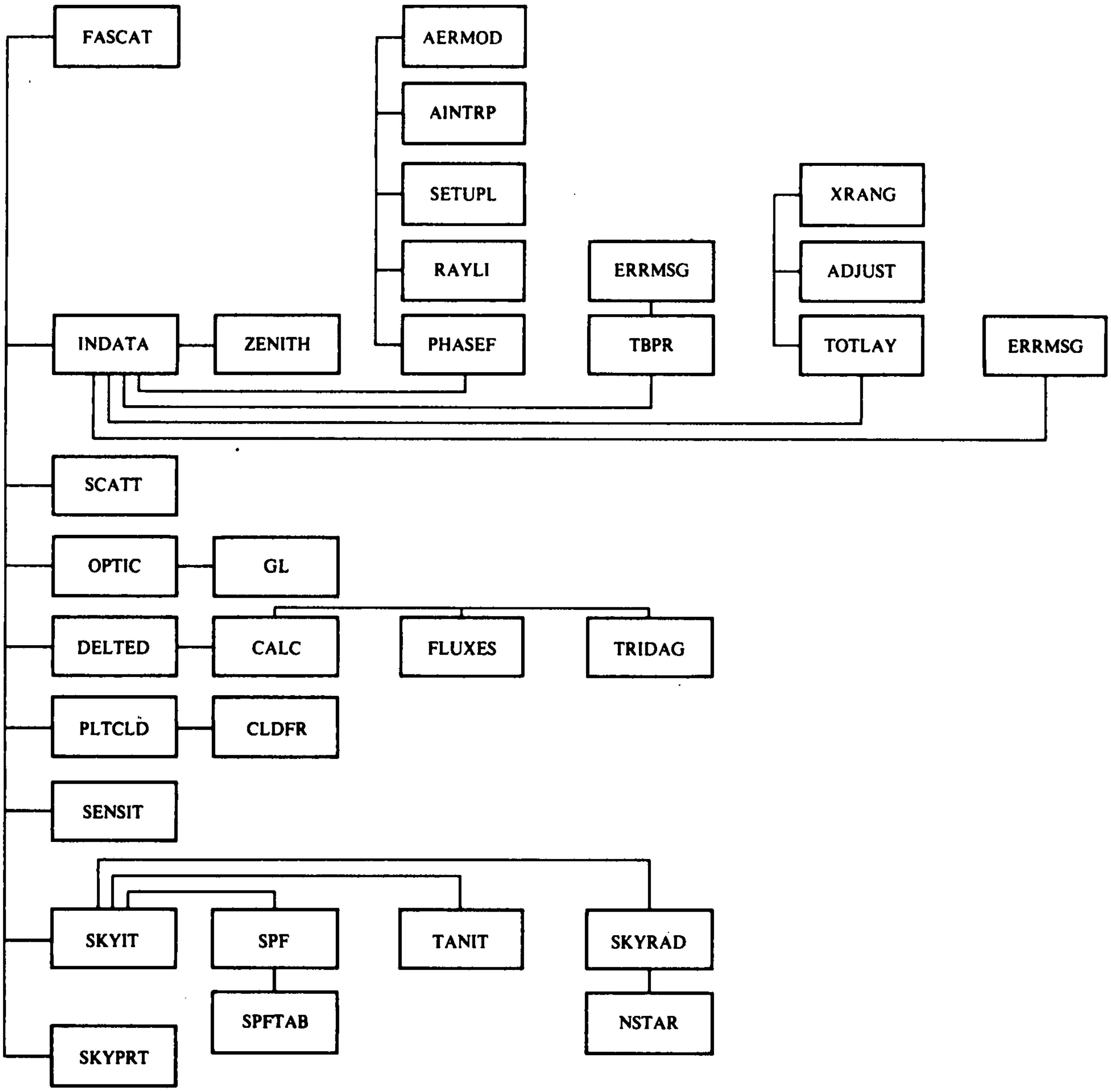
FASCAT
AERMOD
AINTRP
SETUPL
XRANG
RAYLI
ERRMSG
ADJUST
INDATA
ZENITH
PHASEF
TBPR
TOTLAY
ERRMSG
SCATT
OPTIC
GL
DELTED
CALC
FLUXES
TRIDAG
PLTCLD
CLDFR
SENSIT
SKYIT
SPF
TANIT
SKYRAD
SPFTAB
NSTAR
SKYPRT

```
C********************* PARAMETERS *****************************
C
C          SUBROUTINE ADJUST (IOPT,INDEXA,INDEXB)
C            ASSIGN ARRAYS OF ATMOSPHERIC LAYERS
C            IOPT = ASSIGNMENT CHOICES
C            INDEXA,INDEXB = MOVE INDEXB INTO INDEXA
C
C          SUBROUTINE CALC (TAU,M,IPRINT,N,ISTORE)
C            DRIVES FLUXES SUBROUTINE
C            TAU= OPTICAL DEPTH
C            M= INDEX ON LAYER/SUBLAYER
C            IPRINT = PRINT OPTION (0=NO,1=YES)
C            N = TOTAL ATMOSPHERIC LAYERS
C            ISTORE...0=NO,1=YES
C
C          SUBROUTINE CLDFR(CLR,A,B,AB,ANS,IOPT,M)
C            COMBINE DELTA EDDINGTON VARIABLES FOR DIFFUSE
C              RADIANCE CALCULATION
C            CLR = CLEAR SKY CONTRIBUTION
C            A =  FIRST CLOUD LAYER CONTRIBUTION
C            B = SECOND CLOUD LAYER CONTRIBUTION
C            AB = ALL CLOUD CONTRIBUTIONS
C            ANS = COMBINED RADIANCE
C            IOPT...1=ABOVE TOP CLOUD, 2= BELOW TOP CLOUD
C            M = INDEX ON LAYER
C
C          SUBROUTINE DELTED(N,IPRINT,ISTORE)
C            EXPAND AND PRINT DELTA-EDDINGTON PRODUCTS
C            N = TOTAL ATMOSPHERIC LAYERS
C            IPRINT = PRINT OPTION ( 0=NO, 1=YES)
C            ISTORE = STORE OPTION ( 0=NO, 1=YES)
```

```
C
C         SUBROUTINE ERRMSG(JERR)
C           HANDLES FATAL ERROR MESSAGES
C           JERR = POINTS TO FATAL ERROR
C
C         SUBROUTINE FLUXES(N,TAU)
C           DETERMINE IRRADIANCE PROFILES FOR N LAYER ATMOSPHERE
C           N= NUMBER OF ATMOSPHERIC LAYERS
C           TAU= OPTICAL DEPTH FOR WHICH FLUXES ARE CALCULATED
C           ERIC SHETTLE AFGL/OPA HANSCOM AFB MA 01731
C
C         SUBROUTINE FUNCTION GL(Q)
C           GL = ASYMMETRY FACTOR FOR COMBINED RAYLEIGH AND
C                AEROSOL SCATTERING
C           WHERE Q IS THE SCATTERING RATIO
C           (RATIO OF TOTAL & RAYLEIGH SCATTERING COEFFICIENTS)
C
C         SUBROUTINE INDATA(ISEA,LAMDA,IPRINT,N,ISTORE,BRO)
C           SUBROUTINE TO INPUT USER DATA
C           ISEA = REFLECTANCE OPTION (0=NO,1=YES)
C           LAMDA = WAVELENGTH
C           IPRINT = PRINT OPTION (0=NO, 1=YES)
C           N = TOTAL ATMOSPHERIC LAYERS
C           ISTORE = STORE OPTION (0=NO, 1=YES)
C           BRO=SURFACE RALEIGH SCATTERING COEFF  (550nm)
C         SUBROUTINE NSTAR(ITIN,IBALT,IUD,ANS,T,IT,TT,IPHI)
C           COMPUTES RADIANCE GENERATED OVER PATH FROM T & N OF
C           LAYERS
C           ITIN= TOP ALTITUDE LEVEL
```

```
C          IBALT=BOTTOM ALTITUDE LEVEL AND LAYER
C          IUD = 1 FOR UP THETA (0-85)
C                2 FOR DOWN THETA (90-180)
C          ANS = RESULT
C          T = TRANSMITTANCE FOR RANGE
C          IT = INDEX ON THETA (VIEW ANGLE)
C          TT = DIFFUSE TRANSMITTANCE
C          IPHI = INDEX ON AZIMUTHAL ANGLE
C
C        SUBROUTINE OPTIC(LAMDA,N,BRO,KCLOUD,IPRINT,ISTORE)
C          SUBROUTINE TO COMPUTE OPTICAL THICKNESS
C          LAMDA = WAVELENGTH
C          N = TOTAL ATMOSPHERIC LAYERS
C          BRO= SURFACE RALEIGH SCATTERING COEFF (550nm)
C          KCLOUD = CLOUD LAYER INDEX
C          IPRINT = PRINT OPTION...1=YES,0=NO
C          ISTORE = STORE OPTION...1=YES,0=NO
C
C
C     SUBROUTINE PHASEF(VEXT,WAVLEN,NMODEL,RHUMID,ALT,MPHASE,
C         EXTC,SCATTC,SSALB,SRATIO,PHANGL,PHFUNC,NPHASE,
C         ASSYM,IERR)
C        SUPPLIES, VIA LOOK-UP TABLES, THE EXTINCTION AND
C        SCATTERING COEFFICIENTS, SINGLE SCATTER ALBEDO,
C        SCATTERING RATIO, SINGLE SCATTER PHASE FUNCTION
C        AND ASSYMETRY PARAMETER FOR ANY OF THE LOWTRAN 5
C        AEROSOL MODELS, FOR WAVELENGTHS BETWEEN 0.55 AND
```

```
C             1.06 MICRO-METERS.
C           INPUT (**MAY BE CHANGED BY SUBROUTINE IF OUT OF RANGE)
C                VEXT   - VISIBLE EXTINCTION COEFFICIENT IN 1/KM.
C                         TOTAL EXTINCTION, INCLUDING RAYLEIGH AND
C                         AEROSOL SCATTERING AND ABSORPTION,
C                         BUT NOT GAS ABSORPTION (SEE ABOVE).
C                         REQUIRED, NO DEFAULT, RANGE, 1E-2 TO 1E3
C                WAVLEN - WAVELENGTH IN MICRO-METERS, RANGE, 0.55
C                         TO 1.06, DEFAULTS TO CLOSEST IF OUT OF
C                         RANGE.
C                NMODEL-LOWTRAN 5 AEROSOL MODEL NUMBER,DEFAULT, 1
C                     1 - RURAL
C                     2 - MARITIME
C                     3 - URBAN
C                     4 - TROPOSPHERIC
C                   5-7 - NOT USED, DEFAULT TO 1
C                     8 - ADVECTION FOG
C                     9 - RADIATION FOG
C                RHUMID - RELATIVE HUMIDITY IN PERCENT. 0.0-99%,
C                         DEFAULT= 70% IF TOO SMALL OR 99% IF TOO
C                         LARGE.
C                         FOR FOG MODELS, RH INPUT IS IGNORED.
C                ALT     ALTITUDE IN KM (FOR RAYLEIGH CALCULATION)
C                         0 TO 10 KM, DEFAULTS TO NEAREST IF OUT
C                         OF RANGE.
C                MPHASE - DIMENSION OF ARRAYS PHANGLE AND PHFUNC,
C                         BELOW.
C           OUTPUTS
C                EXTC   - EXTINCTION COEFFICIENT IN 1/KM.
C                SCATTC - SCATTERING COEFFICIENT IN 1/KM.
```

```
C             SSALB  - SINGLE-SCATTERING ALBEDO (0-1)
C             SRATIO - RATIO OF SCATT TO RAYLEIGH SCATTERING
C                      COEFFICIENT, DIMENSIONLESS ('SCATTERING
C                      RATIO')
C             PHFUNC - ARRAY (1 TO NPHASE) OF DIRECTIONAL SCAT-
C                     TERING COEFFICIENTS IN 1/(KM*STER).
C                     (SEE IERR)
C             PHANGL - ANGLES ASSOCIATED WITH PHFUNC IN DEGREES
C                      SAME FOR ALL MODELS
C             NPHASE - NUMBER OF ELEMENTS IN PHANGL AND PHFUNC
C                      =MIN(MPHASE,NZANG)(SEE AERMOD SUBROUTINE
C             ASSYM  - PHASE FUNCTION ASSYMMETRY PARAMETER(0-1)
C             IERR   - ERROR FLAG
C                 -2 - FATAL, MPHASE IS .LE. 0
C                 -1 - FATAL,VISIBLE EXTINCTION NOT SUPPLIED OR
C                      OUT OF RANGE.
C                  0 - NORMAL EXECUTION
C                  1 - WARNING, DEFAULTS USED FOR ONE OR MORE
C                        INPUTS.
C                  2 - WARNING,FULL PHASE FUNCTION NOT RETURNED
C                      (MPHASE TOO SMALL)
C                  3 - BOTH ONE AND TWO.
C                  4 - EXTINCTION.LT.RAYLEIGH, RESET TO RAYLEIGH
                 5-7 - COMBINATIONS OF 1, 2, 4
C         LTC JOHN D. MILL, AFGL/OPA, HANSCOM AFB, MA 01731
C
C         SUBROUTINE PLTCLD(N)
C           DETERMINE MULTIPLE SCATTERED RADIANCE COMPONENT FOR
C            PARTLY CLOUDY SKIES
C           N = TOTAL ATMOSPHERIC LAYERS
```

```
C
C         SUBROUTINE SCATT(SVAR1,SVAR2,BRO,I)
C           DETERMINE SCATTERING RATIO OF OVERCAST CLOUD LAYER
C           SVAR1 = SCATTERING VARIANCE
C           SVAR2 = SCATTERING VARIANCE
C           BRO = RAYLEIGH SCATTERING COEFFICIENT
C           I = INDEX ON CLOUD LAYER
C
C         SUBROUTINE SENSIT(JUD,N,JRT,JTOT)
C           FINDS SENSOR MATCH WITH BASE ALTITUDE
C           JUD ... 1= DOWN PATH, 2=UP PATH
C           N = TOTAL ATMOSPHERIC LAYERS
C           JRT ... 1=RADIANCE, 2=TARGET CONTRAST
C           JTOT = TOTAL SETS
C
C         SUBROUTINE SKYIT(N,ISEA,JUD,JTOT,JRT)
C           SUBROUTINE FOR AZIMUTHAL ANGLE INDEXING AND FOR
C           CALCULATION OF TRANSMITTANCE AND SEA SURFACE
C           REFLECTANCE
C           N = TOTAL ATMOSPHERIC LAYERS
C           ISEA = REFLECTANCE OPTION (0=NO, 1=YES)
C           JUD...  1=DOWN PATH, 2 = UP PATH
C           JTOT... TOTAL SETS OF COMPUTATIONS
C           JRT... 1 = RADIANCE, 2 = TARGET CONTRAST
C
C         SUBROUTINE SKYPRT(ISTORE,JUD,JTOT,JRT,ISEA)
C           PRINTS  TABLES FOR  RADIANCE
C           AND APPARENT TARET CONTRAST
C           ISTORE, 0=NO, 1=YES
C           JUD... 1= DOWN PATH, 2=UP PATH
```

```
C           JTOT... TOTAL SETS
C           JRT... 1= RADIANCE, 2= TARGET CONTRAST
C           ISEA...1=SEA REFLECTANCE.0=NO SEA REFLECTANCE
C
C         SUBROUTINE SKYRAD(N,ALB,ALBP,ISEA,JUD,JTOT,JRT)
C            CALCULATES APPARENT BACKGROUND AND TARGET RADIANCE
C           FIELDS AND APPARENT TARGET CONTRAST
C           N=TOTAL NUMBER OF ATMOSPHERIC LAYERS
C           ALB = AVERAGE SURFACE REFLECTANCE
C           ALBP=LOCAL OBJECT/BACKGROUND REFLECTANCE
C                 (IF NOT ALB)
C           ISEA = REFLECTANCE OPTION (0=NO,1=YES)/
C           JUD...  1=DOWN PATH  2=UP PATH
c           JTOT... TOTAL SETS
C           JRT... 1 = RADIANCE, 2 = TARGET CONTRAST
C
C         SUBROUTINE SPF(BETA,Q,P,IOP,G1,G2,C)
C           CALCULATES SINGLE SCATTERING PHASE FUNCTION
C           BETA = SCATTERING ANGLES
C           Q = SCATTERING RATIO
C           P = PHASE FUNCTION
C           IOP
C                1 P=F(Q)
C                2 FOR FOG OR CLOUD
C                3 INPUT TABLE AND G TO BE SPECIFIED BY USER
C                4 USER SPECIFIED G1,G2,C FOR H. GREENSTEIN
C                  CALCULATION,AEROSOL SCATTERING PHASE FUNCTION
C                  G1,G2,C = USER INPUT ASYMMETRY FACTORS
C                     AND WEIGHTING FUNCTION
```

```
C
C          SUBROUTINE SPFTAB(IOP,BETA,P)
C            INTERPOLATE P FROM IOP OPTION TABLE (BETA,P)
C            IOP = INDEX ON BETA TABLE
C            BETA = SCATTERING ANGLES
C            P = INTERPOLATED PHASE FUNCTION
C
C          SUBROUTINE TANIT(T,SN,L,M,THETA,A,PHI,
C            RTS,RT,IT,ISEA,JRT)
C            CALCULATES T (TRANSMITTANCE) AND SN(PATH RADIANCE)
C            FOR EACH SUBLAYER
C            T = TRANSMITTANCE
C            SN = LAYER PATH RADIANCE
C            L = INDEX FOR LAYER
C            M = INDEX ON LAYER/SUBLAYER
C            THETA = LOOK ANGLE
C            A = SINGLE SCATTERING ALBEDO FOR LAYER
C            PHI = AZIMUTHAL ANGLE
C            RTS = SOLAR ZENITH ANGLE IN RADIANS
C            RT = VIEW ANGLE IN RADIANS
C            IT = INDEX ON VIEW ANGLES
C            ISEA, 0=NO REFLECTANCE, 1 = REFLECTANCE
C
C          SUBROUTINE TBPR(N,ISTORE)
C             READ IN TABLES TO PRINT
C             N = TOTAL ATMOSPHERIC LAYERS
C             ISTORE...STORE OPTION..0=NO, 1=YES
C
C
```

```
C             N = TOTAL ATMOSPHERIC LAYERS
C             LAMDA = WAVELENGTH
C            BRO=SURFACE RALEIGH SCATTERING COEF
C
C          SUBROUTINE TRIDAG(N,SUB,DIA,SUP,CON,V)
C             SOLVES SYSTEM OF N SIMULATNEOUS LINES
C             N = NUMBER OF ATMOSPHERIC LAYER
C             SUB,DIA,SUP,CON=SYSTEM OF EQUATIONS FROM SUB.FLUXES
C             V = OUTPUT VECTOR
C
C          SUBROUTINE XRANG(X,XMIN,XMAX)
C             DETERMINE IF X IS IN RANGE OF XMIN AND XMAX
C
C          SUBROUTINE ZENITH
C             COMPUTATION OF SOLAR ZENITH ANGLE
C
C*************************************************************
C
```

```
C**************** EXTERNAL DATA FILE******************************
C       INPUT FILE
C         INPUT DATA IS LIST DIRECTED DATA
C
C       1.  (INFO(JA),JA=1,20).......................FORMAT(20A4)
C            ALPHA TITLE
C       2.  IPRINT,ISTORE,ISEA.......................FORMAT(3I5)
C            IPRINT = PRINT OPTION (0=NO,1=YES)
C            ISTORE = STORE OPTION (0=NO, 1=YES)
C            ISEA = REFLECTANCE OPTION (0=NO, 1=YES)
C       3.  ALB,LAMDA,BAT.....................FORMAT(3F10.4)
C            ALB = AVERAGE SURFACE REFLECTANCE
C            LAMDA = REPRESENTATIVE WAVELENGTH (MICROMETERS)
C            BAT = BASE ALTITUDE OF TOP LAYER (KM MSL)
C       4.  FAC .........................FORMAT(F10.4)
C            EXTRATERRESTRIAL SOLAR IRRADIANCE (UM.CM-2.NM-1)
C       5.  IZEN................................FORMAT(I5)
C            OPTION TO INPUT SOLAR ZENITH ANGLE
C            (0=NO, 1=YES)
C       6.  THETAS,JULIAN,XLAT (IF IZEN=1),FORMAT(F10.3,I5,F10.3)
C            THETAS = SOLAR ZENITH ANGLE (DEGREES AND TENTHS)
C            JULIAN = JULIAN DATE
C            XLAT = LATITUDE  (DEGREES AND TENTHS)
C       7.  HOUR,JULIAN,XLAT(IF IZEN=0)....FORMAT(F10.3,I5,F10.3)
C            HOUR = LOCAL TIME (HOURS AND TENTHS)
C            JULIAN = JULIAN DATE
C            XLAT = LATITUDE (DEGREES AND TENTHS)
```

```
C      8.  NTHETA.................................FORMAT(I5)
C          TOTAL NUMBER OF VIEW ANGLES
C          IF NTHETA = 0, USE DEFAULT VIEW ANGLES
C     9.  (THETA(JA),JA=1,NTHETA).............FORMAT(10F10.3)
C          IF(NTHETA.GT.0)
C          INDIVIDUAL VIEW ANGLES
C     10.  NLAY..................................FORMAT(I5)
C          TOTAL NUMBER OF INITIAL LAYERS OF ATMOSPHERE
C     11.  ISPF(ILAY)............................FORMAT(I5)
C           NOTE..REPEAT INPUT RECORDS 11 & 12 NLAY TIMES
C          AEROSOL TYPE OF ATMOSPHERIC LAYER
C          1 = INPUT ZL,Q,W (CALCULATES PHASE FUNCTIONS)
C          2=INPUT ZL,Q,W(SPECIFIES CLOUD & FOG PHASE FUNCTION)
C          31,32,33 = ZL,Q,W,G (ENTER PHASE FUNCTION TABLES)
C          4 = ZL,Q,W,G1,G2,C (H.G. PHASE FUNCTION CALCULATION)
C          5 = ZL,VEXT,RHUMID,NMODEL (LOWTRAN MODELS)
C      12. RECORD 12=INPUT ACCORDING TO AEROSOL TYPE(RECORD 11)
C          TYPE 1 = ZL(ILAY),Q(ILAY),W(ILAY)....FORMAT(3F10.3)
C          TYPE 2 = ZL(ILAY),Q(ILAY),W(ILAY)....FORMAT(3F10.3)
C          TYPE 31,32,ETC...ZL(ILAY),Q(ILAY),W(ILAY),G(ILAY)
C              FORMAT(4F10.3)
C          TYPE 4 = ZL(ILAY),Q(ILAY),W(ILAY),G1(ILAY),G2(ILAY),
C
C          C(ILAY)...FORMAT(7F10.3)
C          TYPE 5=ZL(ILAY),VEXT,RHUMID,NMODEL,FORMAT(3F10.3,I5)
C          ZL = BASE ALTITUDE OF LAYER (KM MSL)
C          Q = SCATTERING RATIO
C          A = SINGLE SCATTERING ALBEDO
C          G = AEROSOL ASYMMETRY PARAMETER
C          G1 = AEROSOL ASYMMETRY FACTOR (H.G.FUNCTION)
```

```
C          G2 = AEROSOL ASYMMETRY FACTOR (H.G.FUNCTION)
C          C = PARTITIONING FACTOR (H.G. FUNCTION)
C          NMODEL = LOWTRAN AEROSIL MODEL
C            1 = RURAL
C            2 = MARITIME
C            3 = URBAN
C            4 = TROPOSPHERE
C            5 -7 = NOT USED, DEFAULT TO RURAL
C            8 = ADVICTION FOG
C            9 = RADIATION FOG
C          VEXT = VISIBILITY EXTINCTION (KM-1)
C          RHUMID = RELATIVE HUMIDITY (PERCENT)
C
C
C     13.  IENDT(IF AEROSOL TYPE 31-33 IS CHOSEN).....FORMAT(I5)
C          TOTAL BETA/P ENTRIES FOR TABLE
C          REPEAT RECORDS 13 AND 14 FOR EACH 31-33  TYPE CHOSEN
C     14.  TBETA,TP(IF AEROSOL TYPE 31-33 CHOSEN),FORMAT(2F10.4)
C          TBETA =BETA ANGLE
C          TP = PHASE
C         (REPEAT IENDT TIMES FOR EACH 31-33 AEROSOL TYPE )
C     15.  NCLOUD....................................FORMAT(I5)
C          TOTAL NUMBER OF CLOUD LAYERS (MAXIMUM OF 2)
C     16.  ALTOP,ALTBT,AMTFR,ICLOUD,ICLFAC (IF NCLOUD.NE.0)..
C          FORMAT(3F10.2,2I5)
C          ALTOP = TOP ALTITUDE OF CLOUD LAYER (KM MSL)
C          ALTBT = BASE ALTITUDE OF CLOUD LAYER (KM MSL)
C          AMTFR = AMOUNT FRACTION OF CLOUD LAYER
```

```
C            ICLOUD = CLOUD TYPE,
C              1 =  CIRRUS/CIRROSTRATUS
C              2 = ALTOSTRATUS/ALTOCUMULUS
C              3 = CUMULUS
C              4 = STRATUS/STRATOCUMULUS
C              5 = NIMBOSTRATUS/PRECIPITATION
C             ICLFAC....RELATIVE OPTICAL THICKNESS
C              1 = AVERAGE OPTICAL THICKNESS
C              2 = THICK
C              3 =THIN
C                (REPEAT RECORD NCLOUD TIMES)
C       17.  NDLOOK....................................FORMAT I5
C             TOTAL TABLES FOR DOWN PATH OF SIGHT
C       18. DSENS(I),DTARG(I),DTAREF(I),DZNORM(I),DANORM(I)
C            IDTRG(I),DBREF(I),DZSLOP(I),DASLOP(I),IDLUM(I)
C            FORMAT(5F10.2,I5,3F10.2,I5)
C            IF(NDLOOK.NE.0)
C            (I=1,NDLOOK)
C            DSENS=SENSOR ALTITUDE DOWNWARD PATH OF SIGHT(KM MSL)
C            DTARG=TARGET ALTITUDE DOWNWARD PATH OF SIGHT(KM MSL)
C            DTAREF = TARGET REFLECTIVITY
C            DZNORM = TARGET NORMAL ZENITH ANGLE
C            DANORM = TARGET NORMAL AZIMUTH ANGLE
C             (DEGREES DEPARTURE FROM SOLAR AZIMUTH)
C            IDTRG = TARGET ILLUMINATION,
C             1 = SUNLIGHT
C             2 = CLOUD SHADOW
C             3 = LOCAL SHADOW
C            DBREF = LOCAL BACKGROUND REFLECTIVITY
```

```
C          DZSLOP = BACKGROUND NORMAL ZENITH ANGLE (DEGREES)
C          DASLOP = BACKGROUND NORMAL AZIMUTH ANGLE
C          (DEGREES DEPARTURE FROM SOLAR AZIMUTH)
C
C          IDLUM = BACKGROUND ILLUMINATION, 1= SUNLIGHT
C                                           2= CLOUD SHADOW
C                                           3 = LOCAL SHADOW
C      19. NULOOK.................................FORMAT I5
C          TOTAL TABLES FOR UP PATH OF SIGHT
C      20. USENS(I),UTARG(I),UTAREF(I),UZNORM(I),UANORM(I),
C          IUTRG(I)
C          IF(NULOOK.NE.0)
C          FORMAT(5F10.2,2I5)
C          (I = 1, NULOOK)
C          USENS=SENSOR ALTITUDE UPWARD PATH OF SIGHT (KM MSL)
C          UTARG=TARGET ALTITUDE UPWARD PATH OF SIGHT (KM MSL)
C          UTAREF = TARGET REFLECTIVITY
C          UZNORM = TARGET NORMAL ZENITH ANGLE (DEGREES)
C          UANORM = TARGET NORMAL AZIMUTH ANGLE
C          (DEGREES DEPARTURE FROM FROM SOLAR AZIMUTH)
C          IUTRG = TARGET ILLUMINATION
C           1 = SUNLIGHT
C           2 = CLOUD SHADOW
C           3 = LOCAL SHADOW
C      21. NPHI............................FORMAT I5
C          0 = DEFAULT AZIMUTHS = 0,180,90
C          1 = USER INPUTS 3 AZIMUTH ANGLES
C           (DEGREES DEPARTURE FROM SOLAR AZIMUTH)
C      22. PHINT(3)........................FORMAT(3F10.4)
C          IF NPHI .NE.0 ENTER 3 AZIMUTH ANGLES
C
```

```
C*****************************************************************
C      NOTES ON INPUT/OUTPUT DATA FILES
C
C  ITEM
C   2     IPRINT=1   PRINTS A SERIES OF TABLES ASSOCIATED
C         WITH THE CALCULATION OF THE IRRADIANCE AND THE
C         DIRECT AND DIFFUSE RADIANCE COMPONENTS REACHING
C         EACH ATMOSPHERIC LAYER.  THE NUMBER OF TABLE SETS
C         DEPENDS ON THE NUMBER OF CLOUD LAYERS.  FOR EXAMPLE,
C         IF THE MAXIMUM OF TWO LAYERS OF FRACTIONAL OR OVER-
C         CAST CLOUD ARE PRESCRIBED, FOUR SETS OF TABLES OF
C         4 TABLES EACH ARE PRINTED.  THE FIRST SET INCLUDES
C         ONLY THE UPPER CLOUD LAYER IN THE CALCULATIONS, THE
C         SECOND SET THE LOWER CLOUD LAYER, AND THE THIRD SET
C         INCLUDES BOTH CLOUD LAYERS.  THE LAST SET, OR FOURTH
C         SET IN THIS CASE, REFERS TO THE CLOUD FREE PORTION
C         OF THE ATMOSPHERE EXCEPT FOR INSTANCES WHERE OVER-
C         CAST IS PRESCRIBED FOR A GIVEN CLOUD LAYER.
C
C         THE FIRST TABLE IN EACH SET LISTS THE RAYLEIGH AND
C         TOTAL OPTICAL THICKNESS FOR EACH SUBLAYER.  THE
C         SECOND TABLE LISTS THE VERTICAL BEAM TRANSMITTANCE,
C         THE SINGLE SCATTERING ALBEDO AND THE COMBINED
C         RAYLEIGH PLUS AEROSOL ASYMMETRY FACTOR FOR EACH
C         SUB-LAYER.  THE THIRD TABLE LISTS THE TOTAL OPTICAL
C         DEPTH PROFILE FOR THE ACTUAL AND MODIFIED
C         DELTA-EDDINGTON ATMOSPHERE.  THE FOURTH TABLE IN
C         EACH SET LISTS THE COMPONENTS OF THE IRRADIANCE
C         PROFILES AS DETERMINED BY THE DELTA-EDDINGTON
C         COMPUTER CODE.
```

```
C
C          ISTORE = 1  STORES DATA IN UNFORMATTED BINARY FORM
C           OUTPUT HANDLING IS SYSTEM DEPENDENT
C           LOGICAL UNIT NUMBER IN PROGRAM FASCAT IS 4
C
C          ISEA = 1    PRESCRIBES LOWER BOUNDARY CONDITIONS
C          WHICH CONFORM TO A WIND RUFFLED SEA SURFACE WITH
C          LIGHT TO MODERATE WIND SPEED.  SINCE FRESNEL
C          REFLECTANCE IS ASSUMED AND A MATCHING DOWNWELLING
C          RADIANCE AND THE REFLECTED SOLAR BEAM COMPONENT ARE
C          REQUIRED, THIS OPTION IS SET UP TO OPERATE ONLY IF
C          THE 0, 90, 180 DEGREE AZIMUTHAL ANGLE OPTION IS
C          USED.  (SEE ITEM 21).
C
C   3      ALB IS USED TO CALCULATE THE CONTRIBUTION OF THE
C          DIFFUSE BACKGROUND COMPONENT OF THE PATH RADIANCE,
C          I.E. RADIANCE REFLECTED FROM THE UNDERLYING SURFACE
C          AND THEN SCATTERED BY THE ATMOSPHERE IN THE DIREC-
C          TION OF THE SENSOR OR OBSERVER.  A WEIGHTED AREA
C          AVERAGE OF THE BACKGROUND REFLECTIVITY IS REQUIRED
C          GIVING THE MOST WEIGHT TO THE BACKGROUND WITHIN
C          0 TO 25 DEGREES OF THE OBSERVATION ANGLE.  ALB WILL
C          OFTEN DIFFER FROM THE LOCAL OR IMMEDIATE BACKGROUND
C          REFLECTIVITY DBREF, DESCRIBED IN ITEM 18 BELOW.
C
C          BAT SETS THE LOWER ALTITUDE LIMIT OF THE PRIMARY
C          OZONE LAYER.  BAT SHOULD CORRESPOND TO THE BASE
C          ALTITUDE OF THE UPPER LAYER AS ENTERED IN ITEM 11,
C          AND CORRESPOND IN GENERAL TO THE TROPOPAUSE HEIGHT.
C          VALID LIMITS FOR THIS ENTRY ARE 10 TO 15 KM.  THE
```

```
C         OZONE OPTICAL DEPTH IS CALCULATED AS A FUNCTION OF
C         WAVELENGTH, ASSUMING AVERAGE TOTAL OZONE AS A
C         FUNCTION OF LATITUDE AND SEASON.  OTHER CONTRIBU-
C         TIONS TO ABSORPTION IN THE TOP LAYER SHOULD BE
C         INCLUDED IN THE SPECIFIED SINGLE SCATTERING ALBEDO
C         FOR THE LAYER (ITEM 11).
C
C    4    THE EXTRATERRESTRIAL SOLAR IRRADIANCE MAY BE
C         ENTERED IN ANY DESIRED UNITS.  THE RESULTANT RADI-
C         ANCE WILL THEN BE IN THE SAME UNITS /SR.
C         A NORMAL SET OF UNITS FOR IRRADIANCE WOULD BE
C         W*10E-6/NM*CM**2.   IT SHOULD BE
C         NOTED THAT APPARENT CONTRAST AND CONTRAST TRANS-
C         MITTANCE ARE INDEPENDENT OF FAC.
C
C    6    SOLAR ZENITH ANGLE IS AUTOMATICALLY CALCULATED FROM
C         TIME,DATE AND LATITUDE DATA.
C         IF THE OPTION TO ENTER A SPECIFIC SOLAR ZENITH ANGLE IS
C         CHOSEN IN 5, IT IS ENTERED IN ITEM.
C         THE LATITUDE AND JULIAN DATE ARE ALSO REQUIRED FOR
C         DETERMINATION OF THE AVERAGE TOTAL OZONE AMOUNT
C         (SEE ITEM 3).
C
C    7    IF LOCATION IS IN SOUTHERN HEMISPHERE, KEEP THE
C         LATITUDE ENTRY POSITIVE, BUT ADD 183 TO JULIAN DATE.
C
C    8    IT SHOULD BE NOTED THAT ONLY ROUGH CORRECTIONS FOR
C         REFRACTION AND EARTH'S CURVATURE ARE MADE,SO THAT
C         RADIANCE CALCULATIONS FOR OBSERVATION ANGLES CLOSE TO
C         THE HORIZON ARE SUBJECT TO ERRORS ASSOCIATED WITH THOSE
C         UNRESOLVED EFFECTS.
```

```
C
C 10    ONE MAY INTRODUCE AS MANY LAYERS TO DEFINE THE
C       OPTICAL PROPPERTIES OF THE ATMOSPHERE AS WARRANTED
C       BY THE COMPLETENESS AND ACCURACY OF THE AVAILABLE
C       OBSERVATIONS AND FORECASTS.  THE OPTICAL PROPERTY
C       PROFILES FOR THE CLOUD FREE AREAS (ABOVE, BELOW,
C       AND BETWEEN CLOUDS) ARE SET UP IN ITEMS 10 THRU 14.
C       CLOUD LAYERS ARE SUPERIMPOSED IN ITEMS 15 AND 16
C       AND SENSOR AND TARGET LEVELS ARE SPECIFIED IN ITEMS
C       17-20.  EVEN IN THE CASE OF AN OVERCAST SKY,
C       SET-UP A CLOUD FREE ATMOSPHERE INITIALLY FOR THE
C       COMPLETE VERTICAL PROFILE.  FOR OVERCAST LAYER (NO
C       CLOUD FREE PATH) THE CLOUD INFORMATION IN ITEM 16
C       FOR THAT LAYER WILL SUPERSEDE THE CLEAR ATMOSPHERE
C       PROFILE INITIALLY POSTULATED IN ITEM 11 FOR THAT
C       ALTITUDE INTERVAL.  A CLEAR ATMOSPHERE BOUNDARY IN
C       ITEM 11 SHOULD NOT BE CHOSEN INTERIOR TO A CLOUD
C       LAYER AS SPECIFIED IN ITEM 16.
C
C       ISPF(ILAY)    PRESCRIBES THE METHOD USED TO INTRO-
C       DUCE THE OPTICAL PROPERTIES FOR EACH LAYER (BASE
C       ALTITUDE ZL) IN A PLANE PARALLEL HORIZONTALLY HOMO-
C       GENEOUS ATMOSPHERE.  FIVE METHODS (OPTIONS) ARE
C       AVAILABLE AS DESCRIBED BELOW.  OPTICAL PARAMETERS TO
C       BE SPECIFIED ARE:
C
C          A = SINGLE SCATTERING ALBEDO.
C              RATIO OF TOTAL VOLUME SCATTERING COEFFICIENT
C              (RAYLEIGH AND AEROSOL) TO TOTAL EXTINCTION
C              COEFFICIENT (RAYLEIGH AND AEROSOL SCATTERING
C              PLUS AEROSOL ABSORPTION).
```

```
C
C          Q = SCATTERING RATIO.
C              RATIO OF TOTAL VOLUME SCATTERING COEFFICIENT
C              TO RAYLEIGH SCATTERING COEFFICIENT.
C
C          P(BETA) = AEROSOL SINGLE SCATTERING PHASE FUNCTION.
C
C          G = AEROSOL PHASE FUNCTION ASYMMETRY FACTOR.
C
C
C       THE OPTIONS FOR ENTRY OF THESE VARIABLES ARE:
C
C          1)  DATA ENTRIES FOR EACH LAYER ARE Q AND W ONLY.
C              P(BETA) AND G ARE DETERMINED BY 2-TERM
C              HENYEY-GREENSTEIN FUNCTIONS WHOSE COEFFI-
C              CIENTS G1, G2 AND C ARE PRESCRIBED IN THE
C              FASCAT CODE AS A FUNCTION OF Q.
C
C          2)  DATA ENTRIES ARE Q AND W ONLY.  OPTION MAY
C              BE USED AS AN ALTERNATE GENERAL FORMAT FOR
C              FOG/CLOUDS.  P AND G FOR AVERAGE DROP SIZE
C              DISTRIBUTION ARE RETURNED FROM MEMORY.
C
C          3)  DATA ENTRIES ARE Q, W, G AND P (SEE ITEMS
C              13 AND 14).  OPERATOR INPUTS ALL VARIABLES
C              INCLUDING LOOK-UP TABLE FOR SINGLE SCATTER-
C              ING PHASE FUNCTION (SEE ITEM 13).
C
```

```
C          4)  DATA ENTRIES ARE Q, W, AND THE HENYEY-
C              GREENSTEIN PHASE FUNCTION COEFFICIENTS, G1,
C              G2, AND C.
C
C          5)  DATA ENTRIES ARE MADE FOR EACH LAYER
C              THROUGH REFERENCE TO LOWTRAN AEROSOL MODELS.
C              USING SUBROUTINES BY J. MILL/AFL. OPERATOR
C              ENTERS:  (A) EXTINCTION COEFFICIENT (550 MM)
C              (RAYLEIGH AND AEROSOL SCATTERING PLUS
C              AEROSOL ABSORPTION BUT NOT GASEUS ABSORP-
C              TION); (B) RELATIVE HUMIDITY; AND (C) LOWTRAN
C              AEROSOL MODEL (RURAL, MARITIME, URBAN,
C              TROPOSPHERE, ADVECTION FOG, OR RADIATION FOG).
C              REQUISITE OPTICAL PROPERTIES ARE RETURNED BY
C              MODEL ALGORITHMS AND TABLE INTERPOLATION.
C
C  13&14  IF ISPF(ILAY) OPTION IS 31, 32, OR 33 (OPTION 3
C         ABOVE), BETA/P TABLE ARE ENTERED HERE.
C
C  15     A MAXIMUM OF 2 CLOUD LAYERS MAY BE ENTERED.  IF MORE
C         LAYERS ARE OBSERVED OR REPORTED, APPROXIMATE THE
C         SKY CONDITION WITH A 2-LAYER REPRESENTATION OF CLOUD
C         COVER.
C
C  16     FOR EACH CLOUD LAYER, ENTER THE BASE AND TOP ALTI-
C         TUDE (KM MSL) AND THE FRACTION OF SKY COVERED BY THE
C         CLOUD LAYER IN TENTHS.  THE CLOUD TYPE (ICLOUD) IS
C         IDENTIFIED BY ONE OF THE STANDARD CLOUD FORMS
C         (CIRRUS/CIRROSTRATUS, ALTOSTRATUS/ALTOCUMULUS,
```

```
C         CUMULUS, STRATUS/STRATOCUMULUS, AND NIMBOSTRATUS/
C         PRECIPITATION.  THE RELATIVE OPTICAL THICKNESS
C         (ICLFAC) HAS 3 OPTIONS; AVERAGE, THICK, AND THIN.
C         MODEL ALGORITHMS RETURN THE APPROPRIATE OPTICAL
C         DEPTH FROM ICLOUD AND ICLFAC WITHOUT DIRECT REFER-
C         ENCE TO THE GEOMETRIC THICKNESS OF THE CLOUD.
C
C 17&18   INTRINSIC PROPERTIES OF LOCAL SLOPING BACKGROUNDS
C         AND 3-DIMENSIONAL TARGETS FOR SELECTED DOWNWARD
C         LOOKING PATHS OF SIGHT ARE ENTERED IN ITEM 18.
C         THE TOTAL NUMBER OF COMBINATIONS OF SENSOR-TARGET
C         ALTITUDES AND TARGET-BACKGROUND CONDITIONS TO BE
C         DEALT WITH ARE ENTERED IN ITEM 17.
C
C
C                  **** IMPORTANT NOTE ****
C
C         FOR EXTRATERRESTRIAL SENSOR POSITION, DESIGNATE
C         SENSOR ALTITUDE (DSENS) AS 100 KM.
C
C
C                  **** IMPORTANT NOTE ****
C
C
C         THE ZENITH ANGLE OF THE TARGET NORMAL AND THE ZENITH
C         ANGLE OF THE LOCAL BACKGROUND NORMAL ARE ENTERED
C         DIRECTLY WITHOUT REGARD TO THE SOLAR ZENITH ANGLE.
C         HOWEVER,THE AZIMUTHAL ANGLES OF THE TARGET NORMAL AND
```

```
C        THE LOCAL BACKGROUND NORMAL ARE ENTERED AS DEPARTURES
C        REPEAT DEPARTURES FROM THE SOLAR AZIMUTHAL ANGLE,
C        WITHOUT REGARD TO SIGN.
C
C
C        THE INHERENT LOCAL BACKGROUND AND TARGET RADIANCES
C        ARE DETERMINED UNDER THE ASSUMPTION OF DIFFUSE OR
C        LAMBERTIAN REFLECTANCE OF THE IRRADIANCE REACHING
C        THE OBJECT AND BACKGROUND SURFACE FROM ALL DIREC-
C        TIONS.  ILLUMINATION OF TARGET AND/OR BACKGROUND
C        CAN BE DESIGNATED AS
C
C           1)  IN DIRECT SUNLIGHT
C           2)  IN CLOUD SHADOW WHICH WILL INCLUDE DIRECT
C               SOLAR IRRADIANCE PASSING THROUGH THIN CLOUDS
C           3)  IN LOCAL SHADOW WITH NO DIRECT SUN ILLUMIN-
C               ATION.
C
C 19&20  THESE ITEMS DEAL IN A SIMILAR MANNER WITH INPUT
C        DATA FOR UPWARD LOOKING PATHS OF SIGHT.
C
C 21&22           **** IMPORTANT NOTE ****
C
C        AS OPPOSED TO ZENITH OBSERVING ANGLES, THE AZIMUTHAL
C        OBSERVING ANGLES ARE ENTERED AS DEPARTURES REPEAT
C        DEPARTURES FROM THE SOLAR AZIMUTHAL ANGLE.
C
```

```
C        OPTION 0 DEFAULTS TO AZIMUTHAL ANGLES OF 0 (UPSUN),
C        90 (CROSSSUN) AND 180 (DOWNSUN). THIS OPTION MUST BE
C        USED IF ISEA=1 (ITEM 2).
C
C        OPTION 1 PERMITS SELECTION OF ANY 3 AZIMUTHAL VIEWING
C        DIRECTIONS, ENTERED AS THE DEPARTURES FROM THE SOLAR
C        AZIMUTHAL ANGLE WITHOUT REGARD TO SIGN.
C
C
C*********************** OUTPUT DATA ************************
C      TITLE
C      AVERAGE SURFACE REFLECTANCE
C      REPRESENTATIVE WAVELENGTH
C      BASE ALTITUDE OF TOP LAYER
C      EXTRATERRESTRIAL SOLAR IRRADIANCE
C      SOLAR ZENITH ANGLE
C      JULIAN DATE (SOLAR AZIMUTH ANGLE - LOCAL TIME)
C      LATITUDE
C      TOTAL ATMOSPHERIC LAYERS
C         LAYER NUMBER
C        AEROSOL TYPE
C        ALTITUDE
C        Q,A,G,G1,G2,C,VEXT,HUMIDITY,MODEL TYPE
C          (ACCORDING TO AEROSOL TYPE)
C      TOTAL CLOUD LAYERS
C      CLOUD LAYER
C        TYPE
C        TOP ALTITUDE OF CLOUD
C        BASE ALTITUDE OF CLOUD
```

```
C          AMOUNT FRACTION
C          RELATIVE OPTICAL THICKNESS
C        DOWNWARD PATH OF SIGHT
C          SENSOR ALTITUDE
C          TARGET ALTITUDE
C            TARGET
C              REFLECTIVITY
C              NORMAL ZENITH DEGREES
C              DIRECTION AZIMUTH DEGREES
C              ILLUMINATION
C            LOCAL BACKGROUND
C              REFLECTIVITY
C              NORMAL ZENITH DEGREES
C              DIRECTION AZIMUTH DEGREES
C              ILLUMINATION
C        UPWARD PATH OF SIGHT
C          SENSOR ALTITUDE
C          TARGET ALTITUDE
C            TARGET
C              REFLECTIVITY
C              NORMAL ZENITH DEGREES
C              DIRECTION AZIMUTH DEGREES
C              ILLUMINATION
C
C        SUBLAYER
C          Z,SCALE HT,DELTATR,DELTAT)
C        MAJOR LAYER ASYMMETRY PARAMETERS
C          T,W,G,FL,FLP
C        SOLAR ZENITH ANGLE
```

```
C       L,Z.TAUSL.TAUFSL
C       DELTA EDDINGTON RESULTS
C       DOWNWARD PATH OF SIGHT
C          INHERENT BACKGROUND SURFACE RADIANCE
C          APPARENT BACKGROUND RADIANCE TABLE
C          INHERENT TARGET RADIANCE
C          APPARENT TARGET RADIANCE TABLE
C          APPARENT TARET CONTRAST TABLE
C       UPWARD PATH OF SIGHT
C          APPARENT BACKGROUND RADIANCE TABLE
C          INHERENT TARGET RADIANCE
C          APPARENT TARGET CONTRAST TABLE
C          APPARENT TARGET RADIANCE TABLE
C*****************************************************************
C           COMMON.............
C
C          /ATMOS/HS(40,5) =  SOLAR IRRADIANCE
C                 DIO(40,5) = DELTA EDDINGTON RADIANCE
C                             (AVERAGE DIFFUSE)
C                 DI1(40,5) = DELTA EDDINGTON RADIANCE
C                             (VERTICAL ASYMMETRY)
C                 HO(40) = DOWNWARD SURFACE IRRADIANCE
C                 P(15,20) = SINGLE SCATTERING PHASE FUNCTION
C                 RAD = RADIANS
C                 PI = 3.14159
C                 BETA(15) = SCATTERING ANGLES
C                 NB = TOTAL NUMBER BETAS
C                 THETA(20) = VIEW ANGLES
C                 NT = TOTAL NUMBER OF VIEW ANGLES
```

```
C              ABETA(20) = COMPUTED SCATTERING ANGLES
C              PHASE = PHASE FUNCTION
C              UHS(40)= SOLAR IRRADIANCE (BETA.LE.25)
C              IDELTA = INDEX ON CLOUD LAYER
C              NPHI = 0 DEFAULT AZIMUTH ANGLES USED
C                     1 = ENTER 3 AZIMUTH ANGLES
C              PHINT(3) = IF NPHI.NE.0  THREE AZIMUTH ANGLES
C            TPHIS = SOLAR AZIMUTHAL ANGLE
C        /CDAT/CZL(20) = LAYER BASE ALTITUDE (WITH CLOUDS)
C              CQ(20) = SCATTERING RATIO - WITH CLOUDS
C              CG(20) = ASYMMETRY PARAMETER - WITH CLOUDS
C              CA(20) = SINGLE SCATTERING ALBEDO - WITH CLOUDS
C              CG1(20) = USER INPUT ASYMMETRY FACTOR
C              CG2 (20) = USER INPUT ASYMMETRY FACTOR
C              CLC(20) = ASYMMETRY PARAMETER
C              ICSPF(20) = AEROSOL TYPE
C
C       /CLOUD/ICLOUD(10) = CLOUD TYPE
C              ALTOP(10) = TOP ALTITUDE OF CLOUD LAYER
C              ALTBT(10) = BASE ALTITUDE OF CLOUD LAYER
C              AMTFR(10) = AMOUNT FRACTION OF CLOUD LAYER
C              NCLOUD= TOTAL NUMBER OF CLOUD LAYERS
C              ITOP(10) = CLOUD TOP ALTITUDE INDEX
C              IBOT(10) = CLOUD BOTTOM ALTITUDE INDEX
C              ICLFAC(10),1=AVERAGE OPTICAL THICKNESS OF CLOUD
C                         2=THICK
C                         3=THIN
C              DTCLD(5) = CLOUD TYPE DESIGNATION
C              CLDFAC(3) = CLOUD FACTORS FOR OPTICAL THICKNESS
C              PCF(2) = PARTLY CLOUDY FRACTION
```

```
C
C      /DAT/Q(20) = SCATTERING RATIO
C            ZL(20) = LAYER BASE ALTITUDE
C            S(40) = SCALE HEIGHT
C            BRO = SURFACE RAYLEIGH SCATTERING COEFFICIENT
C            DTR(40) = RAYLEIGH OPTICAL THICKNESS
C            Z(40) = ALTITUDE
C            DT(40) = DELTA TAU
C            FL(20)=FORWARD SCATTERING FRACTION,MONO-
C            DIRECTIONAL.
C            FLB(20)=FORWARD SCATTERING FRACTION,ISOTROPIC
C            TAUSL(40) = OPTICAL DEPTH
C            TAUPSL(40) = DELTA EDDINGTON OPTICAL DEPTH
C            THETAS = SOLAR ZENITH ANGLE
C            CTHES = COSINE THETAS
C            NC = TOTAL THETAS  =1
C            FLP(20)= FRACTIONAL SCATTERING INTO FORWARD PEAK
C            FAC = EXTRATERRESTRIAL IRRADIANCE
C
C     /DATE/JULIAN = JULIAN DATE
C            XLAT = LATITUDE IN DEGREES
C            HOUR = LOCAL TIME (TENTHS OF HOURS)
C     /DDAT/ZZL(20) = ALTITUDE
C            QQ(20) = SCATTERING RATIO
C            GG(20) = ASYMMETRY PARAMETER
C            AA(20) = SINGLE SCATTERING ALBEDO
C            GG1(20) = USER INPUT H.G.ASSYMMETRY FACTOR
C            GG2(20) = USER INPUT H.G. ASSYMTRY FACTOR
C           CCC(20) = ASYMMETRY PARAMETER
C             IISPF(20) = AEROSOL TYPE
C             USED FOR ARRAY SWAP
```

```
C
C
C     /LUIO/
C            LUW = LOGICAL UNIT NUMBER FOR OUTPUT
C            LUR = LOGICAL UNIT NIMBER FOR INPUT
C            LUST = LOGICAL UNIT NUMBER FOR STORAGE OF OUTPUT
C
C      /OPTIK/
C            MSPF(20) = SPF FLAGS
C             1 = P=F(Q)
C             2 = FOG AND CLOUD
C             3 = USER INPUT OF P/B TABLE
C             4 = USER INPUT OF G1,G2,C
C            G1(20) = USER INPUT H.G. ASYMMETRY FACTOR
C            G2(20) = USER INPUT H.G. ASYMMETRY FACTOR
C            CC(20) = USER INPUT H.G. PARTITIONING FACTOR
C            T(20) = TAU
C            BAT = BASE ALTITUDE OF TOP LAYER
C
C     /OUT/TP(80,20) = TRANSMITTANCE
C            SN(3,80,20) = NSTAR...(PHI,LAYER,THETA))
C            SNINF(3,20,3) = SKY RADIANCE UP
C            NSTRAD(3,20,3) =  SKY RADIANCE DOWN
C            HERIT = INHERENT RADIANCE
C
C     /PARAM/SUB(40),DIA(40),SUP(40),CON(40),C(40),K(20),
C            P(20),ALFA(20),BETA(20),EKT(20),EKT1(20),ET(20)
C            DETERMINE FLUXES FOR N LAYER ATMOSPHERE
C            NOTE,  THIS NAMED COMMON ONLY IN SUB FLUXES
C
```

```
C       /REFLEC/
C               ISEAT(20)=INDEX, VIEW ANGLES FOR SEA REFLECTANCE
C               N7 = TOTAL SEA REFLECTANCE VIEW ANGLES CHOSEN
C
C       /SAVE/
C               GSAVE(20) = ASYMMETRY PARAMETERS
C               SREF = SEA SURFACE SOLAR REFLECTANCE
C               SHS = SOLAR IRRADIANCE AT SURFACE
C               SPHASE=PHASE FUNCTION FOR REFLECTED SOLAR ENERGY
C               SUHS = IRRADIANCE AT SURFACE (BETA.LE.25)
C
C       /SPFT/TBETA(40,10) = CONSTANTS FOR BETA TABLE
C               TTP(40,10) = TRANSMITTANCE
C               IENDT(10) = INDEX ON B,P
C               TTB(25) = ALPHA ARRAY FOR SPF TABLE TITLE
C
C       /SSALB/W(20) = SINGLE SCATTERING ALBEDO (SAVED)
C       /TABP/ITBPR=FLAGS,PRINT SELECTED TABLE DATA(SKYRAD)
C               TABALT(2) = ALTITUDES FOR EACH TABLE
C               ALBPR = OBJECT/BACKGROUND ALBEDO
C               ITFLE = BASE FILE NUMBERS
C               INFO(27) = ALPHA TITLES FOR TABLES
C               INFIN(2) = FLAG FOR INFINITY LEVEL
C               NDLOOK = TOTAL DOWN PATH
C               NULOOK = TOTAL UP PATH
C               DTARG(10) = TARGET ALT. DOWN PATH
C               DSENS(10) = SENSOR ALT. DOWN PATH
C               DTAREF(10) = TARGET REFLECTIVITY DOWN
C               DZNORM(10) = TARGET NORMAL ZENITH ANGLE DOWN
C               DANORM (10) = TARGET NORMAL AZIMUTH ANGLE DOWN
```

```
C              DBREF(10) = LOCAL BACKGROUND REFLECTIVITY DOWN
C              DZSLOP(10) = BACKGROUND NORMAL ZENITH ANGLE DOWN
C              DASLOP(10)=BACKGROUND NORMAL AZIMUTH ANGLE DOWN
C              IDLUM(10) = BACKGROUND ILLUM.,1=SUNLIGHT
C                                             2=CLOUD SHADOW
C                                             3 = LOCAL SHADOW
C              IDTRG(10)
C                        1=SUNLIGHT
C                        2=CLOUD SHADOW
C                        3=LOCAL SHADOW
C              UTARG(10) = TARGET ALT. UP PATH
C              USENS(10) = SENSOR ALT. UP PATH
C              UTAREF(10) = TARGET REFLECTIVITY
C              UZNORM(10) = TARGET NORMAL ZENITH ANGLE UP
C              UANORM(10) = TARET NORMAL AZIMUTH ANGLE UP
C              IUTRG(10)
C                        1=SUNLIGHT
C                        2=CLOUD SHADOW
C                        3=LOCAL SHADOW
C        /TDIT/TD(80,20)=DIFFUSE TRANSMITTANCE
C
C         /XRAD/TS(20) = OPTICAL DEPTH TO BOTTOM OF LAYERS
C              A(20) = SINGLE SCATTERING ALBEDO FOR LAYERS
C              G(20) = ASYMMETRY PARAMETER FOR LAYERS
C              ALB = AVERAGE SURFACE REFLECTANCE (ASSUMED)
C              UIN = COSINE OF SOLAR ZENITH ANGLE
C              F=SOLAR FLUX ON PLANE NORMAL TO  INCIDENCE
C              IO = AVERAGE DIFFUSE RADIANCE
C              I1 = VERTICAL ANOMALLY DIFFUSE RADIANCE
```

```
C                     FDD = DIFFUSE FLUX DOWN
C                     FUP = DIFFUSE FLUX UP
C                     FDTOT = TOTAL DOWNWELLING IRRADIANCE
C                     FNET = NET IRRADIANCE
C                     GRAD = IRRADIANCE GRADIENT
C                     ENERGY = SPHERICAL IRRADIANCE
C
C************************************************************
C
```

LEGEND

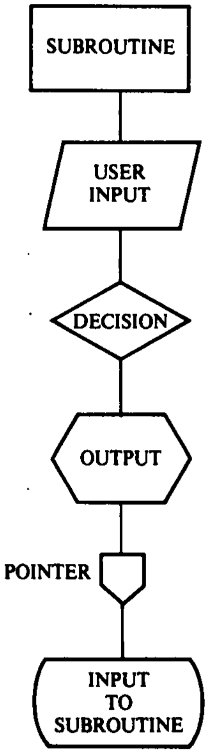
SUBROUTINE
USER INPUT
DECISION
OUTPUT
POINTER
INPUT TO SUBROUTINE

FASCAT LOGIC FLOW CHART

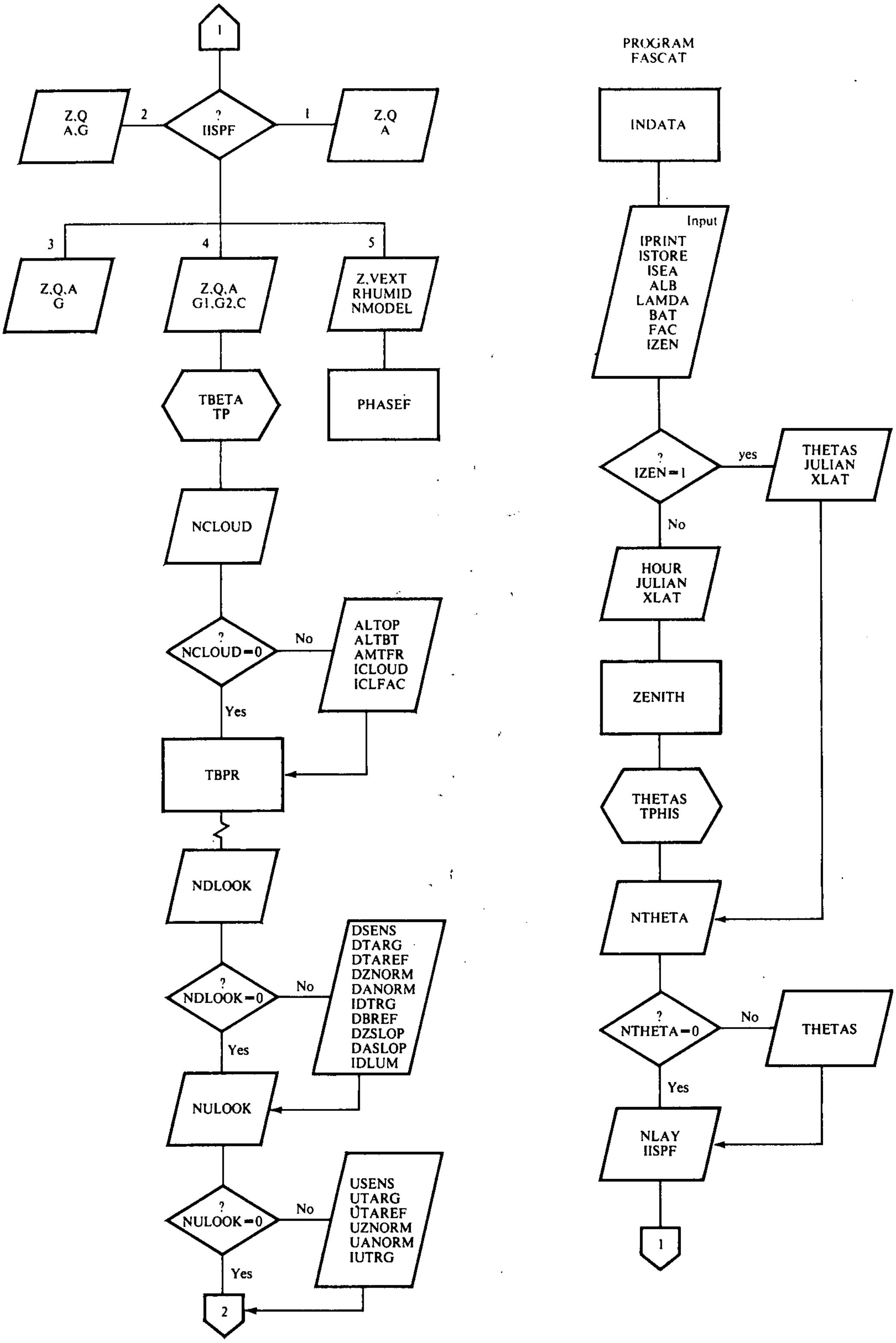

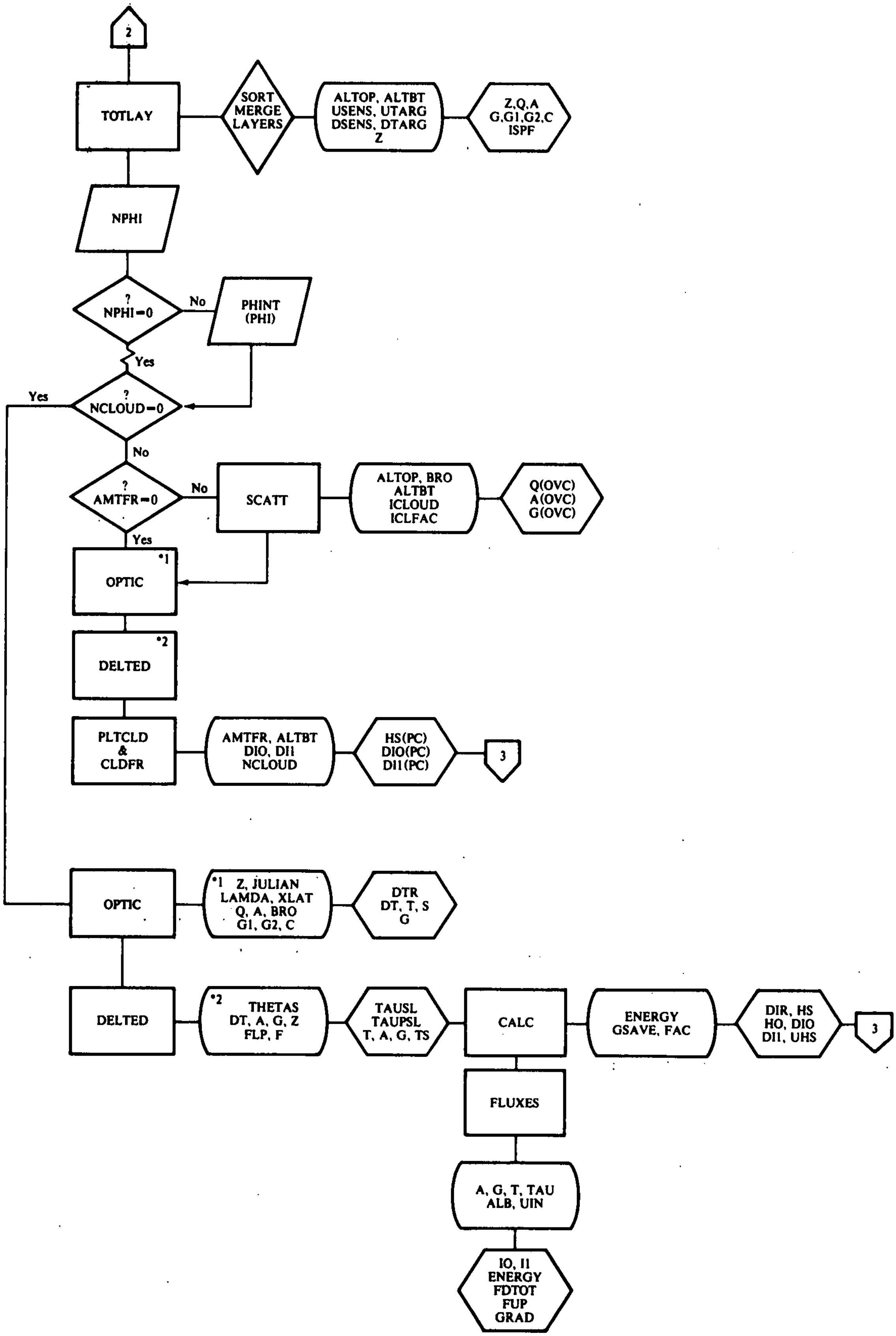
2
TOTLAY
SORT
MERGE
LAYERS
ALTOP, ALTBT
USENS, UTARG
DSENS, DTARG
Z
Z,Q,A
G,G1,G2,C
ISPF
NPHI
?
NPHI=0
No
PHINT
(PHI)
Yes
Yes
?
NCLOUD=0
No
?
AMTFR=0
No
SCATT
ALTOP, BRO
ALTBT
ICLOUD
ICLFAC
Q(OVC)
A(OVC)
G(OVC)
Yes
OPTIC
*1
DELTED
*2
PLTCLD
&
CLDFR
AMTFR, ALTBT
DIO, DI1
NCLOUD
HS(PC)
DIO(PC)
DI1(PC)
3
OPTIC
*1 Z, JULIAN
LAMDA, XLAT
Q, A, BRO
G1, G2, C
DTR
DT, T, S
G
DELTED
*2 THETAS
DT, A, G, Z
FLP, F
TAUSL
TAUPSL
T, A, G, TS
CALC
ENERGY
GSAVE, FAC
DIR, HS
HO, DIO
DI1, UHS
3
FLUXES
A, G, T, TAU
ALB, UIN
IO, I1
ENERGY
FDTOT
FUP
GRAD

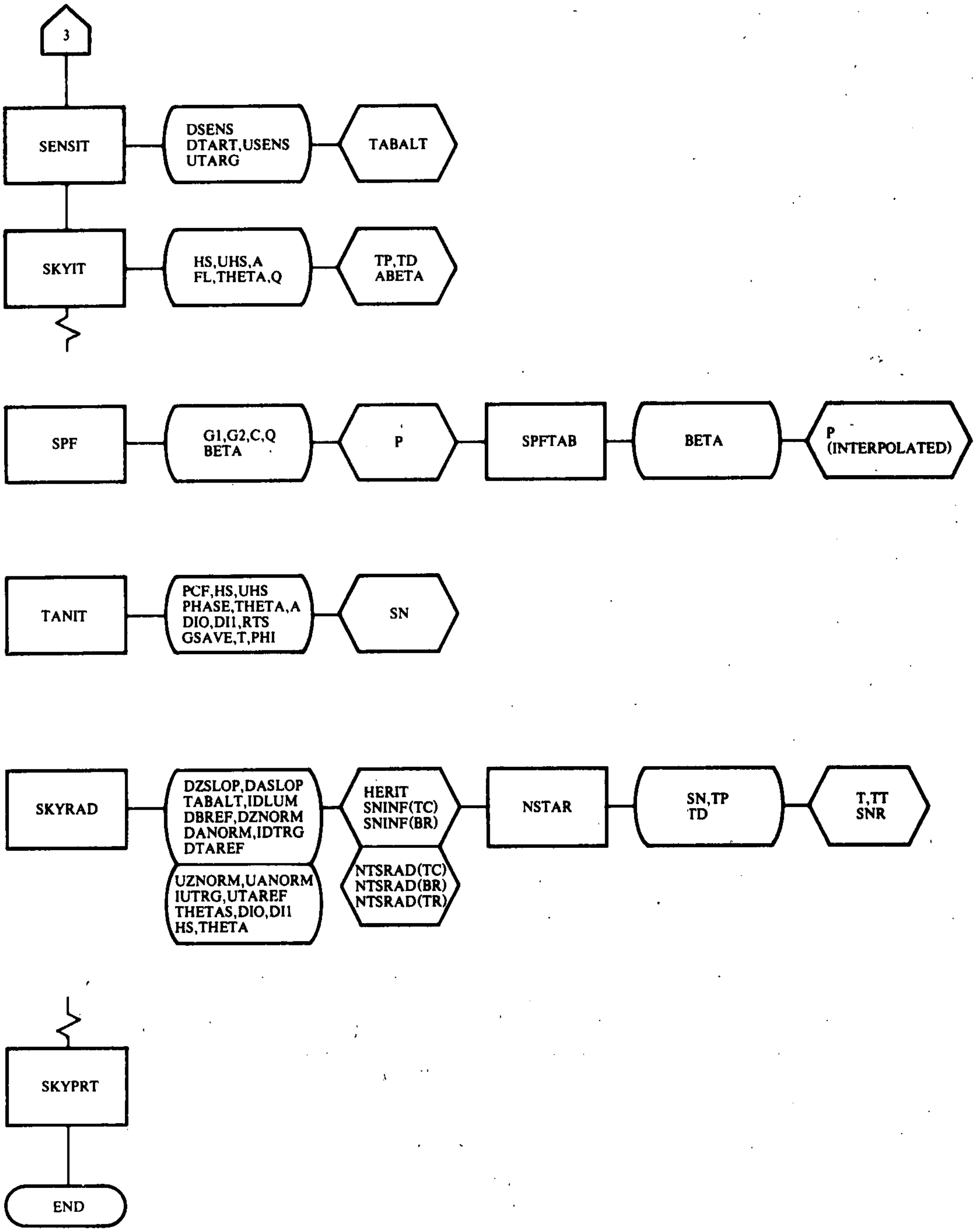
3
SENSIT
DSENS
DTART,USENS
UTARG
TABALT
SKYIT
HS,UHS,A
FL,THETA,Q
TP,TD
ABETA
SPF
G1,G2,C,Q
BETA
P
SPFTAB
BETA
P
(INTERPOLATED)
TANIT
PCF,HS,UHS
PHASE,THETA,A
DIO,DI1,RTS
GSAVE,T,PHI
SN
SKYRAD
DZSLOP,DASLOP
TABALT,IDLUM
DBREF,DZNORM
DANORM,IDTRG
DTAREF
UZNORM,UANORM
IUTRG,UTAREF
THETAS,DIO,DI1
HS,THETA
HERIT
SNINF(TC)
SNINF(BR)
NTSRAD(TC)
NTSRAD(BR)
NTSRAD(TR)
NSTAR
SN,TP
TD
T,TT
SNR
SKYPRT
END

APPENDIX C

VISIBILITY LABORATORY CONTRACTS AND RELATED PUBLICATIONS

Previous Related Contracts:
F19628-81-K-0023, F19628-78-C-0200

PUBLICATIONS:

Duntley, S.Q., R.W. Johnson, J.I. Gordon, and A. R. Boileau, (1970) "Airborne Measurements of Optical Atmospheric Properties at Night", University of California, San Diego, Scripps Institution of Oceanography, Visibility Laboratory, SIO Ref. 70-7, AFCRL-70-0137, NTIS No. AD 870 734.

Duntley, S.Q., R.W. Johnson, and J.I. Gordon, (1972a) "Airborne Measurements of Optical Atmospheric Properties in Southern Germany", University of California, San Diego, Scripps Institution of Oceanography, Visibility Laboratory, SIO Ref. 72-64, AFCRL-72-0255, NTIS No. AD 747 490.

Duntley, S.Q., R.W. Johnson, and J.I. Gordon, (1972b) "Airborne and Ground-Based Measurements of Optical Atmospheric Properties in Central New Mexico", University of California, San Diego, Scripps Institution of Oceanography, Visibility Laboratory, SIO Ref. 72-71, AFCRL-72-0461, NTIS No. AD 751 936.

Duntley, S.Q., R.W. Johnson, and J.I. Gordon, (1972c) "Airborne Measurements of Optical Atmospheric Properties, Summary and Review", University of California, San Diego, Scripps Institution of Oceanography, Visibility Laboratory, SIO Ref. 72-82, AFCRL-72-0593, NTIS No. AD 754 898 (1972c).

Duntley, S.Q., R.W. Johnson, and J.I. Gordon, (1973) "Airborne Measurements of Optical Atmospheric Properties in Southern Illinois", University of California, San Diego, Scripps Institution of Oceanography, Visibility Laboratory, SIO Ref. 73-24, AFCRL-TR-73-0422, NTIS No. AD 774 597.

Duntley, S.Q., R.W. Johnson, and J.I. Gordon, (1974) "Airborne and Ground-Based Measurements of Optical Atmospheric Properties in Southern Illinois", University of California, San Diego, Scripps Institution of Oceanography, Visibility Laboratory, SIO Ref. 74-25, AFCRL-TR-74-0298, NTIS No. ADA 013 164.

Duntley, S.Q., R.W. Johnson, and J.I. Gordon, (1975a) "Airborne Measurements of Optical Atmospheric Properties in Western Washington", University of California, San Diego, Scripps Institution of Oceanography, Visibility Laboratory, SIO Ref. 75-24, AFCRL-TR-75-0414, NTIS No. ADA 026 036.

Duntley, S.Q., R.W. Johnson, and J.I. Gordon, (1975b) "Airborne Measurements of Optical Atmospheric Properties, Summary and Review II", University of California, San Diego, Scripps Institution of Oceanography, Visibility Laboratory, SIO Ref. 75-26, AFCRL-TR-75-0457, NTIS No. ADA 022 675.

Duntley, S.Q., R.W. Johnson, and J.I. Gordon, (1976) "Airborne Measurements of Optical Atmospheric Properties in Northern Germany", University of California, San Diego, Scripps Institution of Oceanography, Visibility Laboratory, SIO Ref. 76-17, AFGL-TR-76-0188, NTIS No. ADA 035 571.

Duntley, S.Q., R.W. Johnson, and J.I. Gordon, (1977) "Airborne Measurements of Atmospheric Volume Scattering Coefficients in Northern Europe, Spring 1976", University of California, San Diego, Scripps Institution of Oceanography, Visibility Laboratory, SIO Ref. 77-8, AFGL-TR-77-0078, NTIS No. ADA 046 290.

Duntley, S.Q., R.W. Johnson, and J.I. Gordon, (1978a) "Airborne Measurements of Atmospheric Volume Scattering Coefficients in Northern Europe, Fall 1976", University of California, San Diego, Scripps Institution of Oceanography, Visibility Laboratory, SIO Ref. 78-3, AFGL-TR-77-0239, NTIS No. ADA 057 144.

Duntley, S.Q., R.W. Johnson, and J.I. Gordon, (1978b) "Airborne Measurements of Atmospheric Volume Scattering Coefficients in Northern Europe, Summer 1977", University of California, San Diego, Scripps Institution of Oceanography, Visibility Laboratory, SIO Ref. 78-28, AFGL-TR-78-0168, NTIS No. ADA 068 611.

Duntley, S.Q., R.W. Johnson, and J.I. Gordon, (1978c) "Airborne Measurements of Optical Atmospheric Properties, Summary and Review III", University of California, San Diego, Scripps Institution of Oceanography, Visibility Laboratory, SIO Ref. 79-5, AFGL-TR-78-0286, NTIS No. ADA 073 121.

Fitch, B.W. and T.S. Cress, (1981) "Measurements of Aerosol Size Distribution in the Lower Troposphere over Northern Europe", J. Appl. Met. 20, No. 10, 1119-1128, also University of California, San Diego, Scripps Institution of Oceanography, Visibility Laboratory, SIO Ref. 81-18, AFGL-TR-80-0192, NTIS No. ADA 104 272.

Fitch, B.W., (1983) "Characteristics of Aerosol Volume Distribution Measured at Meppen, W. Germany", University of California, San Diego, Scripps Institution of Oceanography, Visibility Laboratory, SIO Ref. 84-9, AFGL-TR-83-0270. **NTIS No. ADA 146 138**

Gordon, J.I., C. F. Edgerton, and S.Q. Duntley, (1975) "Signal-Light Nomogram", J. Opt. Soc. Am. **65**, 111-118.

Gordon, J.I., J. L. Harris, Sr., and S.Q. Duntley, (1973) "Measuring Earth-to-Space Contrast Transmittance from Ground Stations", Appl. Opt. **12**, 1317-1324.

Gordon, J.I., (1969) "Model for a Clear Atmosphere", J. Opt. Soc. Am. **59**, 14-18.

Gordon, J.I., (1979) "Daytime Visibility, A Conceptual Review", University of California, San Diego, Scripps Institution of Oceanography, Visibility Laboratory, SIO Ref. 80-1, AFGL-TR-79-0257, NTIS No. ADA 085 451.

Gordon, J.I., (1983) "Implications of the Equation of Transfer Within the Visible and Infrared Spectrum", University of California, San Diego, Scripps Institution of Oceanography, Visibility Laboratory, SIO Ref. 83-10, AFGL-TR-82-0223, NTIS No. ADA 133 979.

Hering, W. S., (1981a) "An Operational Technique for Estimating Visible Spectrum Contrast Transmittance", University of California, San Diego, Scripps Institution of Oceanography, Visibility Laboratory, SIO Ref. 82-1, AFGL-TR-81-0198, NTIS No. ADA 111 823.

Hering, W.S., (1981b) "Assessment of Operational Techniques for Estimating Visible Spectrum Contrast Transmittance", *SPIE Proceedings on Atmospheric Effects on System Performance,* **205**, 119-125 .

Hering, W.S., (1983), "Analytic Techniques for Estimating Visible Image Transmission Properties of the Atmosphere", University of California, San Diego, Scripps Institution of Oceanography, Visibility Laboratory, SIO Ref. 84-6, AFGL-TR-83-0236. **NTIS No. ADA 142 524**

Johnson, R.W. and B.W. Fitch, (1981) "A Review of Measured Atmospheric Optical Properties and Their Contemporary Aerosol Size Distributions", University of California, San Diego, Scripps Institution of Oceanography, Visibility Laboratory, SIO Ref. 82-22, AFGL-TR-82-0049, NTIS No. ADA 123 940.

Johnson, R.W., and J.I. Gordon, (1979) "Airborne Measurements of Atmospheric Volume Scattering Coefficients in Northern Europe, Winter 1978", University of California, San Diego, Scripps Institution of Oceanography, Visibility Laboratory, SIO Ref. 79-25, AFGL-TR-79-0159, NTIS No. ADA 082 044.

Johnson, R.W. and J.I. Gordon, (1980) "Airborne Measurements of Atmospheric Volume Scattering Coefficients in Northern Europe, Summer 1978", University of California, San Diego, Scripps Institution of Oceanography, Visibility Laboratory, SIO Ref. 80-20, AFGL-TR-80-0207, NTIS No. ADA 097 134.

Johnson, R.W. and J.I. Gordon, (1981) "A Review of Optical Data Analysis Related to the Modelling of Visible and Optical Infrared Atmospheric Properties", University of California, San Diego, Scripps Institution of Oceanography, Visibility Laboratory, SIO Ref. 83-5, AFGL-TR-82-0086, NTIS No. ADA 131 486.

Johnson, R.W. and W.S. Hering, (1981a) "Measurements of Optical Atmospheric Quantities in Europe and Their Application to Modelling Visible Spectrum Contrast Transmittance", *AGARD Proceedings on Special Topics in Optical Propagation,* AGARD-CP-300, pp. 14-1 to 14-12.

Johnson, R.W. and W. S. Hering, (1981b) "An Analysis of Natural Variations in Measured European Sky and Terrain Radiances", University of California, San Diego, Scripps Institution of Oceanography, Visibility Laboratory, SIO Ref. 82-6, AFGL-TR-81-0317, NTIS No. ADA 120 487.

Johnson, R.W. and Miriam K. Oleinik, (1984), "A Transportable, Machine Oriented Library of European Sky and Terrain Radiance Distributions with Contemporary Radiometric and Meteorological Profiles", University of California, San Diego, Scripps Institution of Oceanography, Visibility Laboratory, SIO Ref. 84-15, AFGL-TR-84-0096. **NTIS No. ADA 155 254**

Johnson, R.W., (1979) "Airborne Measurements of European Atmospheric Scattering Coefficients", *SPIE Proceedings on Atmospheric Effects on Radiative Transfer*, **195**, 31-38.

Johnson, R.W., (1981a) "Winter and Summer Measurements of European Very Low Altitude Volume Scattering Coefficients," University of California, San Diego, Scripps Institution of Oceanography, SIO Ref. 81-26, AFGL-TR-81-0154, NTIS No. ADA 106 363.

Johnson, R.W., (1981b) "Spring and Fall Measurements of European Very Low Altitude Volume Scattering Coefficients", University of California, San Diego, Scripps Institution of Oceanography, Visibility Laboratory, SIO Ref. 81-33, AFGL-TR-81-0237, NTIS No. ADA 108 879.

Johnson, R.W., (1981c) "Daytime Visibility and Nephelometer Measurements Related to its Determination", Atmospheric Environment, **15**, 10/11, 1835.

Johnson, R.W., (1981d) "Airborne Measurements of European Sky and Terrain Radiances", University of California, San Diego, Scripps Institution of Oceanography, Visibility Laboratory, SIO Ref. 82-2, AFGL-TR-81-0275, NTIS No. ADA 114 637.

Johnson, R.W., (1982) "An Experimental Device for Real Time Determination of Slant Path Atmospheric Contrast Transmittance", University of California, San Diego, Scripps Institution of Oceanography, Visibility Laboratory, SIO Ref. 82-27, AFGL-TR-82-0125. **ADA 126758**

Johnson, R.W., (1983) "An Experimental Device for Real Time Determination of Slant Path Atmospheric Contrast Transmittance (Prototype Status)", University of California, San Diego, Scripps Institution of Oceanography, Visibility Laboratory, SIO Ref. 83-14, AFGL-TR-83-0053. **NTIS No. ADA 134 000**

Shields, J.E., (1981) "An Analysis of Infrared and Visible Atmospheric Extinction Coefficient Measurements in Europe", University of California, San Diego, Scripps Institution of Oceanography, Visibility Laboratory, SIO Ref. 82-4, AFGL-TR-81-0251, NTIS No. ADA 123 999.

☆ U.S. Government Printing Office: 1986 600-000/20022